UNIVERSIDADE TECNOLÓGICA FEDERAL DO PARANÁ

MARCOS ROBERTO CIARALLO FONSECA

OPTIMIZATION OF A VEHICLE MOTOR MODEL FOR VIBRATIONAL ISOLATION VIA A PRIMAL-DUAL INTERIOR-POINT ALGORITHM

CURITIBA

2025

MARCOS ROBERTO CIARALLO FONSECA

OPTIMIZATION OF A VEHICLE MOTOR MODEL FOR VIBRATIONAL ISOLATION VIA A PRIMAL-DUAL INTERIOR-POINT ALGORITHM

Otimização de um Modelo de Motor Veicular para Isolamento Vibracional Usando um Algoritmo de Ponto Interior Primal-Dual

Dissertação apresentada ao Programa de Pós-Graduação em Engenharia Mecânica e de Materiais da Universidade Tecnológica Federal do Paraná (UTFPR) como requisito parcial para obtenção do título de Mestre em Engenharia. Área de concentração: Mecânica dos Sólidos.
Orientador: Prof. Dr. Marco Antônio Luersen.
Coorientador: Prof. Dr. Ivan Moura Belo

CURITIBA

2025

MARCOS ROBERTO CIARALLO FONSECA

OPTIMIZATION OF A VEHICLE MOTOR MODEL FOR VIBRATIONAL ISOLATION VIA A PRIMAL-DUAL INTERIOR-POINT ALGORITHM

Trabalho de pesquisa de mestrado apresentado como requisito para obtenção do título de Mestre Em Engenharia da Universidade Tecnológica Federal do Paraná (UTFPR). Área de concentração: Mecânica Dos Sólidos.

Data de aprovação: 14 de Março de 2025

Dr. Marco Antonio Luersen, Doutorado - Universidade Tecnológica Federal do Paraná

Dr. Claudio Tavares Da Silva, Doutorado - Universidade Tecnológica Federal do Paraná

Dr. Pablo Yugo Yoshiura Kubo, Doutorado - Volvo Trucks North America

Documento gerado pelo Sistema Acadêmico da UTFPR a partir dos dados da Ata de Defesa em 14/03/2025.

AGRADECIMENTOS

Primeiramente, agradeço a Deus, cuja presença iluminou meu caminho e me concedeu força e sabedoria durante toda essa jornada. Sua orientação foi fundamental em cada momento.

Dedico este trabalho com amor e gratidão aos meus pais, que já não estão mais entre nós. Seus ensinamentos e amor incondicional foram a base que me permitiu chegar até aqui. Sinto a falta deles todos os dias, mas agradeço por tudo o que me proporcionaram.

À minha esposa, Rute, meu sincero agradecimento pelo seu apoio, compreensão e amor inabalável. Sou eternamente grato por ter você ao meu lado, sempre me apoiando e me incentivando.

Agradeço também aos meus professores, Marco Antonio Luersen e Ivan Moura Belo, pelas orientações e apoio ao longo deste trabalho.

A todos que contribuíram de alguma forma para esta conquista, meu muito obrigado.

RESUMO

O projeto de coxinização é extremamente importante para garantir um bom isolamento de um equipamento que gera excitação vibratória, seja ele um motor, uma bomba hidráulica, um compressor, entre outros. Para o projeto de coxinização, o posicionamento do coxim e a sua rigidez são características importantes que influenciam no comportamento da independência das direções do movimento e também no desempenho de isolamento e devem ser adequadamente selecionados para garantir o alto desempenho de isolamento em motopropulsores. Outro fator no projeto do coxim é a "pureza modal", a qual quantifica o desacoplamento entre os graus de liberdade. Quanto maior for a pureza modal, maior será o desacoplamento de cada grau de liberdade em cada direção. Isso é importante para reduzir os efeitos vibracionais transmitidos de uma determinada força em uma determinada direção e também para o melhor controle da distribuição vibracional do sistema. Para a descrição da pureza modal, é necessário ter a informação das frequências naturais e dos modos de vibração do motopropulsor suspenso nos coxins. Já para a avaliação do desempenho de isolamento, a transmissibilidade, que é dependente da rigidez, deve ser a mais alta possível pois ela quantifica o quanto a vibração da fonte será atenuada pelo coxim. Neste trabalho, soluções analíticas são desenvolvidas levando-se em consideração os parâmetros de rigidez, amortecimento do coxim, posição das coordenadas dos coxins, ângulo dos coxins, massa e tensor de inércia. Com essas soluções analíticas torna-se possível desenvolver um processo de otimização, realizado através de um algoritmo de ponto interior primal-dual com barreira logarítmica, com o objetivo de obter um alto desempenho de isolamento vibracional e alta pureza modal. Com esse processo de otimização será possível melhorar a eficiência no desenvolvimento do projeto reduzindo a quantidade de protótipos e testes. Após a otimização foi observado, por meio dos resultados, um aumento de isolação vibracional entre 1 a 7 dBs quando comparado com a isolação antes da otimização. Em relação à pureza modal, os resultados também apresentaram melhorias significativas onde a pureza modal de cada grau de liberdade foi, no geral, superior a 85%, sendo que antes da otimização existiam purezas modais abaixo de 50%.

Palavras-chave: Coxim; Motopropulsor; Isolamento; Pureza modal; Otimização.

ABSTRACT

The mount project is extremely important to ensure good isolation of equipment that generates vibration, be it a motor, a hydraulic pump, a compressor, among others. For the mount project, the positioning of the mount and its stiffness are very important characteristics, as they influence the behavior of the independence of the movement directions and also the isolation performance. For the application of mount project in powertrains, this is not different, as the high isolation performance of the mount is extremely important to ensure the reduction of vibration transmission from the powertrain and, for this, the stiffness of the mount and its attachment point must be adequately selected. Another important factor in the mount project is the modal purity, which quantifies the decoupling between the degrees of freedom, and the greater the modal purity, the greater the decoupling of each degree of freedom in each direction. This is important to reduce the vibrational effects transmitted from a given force in a given direction and also for better control of the vibrational distribution of the system. To describe the modal purity, it is necessary to have information on the natural frequencies and vibration modes of the powertrain suspended on the mounts. To evaluate the isolation performance, the stiffness and damping of the mount must be carefully determined to ensure good isolation. Analytical solutions are developed taking into account the parameters of stiffness, mount damping, mount position, mount angle, mass and the inertia tensor. With these analytical solutions, it was possible to develop an optimization process using optimization algorithms with the objective of finding the parameters that generate high vibrational isolation performance and high modal purity. With this optimization process, it will be possible to improve efficiency in project development by reducing the number of prototypes and tests. After optimization, an increase in vibrational isolation between 1 and 7 dB was observed through the results when compared with the isolation before the optimization. Regarding the modal purity performance, the results also showed significant improvements, where the modal purity of each degree of freedom was generally higher than 85%, whereas, before optimization, there were modal purities below 50%.

Key-words: Mount; Powertrain; Isolation; Modal Purity; Optimization.

LIST OF SYMBOLS

Latin Letters

a_c	Fractional derivative order of the fractional derivative element of the second-stage isolation
a_{z1}	Fractional derivative order of the fractional derivative element of the first-stage isolation
a_{z2}	Fractional derivative order of the fractional derivative element of the first-stage isolation
b_c	Viscous force damping coefficient of the fractional derivative element of the first-stage isolation
b_{z1}	Viscous force damping coefficient of the fractional derivative element of the second-stage isolation
b_{z2}	Viscous force damping coefficient of the fractional derivative element of the second-stage isolation
$[\mathbf{B}_i]$	Position matrix of the mount on the global coordinate system
c	Damping factor
$[c_i]_L$	Damping matrix on the local coordinate system of the i-th mount
$[\mathbf{C}]$	Matrix of damping of the 6 DOF system
$\{f_{i,\theta}\}_G$	Rotational force of the i-th mount on the global coordinate system
$\{f_{i,t}\}_L$	Translational force of the i-th mount on the local coordinate system
$\{f_i\}_G$	Force of the i-th mount on the global coordinate system formed by $\{f_{i,t}\}_L$ and $\{f_{i,\theta}\}_G$
F_k	Force of the k-th DOF of the N DOF system
$\{\tilde{\mathbf{F}}\}$	Force vector generated by the motor in the complex domain
$\{\mathbf{F}\}$	Force vector generated by the motor in the real domain
$\{\mathbf{F}_c\}_G$	Total damping force of the mounts on the global coordinate system
$\{\mathbf{F}_k\}_G$	Total stiffness force of the mounts on the global coordinate system
$H(w)$	Transmissibility function
H_{12}	Cross receptance
$|H(\omega)|$	Magnitude of the transmissibility function
$[\mathbf{H}_i]$	Skew-symmetric matrix of the i-th mount

$[\mathbf{H}_k]$	Damping hysteretic matrix
i	Square root of -1
$[\mathbf{I}]$	Identity matrix
k	Spring stiffness of the Kelvin-Voigt spring-mass system
k^*	Complex stiffness
k_1	Storage modulus
k_2	Loss modulus
k_{21}	Cross dynamic stiffness
k_R	Stiffness of the elastomeric mount
k_{cc}	Stiffness of the first-stage spring of the fractional derivative model
k_{zz1}	Stiffness of the second-stage spring of the fractional derivative model
k_{zz2}	Stiffness of the second-stage spring of the fractional derivative model
$[\boldsymbol{k}_i]_L$	Stiffness matrix on the local coordinate system of the i-th mount
$[\ddots k_{r} \ddots]$	Diagonal modal stiffness matrix of the N DOF
K_1	Spring stiffness of the Kelvin-Voigt spring-mass system with second stiffness in series with the damping factor
K_2	Spring stiffness in series of the Kelvin-Voigt spring-mass system with second stiffness in series with the damping factor
$[\mathbf{K}]$	Stiffness matrix of the 6 DOF and N DOF system
$[\mathbf{K}_c]$	Stiffness matrix formed by $\mathbf{K}$ and $\mathbf{H}_k$
L	Langragian of the Motor motion
m	Mass of the Kelvin-Voigt spring-mass system
$[\ddots m_{r} \ddots]$	Diagonal modal mass matrix of the N DOF
$[\mathbf{M}]$	Mass matrix of the 6 DOF and N DOF system
q_i	Displacement of the i-generalized coordinate of the Lagrangian system
$\dot{q}_i$	Velocity of the i-generalized coordinate of the Lagrangian system
Q	Quality factor
r	Ratio of angular frequency over the natural angular frequency
$\{\boldsymbol{R}^M\}_G$	Position of the CG written from the motor side positions $\{\boldsymbol{r}_i^M\}_G$
R_R	Damping of the elastomeric mount

R_O	Resistance to the flow of the inertia track
$\{\widetilde{\mathbf{R}}\}_G$	Displacement vector of the motor at center of gravity in the complex domain
$\{\mathbf{R}\}_G$	Displacement vector of the motor at center of gravity in the real domain
$\{\boldsymbol{R_t}\}_G$	Translation displacement vector of the component of the vector $\{\mathbf{R}\}_G$
$\{\boldsymbol{R_\theta}\}_G$	Rotational displacement vector of the component of the vector $\{\mathbf{R}\}_G$
$\{\boldsymbol{R_i}\}_G$	Displacement vector of the i-th mount in the global coordinate system of the CG
$\{\ddot{\mathbf{R}}\}_G$	Acceleration vector of the motor at center of gravity in the real domain
$\{\dot{\mathbf{R}}\}_G$	Velocity vector of the motor at center of gravity in the real domain
R_j	Displacement of the j-th DOF of the N DOF system
t	Time
T^φ	Kinetic energy of the motor motion regarding the coordinate φ
T^ψ	Kinetic energy of the motor motion regarding the coordinate ψ
T_{total}	Sum of the the kinetic and potential energy of the motor motion
V^φ	Potential energy of the motor motion regarding the coordinate φ
V^ψ	Potential energy of the motor motion regarding the coordinate ψ

Greek Letters

$\alpha_{jk}(\omega)$	Element of the receptance matrix located at the j-th line and k-th column
$[\alpha(\omega)]$	Receptance matrix of the N DOF system
α	Rotation around X axis due to motor motion
Γ	Dissipative function due to the mount damping
$\delta_{i,\varphi}$	Displacement on the mount i due to the coordinate φ
$\delta_{i,\psi}$	Displacement on the mount i due to the coordinate ψ
ζ	Damping ratio
η	Loss modulus
η_r	Damping loss factor of the hysteric damping model

$[\boldsymbol{\Theta}_i]$	Matrix rotation from the local i-th mount coordinate system to the global coordinate system
$\boldsymbol{\theta}_{1i}$	Rotation angle around X from the global coordinate system to the local coordinate system of the i-th mount
$\boldsymbol{\theta}_{2i}$	Rotation angle around Y from the global coordinate system to the local coordinate system of the i-th mount
$\boldsymbol{\theta}_{3i}$	Rotation angle around Z from the global coordinate system to the local coordinate system of the i-th mount
λ	Angular frequency of the solution of the equation of the hysteretic damping model
$\left[\,\ddots\lambda_\mathrm{r}^2\ddots\,\right]$	Diagonal matrix of eigenvalues of the N DOF system of hysteretic damping model
(ϕ_{jr}) column	Element of the eigenvector matrix located at the j-th line and r-th column
φ	Rotation around Z axis due to motor motion
$[\boldsymbol{\Phi}]$	Normalized eigenvector of the N DOF system
ψ	Rotation around Y axis due to motor motion
$[\boldsymbol{\Psi}]$	Eigenvector of the N DOF system
ω	Angular frequency
$[\boldsymbol{\omega}]$ $\{\widetilde{\mathbf{R}}\}_G$	Matrix of angular frequency related to the harmonic displacement of
$\left[\,\ddots\overline{\omega}_\mathrm{r}^2\ddots\,\right]$	Diagonal matrix of eigenvalues of angular frequency of N DOF system without damping

LIST OF ABBREVIATIONS AND ACRONYMS

CG: Center of Gravity

CG: Conjugate Gradient

CNF: Constant Natural Frequency

CS: Complex Spring

DOF: Degree of Freedom

EMA: Experimental Modal Analysis

FRF: Frequency Response Function

KKT: Karush-Kuhn-Tucker

MDOF: Multiple Degrees of Freedom

PDLB: Primal-Dual Logarithmic Barrier

SDOF: Single Degree of Freedom

VCS: Vehicle Coordinate System

TRA: Torque Roll Axis

LIST OF FIGURES

LIST OF TABLES

TABLE OF CONTENTS

1 INTRODUCTION

The effect and perception of vibration have always been relevant in the operation of dynamic systems. This relevance has led to the development and application of vibration analysis to prevent unforeseen issues. For instance, vibration analysis is widely used in predictive maintenance, enabling the diagnosis of faults—especially in their early stages—thereby reducing cost impact and supporting decision-making to prevent critical issues (Chu, Nguyen, Yoo and Wang, 2024).

Another example is the application of vibration analysis in the automotive industry from a comfort perspective, where the driver's physiological responses were investigated through a whole-body vibration model. The study identified vibration-induced effects such as muscle spasms and abdominal pain (Sezgin; Arslan, 2012).

Many material studies have been conducted—and continue to be—to improve the efficiency of vibration isolation. One example is the use of metamaterials, which are meticulously designed at the micro- or nano-scale to enhance vibration isolation performance (Rifaie; Abdulhadi; Mian, 2022).

There are two types of isolation systems for mounts. The first type of isolation is passive, in which techniques using rubber elements or mechanical springs are used. Isolation is achieved by limiting the capacity of vibration transmitted from the source to the structure to be isolated. This is done through a mechanical connection that dissipates or redirects the vibration energy before it reaches the structure to be isolated. Passive methods sometimes involve electromechanical controls to adjust the system, but the isolation mechanism is passive. Passive systems are economical, and their relative simplicity makes them more reliable and safer. Elastomers used in the automotive industry to isolate powertrains are one of the most used passive isolators. Additionally, passive isolation systems also offer good performance, low cost, high reliability, and relative simplicity. The second type of isolation is active isolation, which consists of an insulating material, for example, hydraulic fluid, a vibration sensor, an electronic circuit, and an actuator. The vibration from the powertrain is read by the vibration sensor, which transmits the information to the electronic circuit, which calculates in real-time the necessary displacement compensation. This displacement compensation is transmitted to the actuator to cancel the vibrations. The performance

of active isolators is superior to that of passive actuators; however, cost and complexity issues hinder their application.

Despite these technical differences in isolation technologies, the physical parameters to obtain a high isolation performance are the same.

The isolation performance is a complex study because it varies according to the frequency and the interactions of the mount and the fixation also play a critical behavior in the isolation performance. One of the things that contribute to the performance of the mount project is the modal purity because it implies that once some direction is excited the other will not be if the modal purity is high. The Experimental Modal Analysis (EMA) is used to study many structural properties, one of them being the modal purity. The EMA technique can be applied to evaluate the rigid body modes of the powertrain, which can induce low-frequency vibration when excited by the track or from the powertrain itself if the modal purity is low.

The effectiveness of a mount project's isolation performance is not limited to modal purity. It is influenced by factors such as dynamic stiffness, local modes of the metal part of the mount, mass-spring mode of the rubber or isolator material, load variation, etc. All these parameters cause the isolation to change across different frequencies.

Therefore, it is important to have robust virtual models, effective measurement methodologies, and practical experience to properly consider the variables that influence isolation performance and determine which changes should be made to improve the mount project.

Currently, optimization tools have been used in different applications of science and are powerful in solving many complex problems with effective results concerning time and performance, so within this context, optimization tools are used in this work to explore the mount project aiming to define the variables that result in the best performance within certain restrictions that are imposed by the criterion of the mount project.

1.1 MOTIVATION AND OBJECTIVES

The isolation performance of the mount system is of paramount importance to achieve good quality perception and durability of mechanical systems. To achieve high isolation performance is very common to have only the stiffness as the variable to

define the mount project performance, in fact, the stiffness is really critical in the isolation performance, however, the mount position is also important because it influences the rigid body mode behavior. Depending on the mount position, it can have or not have coupled body modes for the same mount stiffness. Thus, the objective of this work is to expand and extend the possibility of achieving a high-isolation performance by including more variables that somehow contribute to the isolation performance as it is the case of the mount position.

With that in mind, this work focuses on obtaining the best possible combination exploring not only the stiffness but the mount position as well.

The primary goal of this work is to develop an analytical model to calculate the modal purity of the rigid body modes of a powertrain suspended on its mounts and, at the same time, to assess the transmissibility function, which quantifies numerically the isolation performance. To do this study, an optimization algorithm is used to figure out the best decoupling performance among the rigid body modes and transmissibility. The analytical model is generic in terms of number of mounts, their position, and stiffness. However, other parameters like damping and mount angle can be assessed as fixed parameters.

Since the rigid body modes are in a low-frequency region, which is only part of the isolation performance problem, an analytical model is built and integrated into the optimization process to evaluate the transmissibility performance of the mounts together with the modal purity.

The combination of evaluating the rigid body modes and the transmissibility function is an effective approach to achieving good isolation performance. However, it is important to note that the transmissibility function in this model is limited to mid-frequency evaluations. High-frequency evaluations will not be performed due to the presence of many resonances, and the linear approach of the mount transmissibility cannot be considered valid.

1.2 ORGANIZATION OF THE TEXT

This text is divided into six chapters. Chapter 1 presents the motivation and objectives of this work. Chapter 2 discusses the available literature on vibration isolation explaining at the same time the most important features and the types of mounts used in the automotive sector.

Chapter 3 presents the analytical model of a generic mount system of six DOF and the math approach to build it. On the sequence the concepts that formed the model to evaluate the performance of the transmissibility function are presented.

Chapter 4 presents the methodology used to apply the optimization process and shows the principles of the algorithm used to carry out the optimization of the developed objective function and gives more details of it.

In Chapter 5 the model of six DOF is validated using results of simulation already used on the market and in sequence the optimization results are presented.

Chapter 6 presents the conclusions and possibilities for future works are discussed.

1.3 SCOPE OF THE STUDY

Since the field of vibration studies is quite broad, it is essential to clearly define the limitations of this work.

This research focuses on the development and analysis of a vibration isolation system for engine mounts, with a particular emphasis on enhancing comfort. The study evaluates vibration isolation performance based on two key aspects: rigid body mode decoupling and transmissibility within the frequency range of 1 to 600 Hz. Accordingly, modal purity and transmissibility are used as output criteria to assess whether the predefined performance targets are met.

The primary objective is to assess the system's effectiveness in attenuating vibrations transmitted from the engine to the vehicle frame, with particular attention, though not limited, to the low-frequency range, where human sensitivity to vibration is more pronounced. This research aims to provide guidance for mount isolation system designers in selecting the appropriate parameters to ensure high levels of comfort.

The scope of the study is limited to analyses concerning stiffness, transmissibility, and mount positioning. The mount's characteristics, such as frequency-dependent performance, are modelled and simulated. However, long-term durability, material degradation, and fatigue effects are not considered. Likewise, thermal influences and manufacturing tolerances fall outside the scope of this work.

2 BIBLIOGRAPHY REVIEW

2.1 PHYSICAL PARAMETERS OF VIBRATION ISOLATORS

Vibrational isolation, as mentioned earlier, is of utmost importance to achieve greater comfort within the context of the motor mount project. Therefore, some characteristics and parameters that involve the study of this vibrational isolation phenomenon are highlighted.

Regarding the influence of transmissibility, the evaluation of behavior for a mass-spring-damper system, from which important information is derived, is based on one degree of freedom (DOF) with the excitation as shown in Figure 1.

Figure 1: Model of a single degree of freedom system being driven by the base.
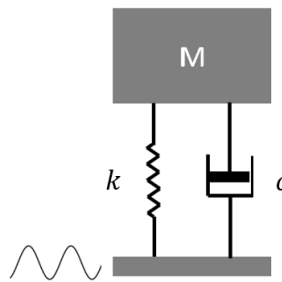
Source: adapted from Griffin (1990).

Considering the force input at the base and using the concepts of mechanical impedance, the transmissibility, as demonstrated in Griffin (1990), can be obtained as

$$H(\omega) = \frac{k + i\omega}{k + i\omega c - \omega^2 m},$$

$$\tag{1}$$

where $H(\omega)$ is the transmissibility of the system, which is dependent on the stiffness k, the angular frequency ω, the mass m and the damping constant c.

The module of transmissibility, $|H(\omega)|$, is often expressed as a function of $r = f/f_n$ and the damping ratio ζ, so $|H(\omega)|$ is expressed as $|H(r)|$

$$|H(r)| = \left[\frac{1 + (2\zeta r)^2}{(1 - r^2)^2 + (2\zeta r)^2} \right]^{\frac{1}{2}}.$$

$$\tag{2}$$

The behavior of the transmissibility while keeping r constant and varying ζ can be observed in Figure 2.

Figure 2: Effect of damping on the transmissibility of a single degree of freedom model with vibrational excitation at the base.
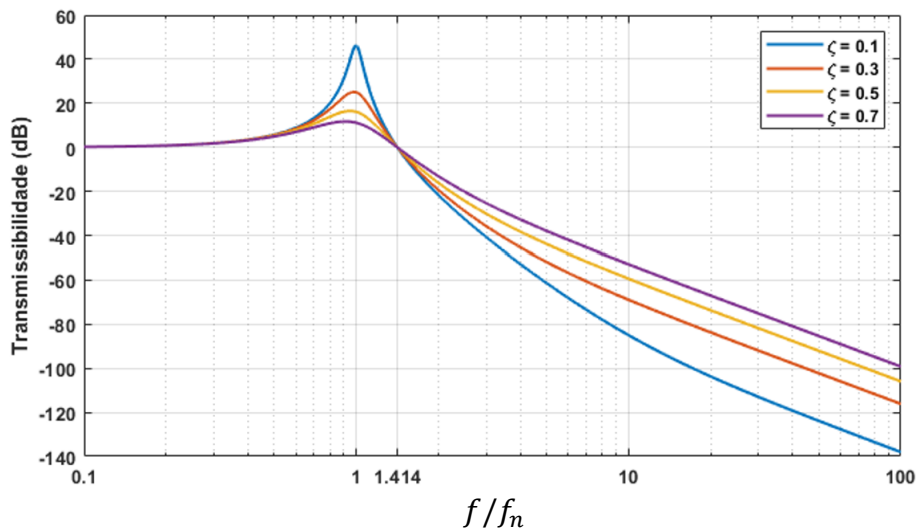
Source: adapted from Harris and Piersol (2002).

As can be observed, there is a significant influence of damping on the transmissibility response. Increased damping markedly reduces the transmissibility in the vicinity of the natural frequency, f_n. In this region, the higher the ζ the lower the transmissibility value. However, the transmissibility remains the same for different values of ζ when the ratio r is $\sqrt{2}$, and after this value, the transmissibility increases as the damping ratio increases. The ratio r is used only with the objective of showing, whatever is the natural frequency, before, at and after $\sqrt{2}$ the transmissibility function behaves with a specific trend in one degree of freedom of the mass-spring system. Thus, it becomes clear the influence of damping on the vibrational filtering effect and how it should be carefully evaluated for each type of application. As mentioned by Ewins (1984), it is worth noting that this transmissibility model was built considering a system with viscous damping. However, for multiple degrees of freedom (MDOF) systems, hysteric damping is more appropriate as it shows a dependency of damping on frequency, which does not occur in the viscous model used here. Despite this more complex behavior for real structures, the SDOF model provides clear information about the influences that damping can have on the transmissibility function. To find the damping values of the mounts, the Complex Spring (CS) model described in Graesser and Wong (1991) is used. In this model, there is the complex modulus $k^* = k_1 + ik_2$, consisting of k_1, the "storage modulus", and k_2, the "loss modulus". The absolute value of k^*, $|k^*|$, is the dynamic stiffness.

As mentioned by Ooi and Ripin (2010) the cross receptance H_{21} resulting from the cross dynamic stiffness k_{21} is expressed as

$$H_{21}(i\omega) = \frac{1}{k + ic\omega}.$$

(3)

The cross-dynamic stiffness k_{21} is the inverse of H_{21} and the loss factor is given by $tan\varphi = c\omega/k$, so rearranging the Eq. (3) k_{21} is expressed as

$$k_{21} = k(1 + itan\varphi).$$

(4)

It is possible to see that $tan\varphi$ is taking the position of the loss modulus k_2. The model is constructed based on the concepts illustrated in Figure 3.

Figure 3: Concept of cross dynamic stiffness transfer.
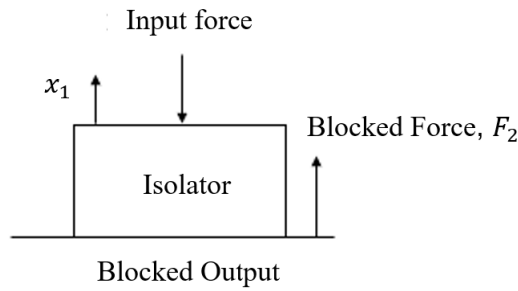
Source: adapted from Ooi and Ripin (2010).

As φ represents the phase angle between the force F_2 and the displacement x_1, so the loss modulus can be found through the receptance H_{21} where the loss factor η is extracted.

$$\eta = tan\varphi = \frac{-Im\{H_{21}(i\omega)\}}{Real\{H_{21}(i\omega)\}}.$$

(5)

The loss modulus k_2 is given by $k_2 = k_1\eta$.

From the information of the loss modulus, the damping ratio ζ can be determined.

As mentioned in sources such as Gade and Herlufsen (1994) and Soovere and Drake (1985), the correlation between ζ used is $\eta = 2\zeta = \frac{1}{Q}$, where Q is the quality factor.

This correlation is often accepted, however, its accuracy depends on the damping value. The correlation between these three parameters is given by the following expression (Nashif; Jones; Henderson, 1985) and (Graesser; Wong, 1991):

$$Q^{-1} = 2\zeta = \sqrt{1 + \eta} - \sqrt{1 - \eta} \,. \tag{6}$$

After some algebraic manipulations, the relationship between ζ and η can be written as

$$\eta = 2\zeta\sqrt{1 - \zeta^2} \,. \tag{7}$$

The relationship from de $\eta = 2\zeta$ remains within 5% accuracy if η is between $0 \leq \eta \leq 0.3$. Figure 4 shows the difference between $\eta = 2\zeta$ and $\eta = 2\zeta\sqrt{1 - \zeta^2}$.

Figure 4: Relationship between loss factor η and the damping ratio ζ with the two mathematical relationships used above.
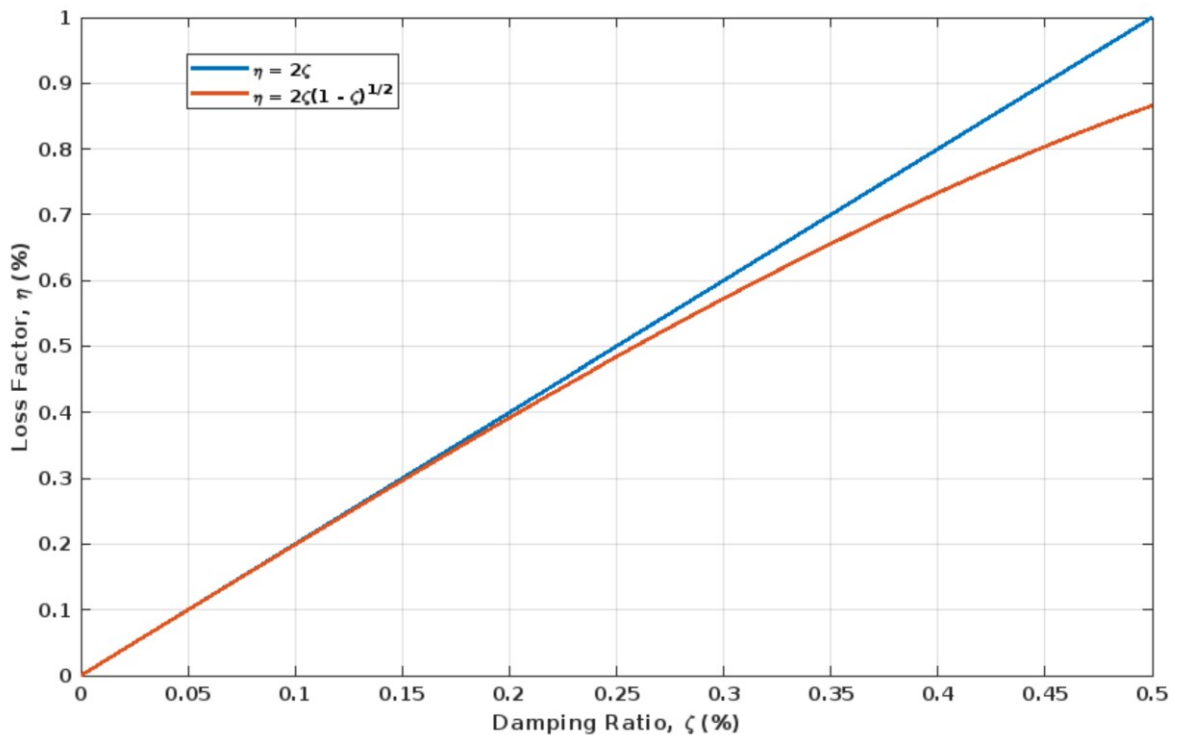
Source: adapted from Petrone (2014).

2.2 RUBBER MOUNTS

Elastomeric mounts have been used to isolate engines for decades. Many changes have been made over the years to improve the performance of this type of system.

Elastomeric mounts are designed with stiffness values to achieve good vibrational isolation in all directions. Due to the elastomeric material being cheaper and the production process simpler compared to other types of mounts, its cost ends up being more competitive. Additionally, these mounts are more compact and do not require maintenance. As mentioned by Swanson (1993), elastomeric mounts can be represented by the Kelvin-Voigt model, with the base being rigidly fixed and the force and displacement coming from the suspended mass. Figure 5 shows a graphical representation of this model.

Figure 5: Model of a single degree of freedom system being driven by the mass.
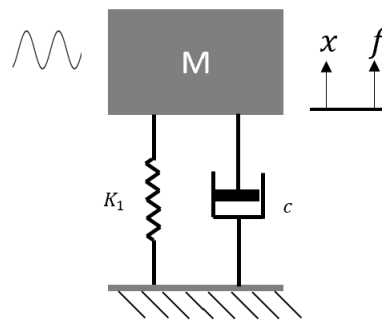
Source: adapted from Griffin (1990).

It is worth mentioning that Figure 1 shows a system with different behavior of the system of Figure 5 since in the former there is no restriction of motion on the base.

Swanson (1993) also stated that elastomeric mounts present a linear dynamic stiffness, which increases with frequency due to the damping effect. This behavior is depicted in Figure 6.

Figure 6: Dynamic stiffness of an elastomeric mount.
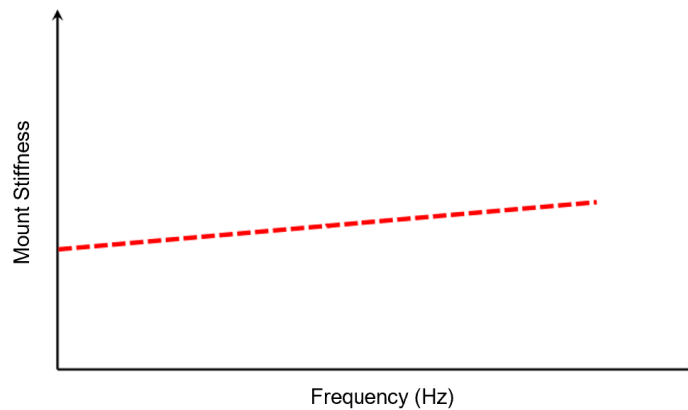
Source: adapted from Yu, Naganathan and Dukkipati (2001).

Designing a mounting system that meets a wide range of project requirements is a challenging task. A mount with high stiffness or high damping can provide high vibrational isolation at low frequencies, but its performance at high frequencies may result in low vibrational isolation, leading to undesired project performance levels. On the other hand, low stiffness and low damping result in high vibrational isolation performance at high frequencies, but low-frequency phenomena involving rigid body modes may be induced due to excitations, such as transient vibration signals.

To meet the pre-established requirements of mounts project, a compromise is necessary to achieve a balance between isolating the powertrain and preventing unwanted rigid body mode movements.

According to Rivin (1985), there are several ways to achieve the desired performance between low and high frequencies. For example, the application of Constant Natural Frequency (CNF) mounts, where the stiffness is proportional to the load on the mount. However, since the natural frequency in this type of system is directly proportional to stiffness and inversely proportional to load, the load's influence is canceled out, leading the CNF mount to have a constant natural frequency, obviously within a load range. Another possibility mentioned by Rivin (1985) is the use of a system where there is a spring in series with the Kelvin-Voigt model damper. In this condition, it is possible to have a high dependence of stiffness and damping on frequency.

Figure 7: Comparison between the Kelvin-Voigt model and the Modified Kelvin-Voigt model with a spring K_2 in series with the damper. Assuming K_2 has the same stiffness as K_1. Consideration of the model with input motion at the base.
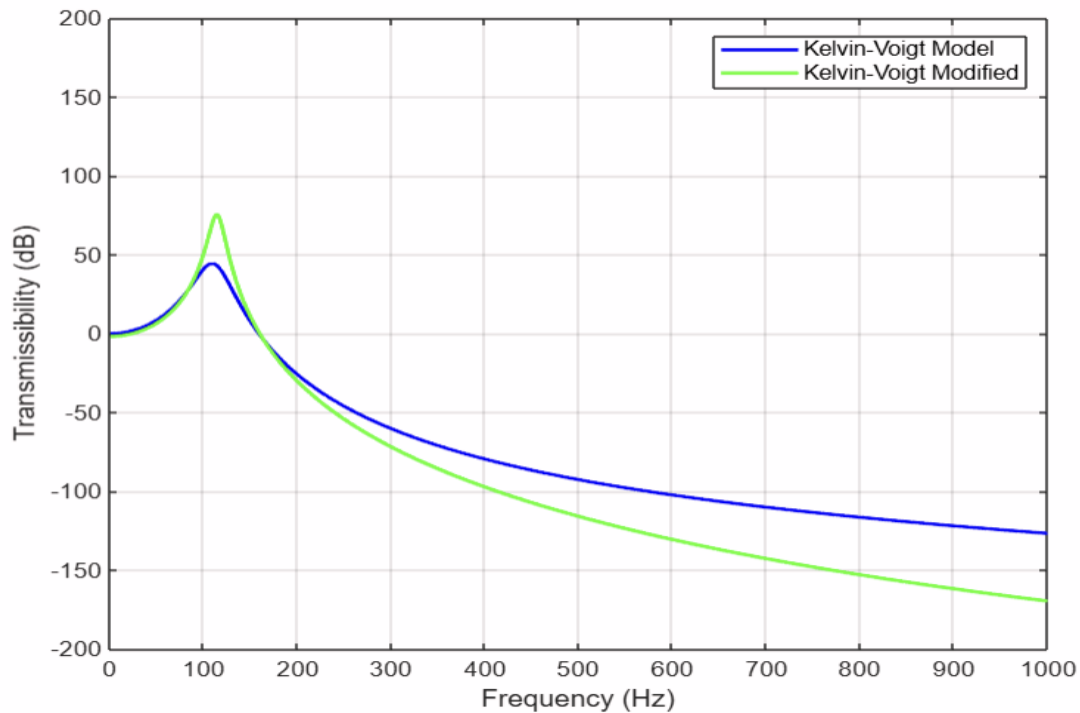
Source: the author.

As can be seen in Figure 7, the Modified Kelvin-Voigt system with the spring K_2 in series with the damper generated a high stiffness dependence on frequency. It is worth noting that the spring K_2 does not refer to the loss modulus. It is important to mention that in the graph of Figure 7, a smaller damping was used in the modified model.

These alternatives described only contribute to a better utilization of the elastomeric mount's performance. However, as previously described, the solution for a conventional elastomeric mount is a compromise between isolating the powertrain and preventing unwanted rigid body mode movements.

For electric motor applications, it is necessary to take into account the natural frequency of the rubber mount itself. As explained by Lion (2020) the frequency excitation of electric synchronous motor, which are most used in vehicles, typically operates within a frequency range from 10 to 300 Hz. However, the influence of the harmonics of electromagnetic orders of the stator and the number of poles can extend the frequency to a much higher frequency range as mentioned by Jagasics and Vajda

(2016). For instance, the natural frequency value of a cylindrical rubber mount would be about 630 Hz according to Lion (2020).

Therefore, analyzing mount isolation becomes more complex and the rigid body approach of the motor cannot also be considered.

One of the technologies developed to deal with electric motors is the second-stage mount model (Zhang; Liu, 2022), which presents a better vibration damping performance than original rubber mounts (Kruse; Carre, 2012). One way to predict the isolation performance of the rubber mount is to use constitutive models, for example, Kelvin-Voight and Maxwell models to obtain the dynamic stiffness through the finite element simulation method (Lee; Shin; Msolli, 2017, Cao; Sadeghi; Stacke, 2016, Davalos; Caldino-Herrera; Cornejo-Monroy, 2021). Another way to predict the isolation performance of the mount is to use the dynamic models, such as the fractional derivative model, to obtain the dynamic stiffness through the analytical calculation method (Shi; Wu, 2016, Lin; Schomburg, 2003).

Peng (2021) calculated the dynamic stiffness of the rubber isolator from 10-1000Hz through the finite element method by the generalized Maxwell model and presented how the parameters of the model were identified. The calculation of the force at the base end and at the motor end of the rubber isolator under high-frequency excitation was performed by the differential method and the segment method (Lion, 2020).

Hazra (2020) and Kruse and Carre (2012) calculated the high-frequency dynamic stiffness (50-2000 Hz) of a rubber mount with second-stage isolation through finite element simulation, on top of that a comparison with the original mount was done and the second-stage isolation mount presented a better vibration damper performance.

Zhang and Liu (2022) proposed a high-frequency dynamic model by the fractional derivative method for the second-stage mount. A graphical representation of the model is shown in Figure 8, where k_{cc}, k_{zz1}, k_{zz2} are the stiffness of springs; b_c, b_{z1} and b_{z2} are the viscous force damping coefficients of the fractional derivative elements; a_c, a_{z1} and a_{z2} are the fractional derivative orders of the fractional derivative elements.

Figure 8: High-frequency dynamic model utilizing the fractional derivative method.
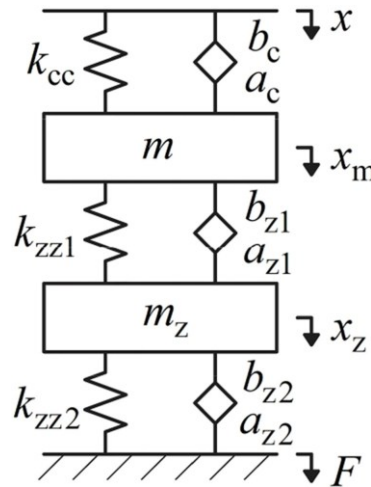
Source: adapted from Zhang and Liu (2022).

With this model they compare the dynamics stiffness of the first and second-stage with a finite element model. Figures 9 and 10 present the comparison of the fractional derivative model and the finite element model.

Figure 9: Comparison of the dynamic stiffness result of the first-stage isolation of the finite element model versus the fractional derivative model.
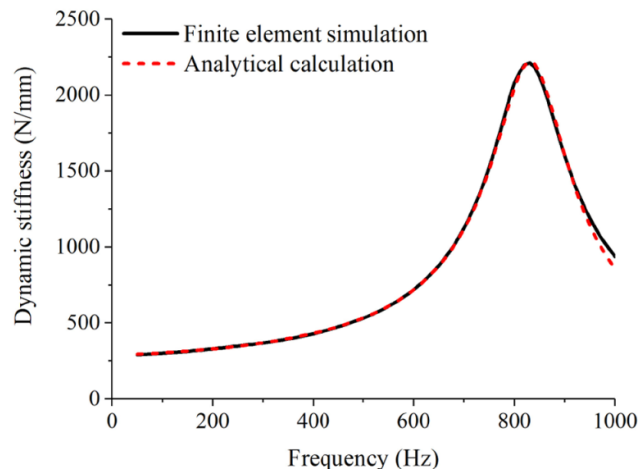
Source: adapted from Zhang and Liu (2022).

Figure 10: Comparison of the dynamic stiffness result of the second-stage isolation of the finite element model versus the fractional derivative model.
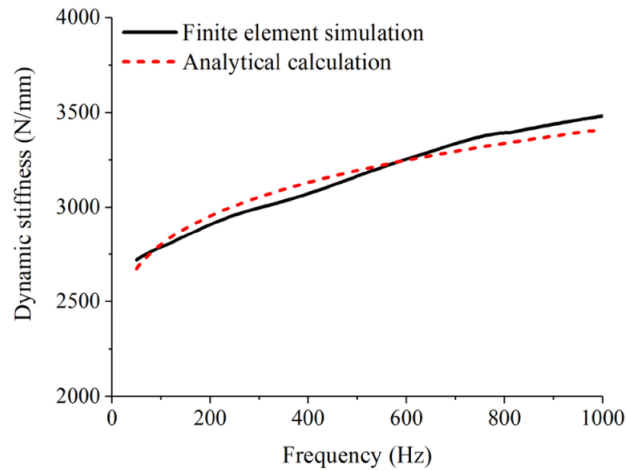
Source: adapted from Zhang and Liu (2022).

As it can be seen, the fractional derivative model presented a very good correlation with the finite element model in high-frequency for the first and second-stage.

2.3 HYDRAULIC PASSIVE MOUNTS

The need for a mount with high damping at low excitation frequencies and low damping at high excitation frequencies has led to the development of new isolation concepts, such as the hydraulic mount.

There are several types of hydraulic mounts, such as the single orifice hydraulic mount, the hydraulic mount with an inertia track, and the hydraulic mount with an inertia track and a decoupler. Follow the sequence for more details about the hydraulic mount with an inertia track and a decoupler, as it provides a clear understanding of the concepts and advantages of hydraulic mounts.

The hydraulic mount with an inertia track and a decoupler is a device that provides the desired damping characteristics by implementing a mechanical switching mechanism known as a decoupler along with a narrow channel that produces high fluid restriction. This channel is technically called an inertia track, as mentioned by Flower (1985). Figure 11 presents more details of the components of the hydraulic mount.

Figure 11: Hydraulic mount with inertia track and decoupler image.
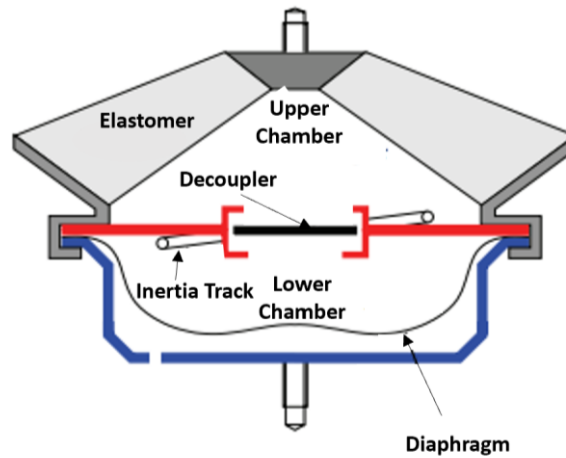
Source: adapted from Christopherson, Mahinfalah and Jazar (2012).

Large amplitudes in the low-frequency ranges transmit significant fluid movement, enough to force the decoupler to the bottom of the cage surrounding it, thus forcing the fluid to flow through the inertia track to the lower chamber. The inertia track is a long, narrow tube that extends circumferentially around the mount, providing a highly restrictive flow path between the upper and lower chambers.

Due to the restrictive nature of the inertia track, there is an increase in viscous damping in the system. This increase in damping acts to reduce transmissibility at low excitation frequencies. However, at high frequencies, the decoupler does not reach the bottom of the cage. Instead, it moves up and down freely, providing little flow restriction.

Because of the low flow restriction that the decoupler now has, the flow redirects from the inertia track to the decoupler, thereby reducing damping. The effects of the inertia track on the mount performance were studied by Lee, Choi and Hong (1994) and the assessed parameters were the diameter and the length of the inertia track.

The increase of the area of the inertia track increases the amplitude, frequency and damping of the mount. Figures 12 and 13 show these effects.

Figure 12: Effect of the intertia track in the amplitude and frequency. A_i is the area of the inertia track.
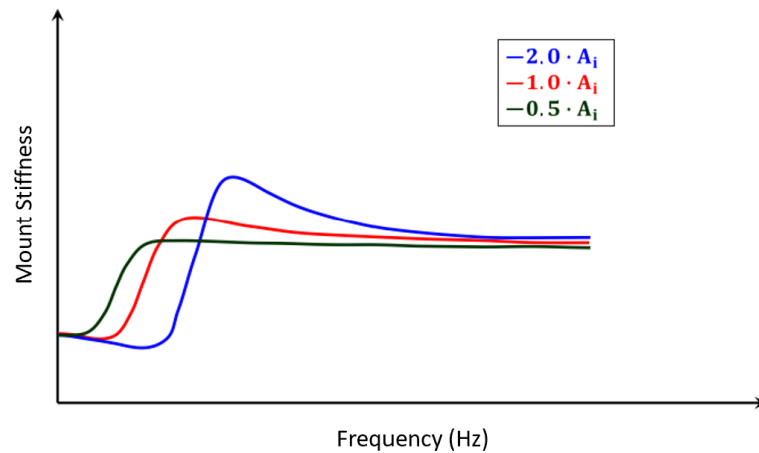
Source: adapted from Lee, Choi and Hong (1994).

Figure 13: Effect of the intertia track in the damping. A_I is the area of the inertia track.
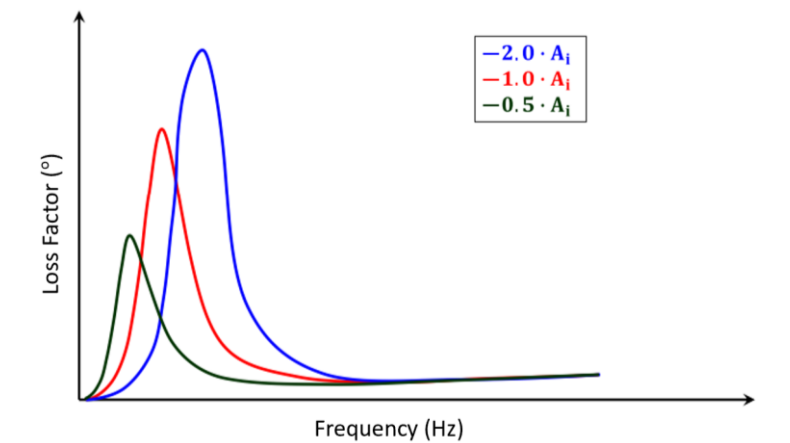
Source: adapted from Lee, Choi and Hong (1994).

Many authors tried to create a dynamic hydraulic mount model of one degree of fredroom (Bernuchon, 1984, Clark, 1985, Corcoran; Ticks, 1984, Lee; Choi; Hong, 1994, Royston; Singh, 1995, Seto; Sawatari, 1991), however a more detailed analysis of the hydraulic mount requires the consideration of the fluid mass, therefore more degrees of freedom are necessary (Seto; Sawata, 1991, Lee; Choi; Hong, 1994, Royston; Singh, 1995). The classical hydraulic mount is illustrated in Figure 14. It is clearly perceptible that the hydraulic mount is similar to the rubber mount with the addition of the fluid mass m and the stiffness k_2 representing the stiffness of the chambers which contain the fluid.

Figure 14: Model of the hydraulic mount.
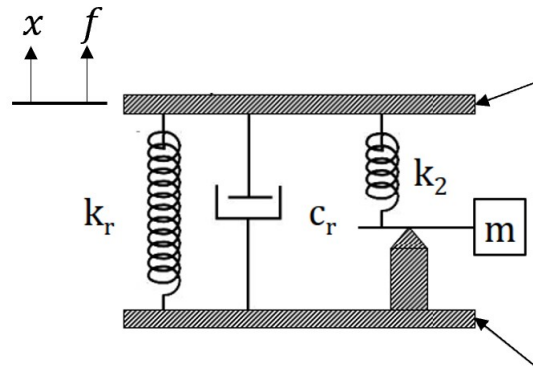
Source: adapted from Yu, Naganathan and Dukkipati (2001).

When modeling the inertia track, the assumptions usually made are (Wang; Lu; Ichiro, 2001):

- The fluid is incompressible;
- The influence of gravity is neglected;
- The properties are uniform at cross-sections at the beginning and the end of the inertia track;
- The relative velocity of the fluid along the track is constant;
- The inertia track is straight;
- Cross-sections taken along the track have the same shape.

The hydraulic inertance is defined as the pressure per unit volume velocity (Massey; Ward-Smith, 2006). For a circular tube, the following equation can be used to estimate I_i, the inertance of the inertia track:

$$I_i = \frac{\rho l_i}{A_i}, \tag{8}$$

where l_i is the effective length of the inertia track, A_i is the cross-sectional area of the inertia track and ρ is the density of the fluid. According to Adiguna et al. (2003) this is an acceptable approximation as more accurate approximations would require lengthy analysis. The effective length is not necessarily the actual length. It is likely to be between 1.0 and 1.33 times greater. This is because when the track stops the flow does not cease, but carries on into the chamber a short way.

Generally, the resistance to flow R relates the change in pressure p across a tube to the flow rate through the tube q as

$$q = \frac{p}{R} .$$
(9)

The resistance to flow was assumed by Singh, Kim and Ravindra (1992) to be constant and given by:

$$R_i = \frac{128 \mu l_i}{\pi d_i^4} ,$$
(10)

where μ is the viscosity of the fluid and d_i is the hydraulic diameter. For this the flow is assumed to be laminar and through a circular tube.

The resistance to flow is, in fact, the gradient of the graph of the steady state pressure drop Δp_{12} versus the steady flow rate q_i (Adiguna et al., 2003). This relationship is non-linear. The linear equation underestimates the actual resistance as it does not take into account end effects and pressure drop due to cornering. It also does not take into account turbulent flow that might be caused by the sharp edge orifice. A more suitable equation is suggested by Adiguna et al. (2003) to describe the non-linear relationship between Δp_{12} and q_i; the sharp edge orifice formula:

$$q_i = C_d A_i \sqrt{\frac{2 \Delta p_{12}}{\rho}} ,$$
(11)

where C_d is the coefficient of discharge, is dependent on the edges, surface finishes and roundness of the hole. For a perfectly sharp edge C_d is 0.60, a chamfered edge can change it to be up to 0.90 and a radius could increase it to 0.98 (Baillio, 2003).

However, chamfers and radius are difficult to recreate and can create extra variables to consider when trying to predict flow. The best method for getting a value for resistance is by curve fitting to experimental results. However, in the work of Adiguna et al. (2003) the non-linear sharp edge orifice formula gives a value of the right order of magnitude, whereas their values with the linear formula differed by an order of magnitude.

Ohadi and Maghsoodi (2007) also consider turbulent terms for the resistance to flow. Ahmadi et al. (2008) studied this effect both experimentally and using a computer

fluid behaviour simulation. They found close agreement between the model and the experiment and the curve was quadratic (see Figure 15). They found the relationship to be:

$$\Delta p_{12} = 2.23 q_i^2 + 0.07 q_i. \tag{12}$$

Figure 15: Pressure flow relantionship for the inertia track.
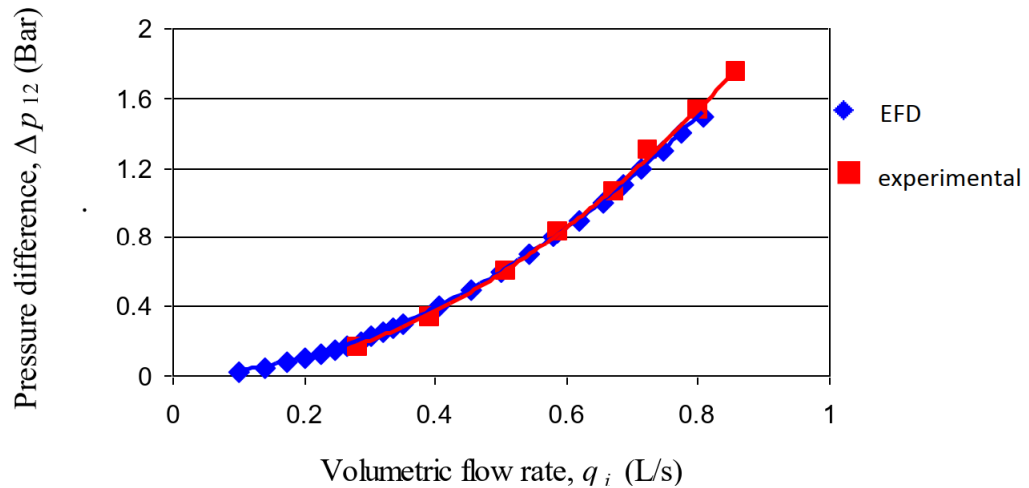
Source: adapted from Ahmadi et al. (2008).

2.4 OPTIMIZATION CONCEPTS

The goal of the optimization is to identify a point that minimizes a function, subject to equality and/or inequality constraints, as described by Arora (2012). In mathematical terms, an optimization problem is formulated as follows:

$$
\begin{aligned}
& min \, f(\{X\}) \\
& {}_j(\{X\}) = 0; j = 1 \, to \, p \\
& g_i(\{X\}) \leq 0; i = 1 \, to \, m,
\end{aligned}
\tag{13}
$$

where $\{X\}$ represents the set (vector) of the design variables (the adjustable parameters during the optimization process), f denotes the objective function, h_j corresponds to the equality constraints, and g_i to the inequality constraints.

There are some techniques to solve the problem of Eq. (13) and one of the them is the interior-point using the primal-dual logarithmic barrier method (PDLB) which is considered a robust and efficient approach (Delgado, 2016).

In the PDLB method, the inequality constraints from Eq. (13) are transformed into equalities by introducing positive slack variables s_i. This leads to the modified problem presented in Eq. (14)

$$
\begin{aligned}
&min\ f(\{X\}) \\
&h_j(\{X\}) = 0; j = 1\ to\ p \\
&g_i(\{X\}) + s_i = 0;\ i = 1\ to\ m.
\end{aligned}
\tag{14}
$$

Subsequently, a logarithmic barrier function is added to the objective function to ensure the non-negativity of the slack variables, as shown in Eq. (15).

$$
\begin{aligned}
&min\ f(\{X\}) - \mu \sum_i ln(s_i) \\
&h_j(\{X\}) = 0; j = 1\ to\ p \\
&g_i(\{X\}) + s_i = 0;\ i = 1\ to\ m,
\end{aligned}
\tag{15}
$$

where μ is referred to as the barrier parameter and the $ln(s_i)$ is called the logarithmic barrier function.

Thus, the following logarithmic barrier Lagrangian function is obtained:

$$
L(\{X_k\}) = f(\{X_k\}) + \mu \sum_{i=1}^{m} ln(s_i) + \sum_{i=1}^{m} u_{k,i} \nabla^2 g_i(\{X_k\}) + \sum_{i=1}^{p} v_{k,i} \nabla^2 h_i(\{X_k\}).
\tag{16}
$$

The necessary condition of 1st order is applied to the barrier Lagrangian logarithmic barrier function, Eq. (16), resulting in a system of nonlinear equations as shown in Eq. (17):

$$
\nabla L(\{X_k\}) = \begin{bmatrix} \nabla f(\{X\}) + [J_h]^T\{v\} + [J_g]^T\{u\} \\ \{u\} - \mu\{s\}^{-1} \\ \{h(\{X\})\} \\ \{g(\{X\})\} + \{s\} \end{bmatrix} = 0,
\tag{17}
$$

here $[J_g]$ denotes the Jacobian of the constraint functions $\{g(\{X\})\}$ and $[J_h]$ denotes the Jacobian of the constraint functions $\{h(\{X\})\}$.

The solution of the nonlinear system is given by the Newton's Method as in Eq (18)

$$
[W]\Delta\{d\} = -\nabla L(\{X_k\}),
\tag{18}
$$

where $\Delta\{d\}^T = (\Delta\{X\}, \Delta\{s\}, \Delta\{u\}, \Delta\{v\})$ and $[W]$ is given by

$$[W] = \begin{bmatrix} [H] & 0 & [J_h]^T & [J_g]^T \\ 0 & -\mu[S]^{-1} & 0 & [I] \\ [J_h] & 0 & 0 & 0 \\ [J_g] & [I] & 0 & 0 \end{bmatrix}. \tag{19}$$

$[H]$ is referred to as the Hessian matrix of the Lagrangian function where:

$$[H] = \nabla^2_{xx} L(\{X_k\}) = \nabla^2 f(\{X_k\}) + \sum_{i=1}^{m} u_{k,i} \nabla^2 g_i(\{X_k\}) + \sum_{i=1}^{p} v_{k,i} \nabla^2 h_i(\{X_k\}). \tag{20}$$

And the submatrix $[S]$ is give by

$$[S] = \begin{bmatrix} \dfrac{\mu}{(s_1)^2} & 0 & 0 \\ 0 & \ddots & 0 \\ 0 & 0 & \dfrac{\mu}{(s_m)^2} \end{bmatrix}. \tag{21}$$

The vector of the variables $\{X\}$, $\{s\}$, $\{u\}$ and $\{v\}$ are updated according to

$$\begin{aligned} \{X_{k+1}\} &= \{X_k\} + \alpha_p \Delta\{X_k\} \\ \{s_{k+1}\} &= \{s_k\} + \alpha_p \Delta\{s_k\} \\ \{v_{k+1}\} &= \{v_k\} + \alpha_d \Delta\{v_k\} \\ \{u_{k+1}\} &= \{u_k\} + \alpha_d \Delta\{u_k\}, \end{aligned} \tag{22}$$

α_p and α_d are the steps used in the update of the primal and dual variables, respectively.

In case of interest on how the α_p and α_d are calculated further details can be found in Granville (1994) and Torres, Quintana and Medina (2000).

3 SIX DOF MOTOR MODEL AND MOUNT ISOLATION MODEL

In order to begin evaluating the vibrational behavior of the mount project, the first step is to create an analytical model of six degrees of freedom for a general case of N mounts, bearing in mind that, afterward, the model can be used for any mount project whatever be the number of mounts.

The analytical model developed in this chapter is essential to estimate the modal parameters of the system required in the optimization process to reach a high modal purity.

As part of the optimization problem, the isolation performance is evaluated. A transmissibility model of the mount is created and integrated into the problem together to the modal purity problem with the objective to optimize the isolation performance of the mount in the mid-frequency range.

3.1 MATHEMATICAL MODEL OF SIX DOF OF THE MOTOR FIXED WITH MOUNTS

To determine the rigid body modes of the motor, the first step is to develop a mathematical model for this purpose. There are six degree of fredoom for a rigid body mode, three modes of translation and another three of rotation (Lin; Tsay, 2011). For the construction of the model, an important condition must be satisfied, which is the suspension of the structure on slightly rigid springs (Park; Singh, 2010). The importance of this condition is to ensure a high modal modal purity. According to Tahir (2018) a high modal purity of a mode means a high kinetic energy of this respective mode, the kinetic energy of the mode will be discussed in further detail in Chapter 4.

The greater the modal purity, the greater the decoupling of each degree of freedom in each direction. This is important to reduce the vibrational effects transmitted given the input of a certain force in a certain direction and also for better control of the vibrational distribution of the system in the low-frequency range.

For the model of the motor suspended on the mounts, six degrees of freedom (DOF) are used to determine the rigid body modes. A schematic representation of the suspended motor is shown in Figure 16.

Figure 16: Schematic illustration of a motor suspended on four mounts.
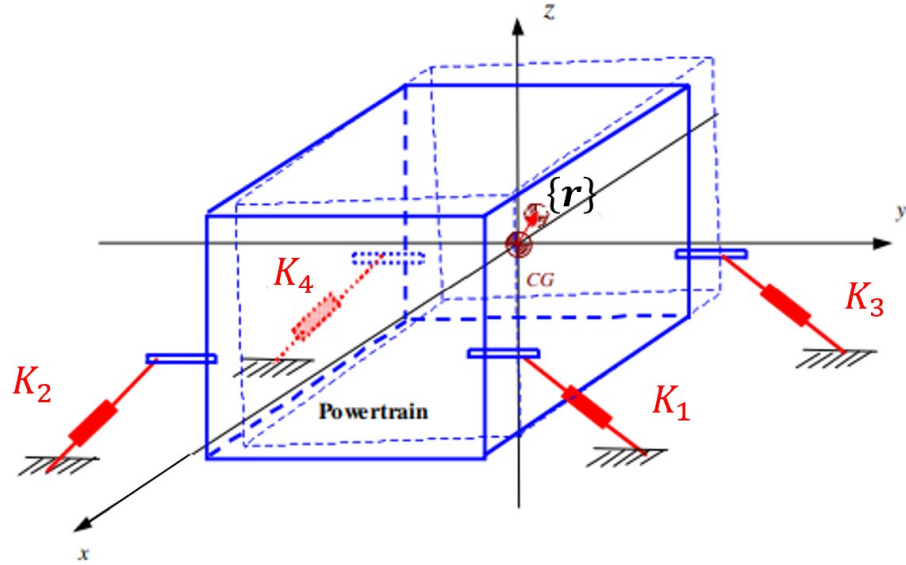
Source: adapted from Park and Singh (2010).

Considering that the forces and displacements of a motor are assumed to be periodic, they can be expressed as the sum of harmonic functions (Hafidi; Martin, 2010). This assumption allows for a simplified, but at the same time quite reasonable approach. They are represented as:

$$\{\tilde{\mathbf{R}}\}_G = \{\mathbf{R}\}_G e^{i\omega t}, \tag{23}$$

$$\{\tilde{\mathbf{F}}\} = \{\mathbf{F}\} e^{i\omega t}. \tag{24}$$

The motion equation will be formulated in matrix form based on the vector $\{\boldsymbol{R}\}_G$, which represents the displacement vector at the center of gravity (CG) in global coordinates.

$$\{\boldsymbol{R}\}_G = \begin{bmatrix} \{\boldsymbol{R}_t\}_G \\ \{\boldsymbol{R}_\theta\}_G \end{bmatrix}. \tag{25}$$

The motion equation is formed by the reaction forces of elastic and damping nature, and is given by the following relation:

$$[\mathbf{M}]\{\ddot{\mathbf{R}}\}_G + [\mathbf{C}]\{\dot{\mathbf{R}}\}_G + [\mathbf{K}]\{\mathbf{R}\}_G = \{\mathbf{F}\}. \tag{26}$$

As it deals with harmonic displacements and forces, Eq. (26) can be rewritten as:

$$-\omega^2[\mathbf{M}]\{\mathbf{R}\}_G + i\omega[\mathbf{C}]\{\mathbf{R}\}_G + [\mathbf{K}]\{\mathbf{R}\}_G = \{\mathbf{F}\}. \tag{27}$$

The displacement $\{R_i\}_G$ at each mount in the global coordinate located at the CG (in this case, the center of mass and center of gravity are coincident) can be written based on the displacement of the motor's center of mass by the following equation:

$$\{R_i\}_G = \{R_t\}_G + \{R_\theta\}_G \times \{r_i\}_G, \tag{28}$$

where $\{R_t\}_G$ represents the translational displacement vector in the global coordinate, $\{R_\theta\}_G$ represents the rotational displacement vector in the global coordinate, and $\{r_i\}_G$ represents the position vector of the *i*-th mount in the global coordinate.

The vector $\{R_i\}_G$ can also be written as:

$$\{R_i\}_G = \big[[\mathbf{I}][\mathbf{H}_i]\big]\{\mathbf{R}\}_G, \tag{29}$$

where $[\mathbf{I}]$ is the 3 x 3 identity matrix and $[\mathbf{H}_i]$ is a skew-symmetric matrix (Haug, 2021):

$$[\mathbf{H}_i] = \begin{bmatrix} 0 & r_{iz} & -r_{iy} \\ -r_{iz} & 0 & r_{ix} \\ r_{iy} & -r_{ix} & 0 \end{bmatrix}. \tag{30}$$

If there are rotations in the local coordinate system of each mount, it is necessary to apply the rotation transformation matrix. Therefore, the displacement vector of the i-th mount in the local coordinate $\{R_i\}_L$ is given by:

$$\{R_i\}_L = \begin{bmatrix} \{R_{i,t}\}_L \\ \{R_{i,\theta}\}_L \end{bmatrix} = [\mathbf{\Theta}_i] \begin{bmatrix} [\mathbf{I}] & [\mathbf{H}_i] \\ \mathbf{0} & [\mathbf{I}] \end{bmatrix} \{\mathbf{R}\}_G. \tag{31}$$

where $[\mathbf{\Theta}_i]$ is the rotational transformation matrix of the i-th mount constructed with the Euler angles around the global coordinate system in the sequence X, Y, and Z (Crede, 1965). Here, θ_{1i}, θ_{2i} e θ_{3i} are the rotation angles around the respective X, Y, and Z axes.

$$[\mathbf{\Theta}_i] = \begin{bmatrix} C\theta_{2i}C\theta_{3i} & S\theta_{1i}S\theta_{2i}C\theta_{3i} - C\theta_{1i}S\theta_{3i} & C\theta_{1i}S\theta_{2i}C\theta_{3i} + S\theta_{1i}S\theta_{3i} \\ C\theta_{2i}S\theta_{3i} & S\theta_{1i}S\theta_{2i}C\theta_{3i} + C\theta_{1i}S\theta_{3i} & C\theta_{1i}S\theta_{2i}C\theta_{3i} - S\theta_{1i}S\theta_{3i} \\ -S\theta_{2i} & S\theta_{1i}C\theta_{2i} & C\theta_{1i}C\theta_{2i} \end{bmatrix}, \tag{32}$$

where C and S represent the cosine and sine functions.

From Eq. (31), it is possible to find the local translational force $\{f_{i,t}\}_L$ at each mount:

$$\{f_{i,t}\}_L = [k_i]_L\{R_{i,t}\}_L = [k_i]_L[\Theta_i][[I]\ [H_i]]\{R\}_G, \tag{33}$$

where $[k_i]_L$ is the diagonal matrix at the local coordinate, given by:

$$[k_i]_L = \begin{bmatrix} k_{ix} & 0 & 0 \\ 0 & k_{iy} & 0 \\ 0 & 0 & k_{iz} \end{bmatrix}. \tag{34}$$

The vector $\{f_i\}_G$ is given by the translational forces and the moments produced from the translational forces $\{f_{i,t}\}_G$, represented by the following expression:

$$\{f_i\}_G = \begin{Bmatrix} \{f_{i,t}\}_G \\ \{f_{i,\theta}\}_G \end{Bmatrix} = \begin{Bmatrix} \{f_{i,t}\}_G \\ \{r_i\}_G \times \{f_{i,t}\}_G \end{Bmatrix} = \begin{bmatrix} [I] \\ [H_i^T] \end{bmatrix}\{f_{i,t}\}_G. \tag{35}$$

It is important to note that Eq. (35) considers only the torque produced by the translation of the motor and disregards the torque from rotational stiffness as it is a non-dominant component in this type of system (Hafidi, 2010).

However, $\{f_{i,t}\}_G$ can also be written as $\{f_{i,t}\}_G = [\Theta_i]^{-1}\{f_{i,t}\}_L$, but since the transformation matrix $[\Theta_i]$ is orthogonal, then , $\{f_{i,t}\}_G = [\Theta_i]^T\{f_{i,t}\}_L$. Thus, $\{f_i\}_G$ takes the following form shown:

$$\{f_i\}_G = \begin{bmatrix} [I] \\ [H_i^T] \end{bmatrix}[\Theta_i]^T[k_i]_L[\Theta_i][[I]\ [H_i]]\{R\}_G. \tag{36}$$

The global matrix stiffness $[k_i]_G$ appears as the product of $[\Theta_i]^T[k_i]_L[\Theta_i]$ and the position matrix $[B_i]$ as $[[I]\ [H_i]]$.

Thus $\{f_i\}_G$ can be rewritten as:

$$\{f_i\}_G = [B_i]^T[k_i]_G[B_i]\{R\}_G. \tag{37}$$

Therefore, the total reaction force $\{F_k\}_G$ associated with the stiffness can be given by:

$$\{\mathbf{F}_k\}_G = \sum_{i=1}^{N} [B_i]^T [k_i]_G [B_i]\{\mathbf{R}\}_G. \tag{38}$$

With the considerations above, the Eq. (34) can be extended to the reaction forces related to the damping of the system, where now the local matrix $[c_i]_L$ is the damping matrix and presents the following form:

$$[c_i]_L = \begin{bmatrix} c_{ix} & 0 & 0 \\ 0 & c_{iy} & 0 \\ 0 & 0 & c_{iz} \end{bmatrix}. \tag{39}$$

Replacing $[k_i]_L$ by $[c_i]_L$ in Eq. (38) yields:

$$\{\mathbf{F}_c\}_G = \sum_{i=1}^{N} [B_i]^T [c_i]_G [B_i]\{\mathbf{R}\}_G. \tag{40}$$

The generalized mass matrix of the powertrain is given by the following equation (Xu; Gong; Meng; Li, 2021):

$$[\mathbf{M}] = \begin{bmatrix} m & 0 & 0 & 0 & mz_d & -my_d \\ 0 & m & 0 & -mz_d & 0 & mx_d \\ 0 & 0 & m & my_d & -mx_d & 0 \\ 0 & -mz_d & my_d & I_{xxo} & -I_{xyo} & -I_{xzo} \\ mz_d & 0 & -mx_d & -I_{xyo} & I_{yyo} & -I_{yzo} \\ my_d & mx_d & 0 & -I_{xzo} & -I_{yzo} & I_{zzo} \end{bmatrix}. \tag{41}$$

In Eq. (41), m is the mass of the powertrain, (x_d, y_d, z_d) is the resulting vector of the distance from the powertrain's CG to the origin of the global coordinate system, $I_{xxo}, I_{yyo}, I_{zzo}, ...,$ are the inertia terms of the powertrain assembly about the origin of the global coordinate system. Since the center of gravity of the powertrain coincides with the origin of the global coordinate system, the generalized mass matrix is simplified to the following form:

$$[\mathbf{M}] = \begin{bmatrix} m & 0 & 0 & 0 & 0 & 0 \\ 0 & m & 0 & 0 & 0 & 0 \\ 0 & 0 & m & 0 & 0 & 0 \\ 0 & 0 & 0 & I_{xxo} & -I_{xyo} & -I_{xzo} \\ 0 & 0 & 0 & -I_{xyo} & I_{yyo} & -I_{yzo} \\ 0 & 0 & 0 & -I_{xzo} & -I_{yzo} & I_{zzo} \end{bmatrix}. \tag{42}$$

Therefore, Eq. (27) can be rewritten as:

$$-\omega^2[\mathbf{M}]\{\mathbf{R}\}_G + i\omega \sum_{i=1}^{N}[B_i]^T[c_i]_G[B_i]\{\mathbf{R}\}_G + \sum_{i=1}^{N}[B_i]^T[k_i]_G[B_i]\{\mathbf{R}\}_G = \{\mathbf{F}\}. \qquad (43)$$

From Eq. (43), it is possible to describe all rigid body motions of the powertrain, which are evaluated in subsequent chapters.

3.2 DESCRIPTION OF THE MODEL WITHOUT DAMPING

For an undamped MGL system with N degrees of freedom, the governing equations of motion can be written in matrix form as follows:

$$[\mathbf{M}]\{\ddot{\mathbf{R}}\} + [\mathbf{K}]\{\mathbf{R}\} = \{\mathbf{F}\}. \qquad (44)$$

We should first consider the free vibration solution (in order to determine the normal or natural modal properties) by setting $\{\mathbf{F}\} = 0$.

Under this condition, it should be consider a displacement solution of the form $\{\widetilde{\mathbf{R}}\} = \{\mathbf{R}\}\,e^{i\omega t}$.

Substituting these conditions into Eq. (44), the final result is expressed as:

$$([\mathbf{K}] - \omega^2[\mathbf{M}])\{\mathbf{R}\} = \{0\}. \qquad (45)$$

For which the only non-trivial solution is given by:

$$det\big[[\mathbf{K}] - \omega^2[\mathbf{M}]\big] = 0. \qquad (46)$$

From the solution of the equation above, we obtain the diagonal matrix of eigenvalues $[\ddot{\omega}_r^2.]$ and eigenvectors $[\mathbf{\Psi}]$ that form the modal model. Here, the eigenvalue $\bar{\omega}_r^2$ is the r-th eigenvalue or squared natural frequency.

The modal model has important properties known as orthogonality properties, which are as follows:

$$[\mathbf{\Psi}]^T[\mathbf{M}][\mathbf{\Psi}] = [\ddot{m}_{r.}], \qquad (47)$$

$$[\mathbf{\Psi}]^T[\mathbf{K}][\mathbf{\Psi}] = [\ddot{k}_{r.}], \qquad (48)$$

where the matrices $\left[\,\ddots m_r \ddots\,\right]$ and $\left[\,\ddots k_r \ddots\,\right]$ are called, respectively, the modal mass matrix and the modal stiffness matrix. From these matrices, we can also find the matrix of natural frequencies by the expression below:

$$\left[\,\ddots \overline{\omega}_r^2 \ddots\,\right] = \left[\,\ddots m_r \ddots\,\right]^{-1} \left[\,\ddots k_r \ddots\,\right]. \tag{49}$$

It is also possible to normalize the eigenvector matrix using the modal mass as:

$$[\boldsymbol{\Phi}] = [\boldsymbol{\Psi}] \left[\,\ddots m_r^{-\frac{1}{2}} \ddots\,\right]. \tag{50}$$

This normalization is crucial, because the modal mass and stiffness matrices can be rewritten as:

$$[\boldsymbol{\Phi}]^T [\mathbf{M}][\boldsymbol{\Phi}] = [\mathbf{I}], \tag{51}$$

$$[\boldsymbol{\Phi}]^T [\mathbf{K}][\boldsymbol{\Phi}] = \left[\,\ddots \overline{\omega}_r^2 \ddots\,\right]. \tag{52}$$

Returning now to the case where a set of external sinusoidal forces is applied $\{\widetilde{\mathbf{F}}\} = \{\mathbf{F}\}e^{i\omega t}$, all of the same frequency, ω, but with different amplitudes and phases, and similarly assuming a response of the form $\{\widetilde{\mathbf{R}}\}_G = \{\mathbf{R}\}_G e^{i\omega t}$. Therefore, returning to Eq. (45), but with the force being non-zero, the following relationship appears:

$$([\mathbf{K}] - \omega^2 [\mathbf{M}])\{\mathbf{R}\}e^{i\omega t} = \{\mathbf{F}\}e^{i\omega t}. \tag{53}$$

After some manipulations of the equation above, we find:

$$\{\mathbf{R}\} = ([\mathbf{K}] - \omega^2 [\mathbf{M}])^{-1}\{\mathbf{F}\}, \tag{54}$$

$$\{\mathbf{R}\} = [\alpha(\omega)]\{\mathbf{F}\}, \tag{55}$$

where $[\alpha(\omega)]$ is the N x N receptance matrix and forms the response model. Each element of the receptance matrix is the frequency response function (FRF) expressed generally as:

$$\alpha_{jk}(\omega) = \left(\frac{R_j}{F_k}\right), F_m = 0, m = 1, N; k \neq 0. \tag{56}$$

In practice, computing the FRFs for each value of ω is computationally infeasible due to the need to invert the matrix for each value of ω. Therefore, it is necessary to rewrite Eq. (56). For this, the following form is taken:

$$([\mathbf{K}] - \omega^2[\mathbf{M}]) = [\alpha(\omega)]^{-1}. \tag{57}$$

By pre-multiplying by $[\mathbf{\Phi}]^T$ and post-multiplying by $[\mathbf{\Phi}]$:

$$[\mathbf{\Phi}]^T([\mathbf{K}] - \omega^2[\mathbf{M}])[\mathbf{\Phi}] = [\mathbf{\Phi}]^T[\alpha(\omega)]^{-1}[\mathbf{\Phi}] \tag{58}$$

or

$$[(\overline{\omega}_r^2 - \omega^2)] = [\mathbf{\Phi}]^T[\alpha(\omega)]^{-1}[\mathbf{\Phi}], \tag{59}$$

resulting in:

$$[\alpha(\omega)] = [\mathbf{\Phi}][(\overline{\omega}_r^2 - \omega^2)]^{-1}[\mathbf{\Phi}]^T. \tag{60}$$

Therefore, each term $\alpha_{jk}(\omega)$ is given by:

$$\alpha_{jk}(\omega) = \sum_{r=1}^{N} \frac{(\phi_{jr})(\phi_{kr})}{\overline{\omega}_r^2 - \omega^2}. \tag{61}$$

The Eq. (61) allows the calculation of each FRF by the usage of the elements of the mass normalized eigenvector matrices. This is much simpler and informative than calculate the direct inverse of Eq. (54).

3.3 DESCRIPTION OF THE HYSTERETIC MODEL

For a system of MDOFs with hysteretic damping, with N degrees of freedom, the governing equations of motion can be written in matrix form as:

$$[\mathbf{M}]\{\ddot{\mathbf{R}}\} + [\mathbf{K}]\{\mathbf{R}\} + i[\mathbf{H}_k]\{\mathbf{R}\} = \{\mathbf{F}\}, \tag{62}$$

where $[\mathbf{H}_k]$ is the matrix of hysteretic damping. Similarly to what was done in the undamped system, we should first consider the free vibration solution (in order to determine the normal or natural modal properties) by setting $\{\mathbf{F}\} = 0$.

Under this condition, a displacement solution for Eq. (62) is of the form $\{\tilde{\mathbf{R}}\} = \{\mathbf{R}\}\, e^{i\lambda t}$.

Substituting these conditions into Eq. (44), the final result is expressed as:

$$([\mathbf{K}_c] - \omega^2[\mathbf{M}])\{\mathbf{R}\} = \{0\}, \tag{63}$$

where $[\mathbf{K}_c] = [\mathbf{K}] + i[\mathbf{H}_k]$, thus the only non-trivial solution is given by:

$$det\big[[\mathbf{K}_c] - \omega^2[\mathbf{M}]\big] = 0. \tag{64}$$

From the solution of the Eq. (64), it is obtained the diagonal matrix of eigenvalues $\begin{bmatrix} \ddots \lambda_r^2 \ddots \end{bmatrix}$ and eigenvectors $[\mathbf{\Psi}]$ that form the modal model, but now both the eigenvalues and eigenvectors belong to the set of complex numbers. Here, the eigenvalue λ_r^2 is the r-th eigenvalue and has the following form:

$$\lambda_r^2 = \omega_r^2(1 + i\eta_r), \tag{65}$$

where η_r is the damping loss factor. The same orthogonality properties mentioned for the undamped model apply here:

$$[\mathbf{\Psi}]^T[\mathbf{M}][\mathbf{\Psi}] = \begin{bmatrix} \ddots m_r \ddots \end{bmatrix}, \tag{66}$$

$$[\mathbf{\Psi}]^T[\mathbf{K}_c][\mathbf{\Psi}] = \begin{bmatrix} \ddots k_r \ddots \end{bmatrix}. \tag{67}$$

The eigenvalues can be directly found from the relationship between the modal mass matrix and the modal stiffness matrix, both of which are complex.

$$\begin{bmatrix} \ddots \lambda_r^2 \ddots \end{bmatrix} = \begin{bmatrix} \ddots m_r \ddots \end{bmatrix}^{-1} \begin{bmatrix} \ddots k_r \ddots \end{bmatrix}. \tag{68}$$

One can also normalize the eigenvector matrix using the modal mass as:

$$[\mathbf{\Phi}] = [\mathbf{\Psi}] \begin{bmatrix} \ddots m_r^{-\frac{1}{2}} \ddots \end{bmatrix}. \tag{69}$$

This normalization is very important because the modal mass and stiffness matrices can be rewritten as:

$$[\mathbf{\Phi}]^T[\mathbf{M}][\mathbf{\Phi}] = [\mathbf{I}], \tag{70}$$

$$[\mathbf{\Phi}]^T[\mathbf{K}_c][\mathbf{\Phi}] = \left[\begin{smallmatrix}\ddots\\ & \lambda_r^2\\ & & \ddots\end{smallmatrix}\right]. \tag{71}$$

Returning now to the case where a set of external sinusoidal forces is applied $\{\widetilde{\mathbf{F}}\} = \{\mathbf{F}\}e^{i\omega t}$, all of the same frequency, ω, but with different amplitudes and phases, and similarly, we assume a response of the form $\{\widetilde{\mathbf{R}}\}_G = \{\mathbf{R}\}_G e^{i\omega t}$.

Using the same approach as the undamped modal model, we can write the inverse of the receptance matrix, but now with the matrix $[\mathbf{K}_c]$.

$$([\mathbf{K}_c] - \omega^2[\mathbf{M}]) = [\alpha(\omega)]^{-1}. \tag{72}$$

By pre-multiplying by $[\mathbf{\Phi}]^T$ and pos-multiplying by $[\mathbf{\Phi}]$ leads to:

$$[\mathbf{\Phi}]^T([\mathbf{K}_c] - \omega^2[\mathbf{M}])[\mathbf{\Phi}] = [\mathbf{\Phi}]^T[\alpha(\omega)]^{-1}[\mathbf{\Phi}] \tag{73}$$

or

$$[(\lambda_r^2 - \omega^2)] = [\mathbf{\Phi}]^T[\alpha(\omega)]^{-1}[\mathbf{\Phi}]. \tag{74}$$

This results in:

$$[\alpha(\omega)] = [\mathbf{\Phi}][(\lambda_r^2 - \omega^2)]^{-1}[\mathbf{\Phi}]^T. \tag{75}$$

Therefore, each term $\alpha_{jk}(\omega)$ for the hysteretic modal model is given by

$$\alpha_{jk}(\omega) = \sum_{r=1}^{N} \frac{(\phi_{jr})(\phi_{kr})}{\omega_r^2 - \omega^2 + i\eta_r\omega_r^2}, \tag{76}$$

From Eq. (76), the FRFs of the hysteretic model can be calculated using again the mass normalized eigenvectors, however, now, the hysteresis generates a phase and the numerator and denominator are complex numbers.

The mount isolation model in working condition is as important as the rigid body modes. Furthermore, the loads generated by the motor have to be considered what makes the assumptions involved in the study of isolation different from the ones of the rigid body modes because the isolation of higher frequencies should be considered. As mentioned by Hazra (2020) the electric motor mounts resonate at high structural frequencies in the range of 600 to 1000 Hz. For this reason, a range of frequencies below this range is considered to evaluate the mount isolation capability. This means

that the motor still behaves in an unyielding manner, so for this region the motor mount filtration can be evaluated as a rigid body mode.

The model is developed considering the mount damping and using the mechanical impedance theory. For this reason, a quick theory review is presented and the transmissibility function derived from the model is set.

3.4 MECHANICAL IMPEDANCE APPROACH

According to Harris and Piersol (2002), the mechanical impedance Z of a system is the ratio of a sinusoidal driving force F acting on the system to the resulting velocity v of the system. Its mechanical mobility Y is the inverse of the mechanical impedance.

Consider a sinusoidal driving F that has a magnitude F_0 and an angular frequency ω:

$$F = F_0 e^{i\omega t} . \tag{77}$$

The application of this force to a linear mechanical system results in a velocity v:

$$v = v_0 e^{i(\omega t + \theta)} , \tag{78}$$

where v_0 is the magnitude of the velocity and θ is the phase angle between F and v. Then, by definition, the mechanical impedance of the system Z (at the point of application of the force) is given by:

$$Z = \frac{F}{v} . \tag{79}$$

The idealized mechanical systems considered in this chapter are considered to be represented by combinations of basic mechanical elements assembled to form linear mechanical systems. These basic elements are mechanical resistances (dampers), springs, and masses.

A mechanical resistance is a device in which the relative velocity between the end points is proportional to the force applied to the end points. Such a device can be represented by the dashpot of Figure 17, in which the force resisting the extension (or

compression) of the dashpot is the result of viscous friction. An ideal resistance is assumed to be made of massless, infinitely rigid elements. The velocity of point A, v_1, with respect to the velocity at point B, v_2, is:

$$v = (v_1 - v_2) = \frac{F_a}{c} \,,$$ (80)

Figure 17: Mechanical resistance representation.
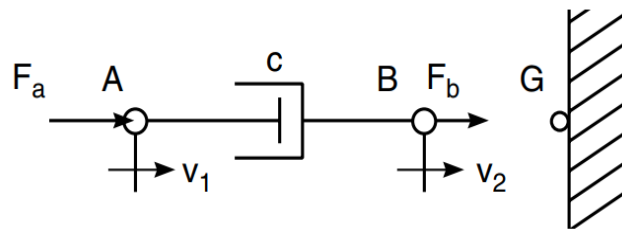
Source: adapted from Harris and Piersol (2002).

where c is a constant of proportionality called the mechanical resistance or damping constant. For there to be a relative velocity v as a result of force at A, there must be an equal reaction force at B. Thus, the transmitted force F_b is equal to F_a. The velocities v_1 and v_2 are measured with respect to the stationary reference G; their difference is the relative velocity v between the end points of the resistance.

With the sinusoidal force of Eq. (77) applied to point A with point B attached to a fixed (immovable) point, the velocity v_1 is obtained from Eq. (80) and can be written as

$$v_1 = \frac{F_0 e^{i\omega t}}{c} = v_0 e^{i\omega t} \,.$$ (81)

Because c is a real number, the force and velocity are said to be in phase. The mechanical impedance of the resistance is obtained by substituting from Eq. (77) and (79) in (81):

$$Z_c = \frac{F}{v} = c.$$ (82)

The mechanical impedance of a resistance is the value of its damping constant c.

The second basic element is the impedance of a linear spring. A linear spring is a device for which the relative displacement between its end points is proportional to the force applied. It is illustrated in Figure 18 and can be represented mathematically by:

$$x_1 - x_2 = \frac{F_a}{k},\tag{83}$$

where x_1, x_2 are displacements relative to the reference point G and k is the spring stiffness. The stiffness k can be expressed alternately in terms of a compliance C = 1/k.

The spring transmits the applied force, so that $F_a = F_b$.

Figure 18: Mechanical impedance representation of a spring.
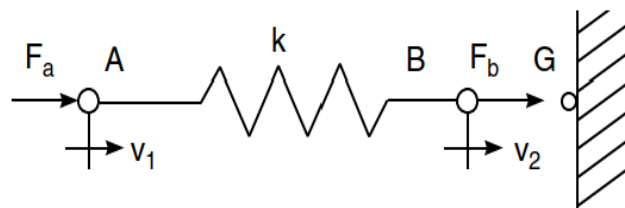
Source: adapted from Cyril (2002).

With the force of Eq. (77) applied to point A and with point B fixed, the displacement of point A is given by replacing this condition in Eq. (83), the result is

$$x_1 = \frac{F_0 e^{i\omega t}}{k} = x_0 e^{i\omega t}.\tag{84}$$

The displacement is thus sinusoidal and in phase with the force. The relative velocity of the end connection is required for impedance calculations and is given by the differentiation of x with respect to the time:

$$\dot{x} = v = \frac{i\omega F_0 e^{i\omega t}}{k} = \frac{\omega}{k} F_0 e^{i\left(\omega t + \frac{\pi}{2}\right)}.\tag{85}$$

Replacing Eqs. (77) and (92) in Eq. (79) the impedance of the linear spring can be found, given by

$$Z_k = -\frac{jk}{\omega}.\tag{86}$$

In the ideal mass illustrated in Figure 19, the acceleration $\ddot{x}$ of the rigid body is proportional to the applied force F:

$$\ddot{x}_1 = \frac{F_a}{m},$$ (87)

Figure 19: Mechanical impedance representation of a mass.
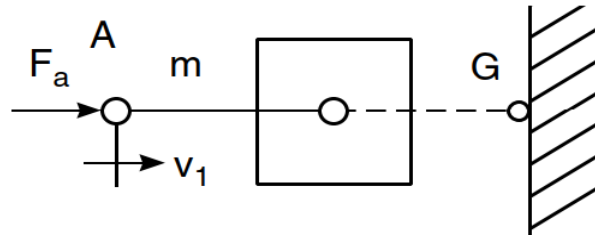
Source: adapted from Cyril (2002).

where m is the mass of the body. By Eq. (87), the force F_a is required to give the mass the acceleration $\ddot{x}_1$, and the force F_a is transmitted to the reference G. When a sinusoidal force is applied, the Eq. (87) becomes

$$\ddot{x}_1 = \frac{F_0 e^{i\omega t}}{m}.$$ (88)

The acceleration is sinusoidal and in phase with the applied force.
Integrating Eq. (88) to find velocity,

$$\dot{x}_1 = v = \frac{F_0 e^{i\omega t}}{i\omega m}.$$ (89)

The mechanical impedance of the mass is the ratio of F to v, so that

$$Z = \frac{F_0 e^{i\omega t}}{F_0 e^{i\omega t}/i\omega m} = i\omega m.$$ (90)

Thus, the impedance of a mass is an imaginary quantity that depends on the magnitude of the mass and on the frequency.

In analyzing the properties of mechanical systems, it is often advantageous to combine groups of basic mechanical elements into single impedances.

The parallel elements are the combination of elements shown in Figure 20, a spring and a mechanical resistance. They are said to be in parallel since the same

force is applied to both, and both are constrained to have the same relative velocities between their connections.

Figure 20: Representation of a parallel spring-resistance combination.
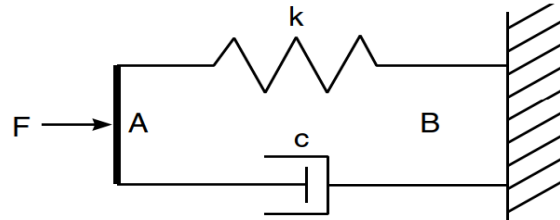
Source: adapted from Cyril (2002).

In this configuration, the force in both elements are summed, i.e.,

$$F = F_c + F_k. \tag{91}$$

By extending this concept to any number of parallel elements, the driving force F is equal to the sum of the resisting forces:

$$F = \sum_{i=1}^{n} vZ_i \ \text{ and } \ Z_p = v \sum_{i=1}^{n} Z_i, \tag{92}$$

where Z_p is the total mechanical impedance of the parallel combination of the individual elements Z_i.

Since mobility is the reciprocal of impedance, when the properties of the parallel elements are expressed as mobilities, the total mobility of the combination follows from Eq. (92):

$$\frac{1}{Y_p} = \sum_{i=1}^{n} \frac{1}{Y_i}. \tag{93}$$

Figure 21 represents a spring connected to a damper, so that the applied force passes through both elements to the inertial reference. Then the velocity v is the sum of v_k and v_c. This is a series combination of elements. The method for determining the mechanical impedance of the combination follows.

Figure 21: Representation of a series combination of a spring and a damper.
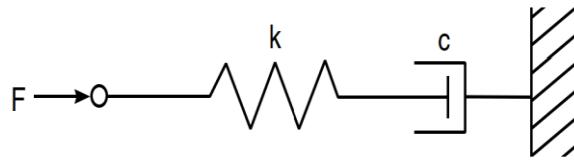
Source: adapted from Cyril (2002).

Consider the more general case of three arbitrary impedances shown in Figure 22.

Determine the impedance presented by the end of a number of series-connected elements. Elements Z_1 and Z_2 must have no mass, since a mass always has one end connected to a stationary inertial reference. However, the impedance Z_3 may be a mass.

The relative velocities between the end connections of each element are indicated by v_a, v_b, and v_c, and the velocities of the connections with respect to the stationary reference point G are indicated by v_1, v_2, and v_3:

$$v_3 = v_c \quad \text{and} \quad v_2 = v_3 + (v_2 - v_3) = v_c + v_b,$$
$$v_1 = v_2 + (v_1 - v_2) = v_a + v_b + v_c. \tag{94}$$

Figure 22: Representation of a generalized series combination of three elements.
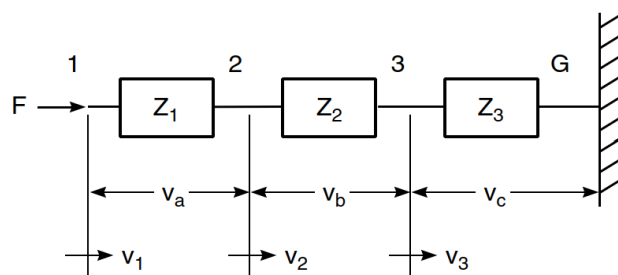
Source: adapted from Cyril (2002).

The impedance at point 1 is F/v_1 and the force is transmitted to all three elements.

The relative velocities are described below:

$$v_a = \frac{F}{Z_1}, \quad v_b = \frac{F}{Z_2}, \quad v_c = \frac{F}{Z_3}. \tag{95}$$

Thus, the total impedance is defined by

$$\frac{1}{Z} = \frac{F/Z_1 + F/Z_2 + F/Z_3}{F} = \frac{1}{Z_1} + \frac{1}{Z_2} + \frac{1}{Z_3} \ . \tag{96}$$

Extending this principle to any number of massless series elements,

$$\frac{1}{Z_s} = \sum_{i=1}^{n} \frac{1}{Z_i} \ , \tag{97}$$

where Z_s is the total mechanical impedance of the elements Z_i connected in series.

Since mobility is the reciprocal of impedance, the total mobility of elements connected in series is given by

$$Y_s = \sum_{i=1}^{n} Y_i \ . \tag{98}$$

The following theorems are the mechanical analogs of theorems widely used in analyzing electric circuits. They are statements of basic principles (or combinations of them) that apply to elements of mechanical systems. In all but Kirchhoff's laws, these theorems apply only to systems composed of linear, bilateral elements. A linear element is one in which the magnitudes of the basic elements (c, k, and m) are constant, regardless of the amplitude of motion of the system; a bilateral element is one in which forces are transmitted equally well in either direction through its connections.

The sum of all the forces acting at a point (common connection of several elements) is zero:

$$\sum_{i=1}^{n} F_i = 0 \ (\text{at a point}). \tag{99}$$

This follows directly from the considerations leading to Eq. (92).

The sum of the relative velocities across the mechanical elements in series and around a closed loop is zero:

$$\sum_{i=1}^{n} v_i = 0 \text{ (around a closed loop)}. \tag{100}$$

Kirchhoff's laws apply to any system, even when the elements are not linear or bilateral.

Based on all these concepts, a model formed by springs and damper is created to describe the insulation level of the mounts. It is worth to remember that the damper model of the rubber mount is associated to the loss modulus as explained in section 2.1.

The transmissibility function derived from all these concepts is expressed as

$$\left| H_m^j(w) \right| = \sqrt{\left[\frac{k_m^{j^2} K_m^{j^2} + k_m^{j^2} \eta_m^{j^2} + k_m^{j^2} K_m^{j^2}}{\left(k_m^{j^2} + K_m^{j^2} \right)^2 + k_m^{j^2} \eta_m^{j^2}} \right]^2 + \left[\frac{k_m^{j^2} K_m^{j^2} \eta_m^j}{\left(k_m^{j^2} + K_m^{j^2} \right)^2 + k_m^{j^2} \eta_m^{j^2}} \right]^2} \tag{101}$$

where m is the mount number, j is the direction x, y or z, k_m^j is the mount stiffness, K_m^j is the stiffness of the point where the mount is fixed and η_m^j is the loss factor of the mount.

4 METHODOLOGY

In this chapter, the optimization concepts used to solve the addressed problem are presented. A brief overview of constrained optimization theory is provided, as it forms the foundation of the algorithm used to tackle the problem.

The optimization algorithm employed is based on interior-point using the primal-dual logarithmic barrier method, which can accommodate both equality and inequality constraints. However, in the problem considered in this work, only inequality constraints will be applied.

4.1 OPTIMIZATION PROBLEM DEFINITION

To make the optimization process the constraint equations and objective function of Eq. (13) need to be defined, then this will be developed in this session.

The optimization of the vibrational isolation performance of the motor of this work is formed by four mounts. The three directions of each mount stiffness will be explored in this work, as there are four mounts then a total of twelve stiffness variables will compose the problem, furthermore, two mount positions will be variable whereas the other two mounts will be fixed. The three directions of the two mount positions which are subject to optimizations will be explored, so altogether eighteen variables will be subjected to the optimization process.

The Eq. (104) shows the twenty six constrained functions, where g_1 up to g_8 are related to the modal purity of the six DOF, the frequency mode distribution and the mount transmissibility. The constrained functions from g_9 up to g_{14} are related to the position of mounts 1 and 2. The constrained functions from g_{15} up to g_{26} are related to the stiffness of the mounts 1 to 4.

The objective function is built to meet the criterion of high modal purity, which is based on the high contribution of the vector component of each eigenvector.

The modal purity P_{kr}, as described by Chen et al. (2012), is given by the kinetic energy, which is associated with each mode shape, and is given by the kinetic energy of each mode as

$$P_{kr} = \frac{\sum_{j=1}^{6} M_{kj}\phi_{kr}\phi_{jr}}{\sum_{k=1}^{6}\sum_{j=1}^{6} M_{kj}\phi_{kr}\phi_{jr}} \times 100\% . \tag{102}$$

The term M_{kj} is the mass element of the matrix $[\mathbf{M}]$, ϕ_{kr} and ϕ_{jr} are the elements of the eigenvector matrix $[\mathbf{\Psi}]$ and then P_{kr} represents the kinetic energy of the r-th mode at the k-th DOF.

The eigenvector comes from the matrix $[\mathbf{M}]$ and the the global stiffness matrix $[\mathbf{K}]$, this matrix $[\mathbf{K}]$ has a mount position dependence, because $[\mathbf{K}] = \sum_{i=1}^{N}[\mathbf{B}_i]^T[\mathbf{k}_i]_G[\mathbf{B}_i]$ and as discussed previously $[\mathbf{B}_i]$ is formed by $[\mathbf{I}]$ and $[\mathbf{H}_i]$, where $[\mathbf{H}_i]$ is defined in Eq. (30) as a skew-matrix of the mount position i. For this reason the elements of the eigenvector matrix $[\mathbf{\Psi}]$ are affected by the mount position and as consequence the modal purity, which is dependent of the elements of the matrix $[\mathbf{\Psi}]$ are dependent on the mount position as well.

The objective function is given by the sum of the maximum value of each P_{kr} of each r-th mode:

$$f(\{\mathbf{X}\}) = -\sum_{k=1}^{6}\sum_{r=1}^{6}\max\left(P_{kr}\right). \tag{103}$$

In Eq. (103), the minus sign is used because the algorithm is designed to search for the minimum value of $f(\{\mathbf{X}\})$, thus, minimizing $f(\{\mathbf{X}\})$ is equivalent to maximizing the $-f(\{\mathbf{X}\})$. The minimum value $f(\{\mathbf{X}\})$ can achieve is -600% because the maximum value of P_{kr} for each mode is 100%.

Furthermore, the inequality constraints of the problem shown in Eq. (104) also need to be fulfilled.

$$g_r(\{\mathbf{X}\}) = p - \max(P_{kr}) \leq 0; \; k = r = 1, 2, \dots, 6$$
$$g_7(\{\mathbf{X}\}) = 7 \, Hz \, \leq \, f_r \, \leq 47 \, Hz$$
$$g_8 = \Omega_{r+1}(\{\mathbf{X}\}) - \Omega_r(\{\mathbf{X}\}) \geq 2$$
$$g_9 = T_m^j(w) = 20log\left[\left|H_m^j(w)\right|\right] < -30 \, dB$$
$$g_9 = -300 \leq X_1 \leq 50 \, mm$$
$$g_{10} = -250 \leq Y_1 \leq 50 \, mm$$
$$g_{11} = -150 \leq Z_1 \leq 50 \, mm$$
$$g_{12} = -300 \leq X_2 \leq 50 \, mm$$
$$g_{13} = \quad 50 \leq Y_2 \leq 250 \, mm$$
$$g_{14} = -150 \leq Z_2 \leq 50 \, mm$$
$$g_{15} = \quad 100 \leq S_{1x} \leq 600 \, N/mm$$

$$g_{16} = 100 \leq S_{1y} \leq 600 \, N/mm$$

$$g_{17} = 100 \leq S_{1z} \leq 600 \, N/mm$$

$$g_{18} = 100 \leq S_{2x} \leq 600 \, N/mm$$

$$g_{19} = 100 \leq S_{2y} \leq 600 \, N/mm \tag{104}$$

$$g_{20} = 100 \leq S_{2z} \leq 600 \, N/mm$$

$$g_{21} = 100 \leq S_{3x} \leq 600 \, N/mm$$

$$g_{22} = 100 \leq S_{3y} \leq 600 \, N/mm$$

$$g_{23} = 100 \leq S_{3z} \leq 600 \, N/mm$$

$$g_{24} = 100 \leq S_{4x} \leq 600 \, N/mm$$

$$g_{25} = 100 \leq S_{4y} \leq 600 \, N/mm$$

$$g_{26} = 100 \leq S_{4z} \leq 600 \, N/mm.$$

Here, p is the lower limit for the modal purity that is required in the project. In this work a modal purity p of 85% for each degree of freedom is chased as design criteria.

There are another two constraints related to the eigenvalues. These constraints are the functions $g_7(\{X\})$, which limits the frequency range of the rigid body modes between 7 Hz and 47 Hz, and the $g_8(\{X\})$ which requires that the separation of the frequencies of the modes must be greater or equal to 2 Hz. The frequency range and the frequency separation were extracted from benchmark studies of the vehicles on the market.

The constrained function $g_8(\{X\})$ ($T_m^j(w)$) is the module of the transmissibility function $\left| H_m^j(w) \right|$ converted to the dB scale. The isolation of 30 dB is used as the criteria o mount isolation, which corresponds to a reduction of about 32 times, here m represents the mount number and j represents the direction x, y or z.

Since the mathematical model of the rigid body mode is defined, it is possible to find the best modal purity by solving the optimization problem defined in Eq. (104).

The changes in the mount position can be highly sensible for modal purity and implies in strong modifications of this criteria. To have a controlled and predictable change on the project, optimization approaches can be used to overcome and predict downsides in changes like that.

Figure 23 shows the flowchart of the optimization process.

Figure 23: Flowchart of the optimization process.
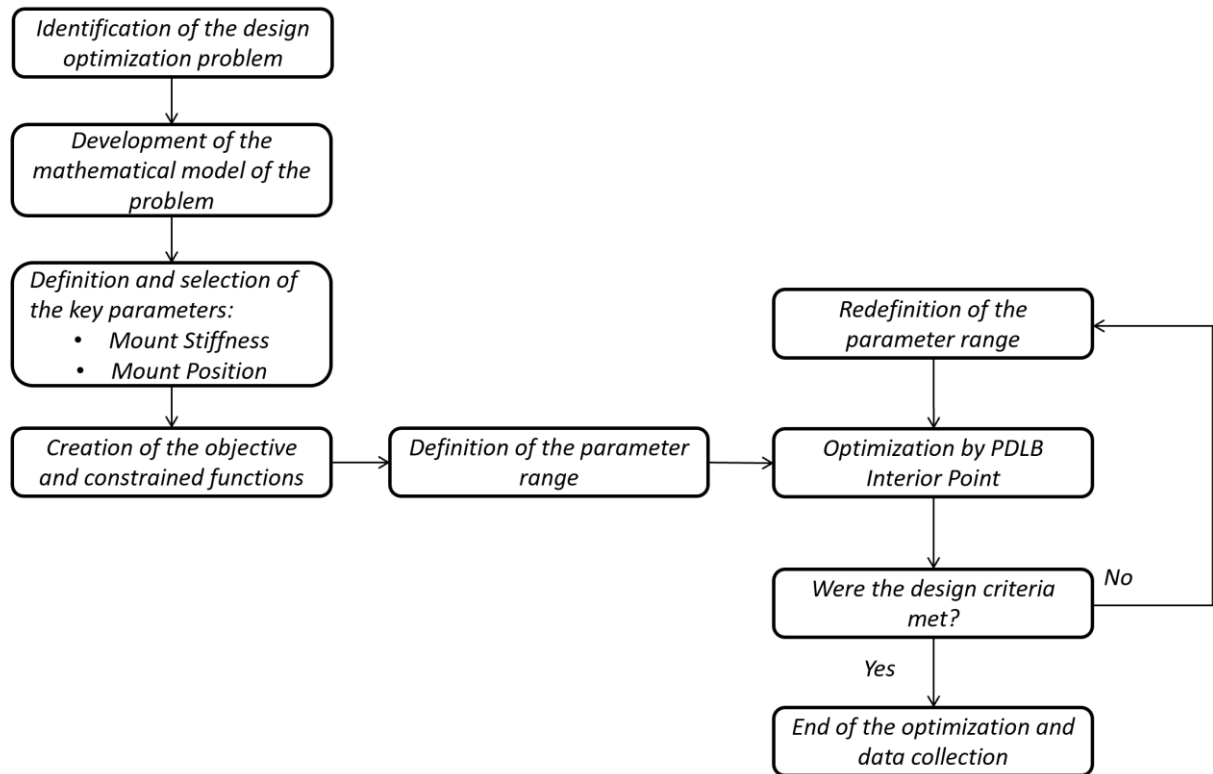
Once the achievement of the design criteria by Eq. (104) is completed, as a second step the isolation performance is also verified along the frequency range using the dynamic stiffness. This kind of analysis is carried out separately because the physics of the problem is related to the mechanical impedance between the mounts and their fixation points considering the frequency dependence.

Three different initial conditions (initial Condition 1, 2 and 3) changing the initial position of the mounts will be done with the objective to verify whether the algorithm can meet a local minimum more than once with different vector $\{X\}$. Whether this is the case the problem is pointing to different combination of the mount position meeting the constrained and the objective function criteria. The results of this analysis are carried out in chapter 5.

4.2 FMINCON PDLB INTERIOR-POINT ALGORITHM

The interior-point algorithm based on the PDLB strategy can be found on the Matlab software. As mentioned previously, this algorithm changes the initial problem

of Eq. (13) to Eq. (14) and uses the Newton's method during the process to get the vector $\Delta\{X\}$.

By default, the algorithm first attempts to get $\Delta\{X\}$ through the Newton's method, however when the approximate problem is not locally convex near the current iterate the algorithm uses the Conjugate Gradient (CG) method.

The conjugate gradient approach to solving the approximate problem Eq. (14) is similar to other conjugate gradient calculations. In this case, the algorithm adjusts both $\{X\}$ and $\{s\}$, keeping the slacks $\{s\}$ positive. The approach is to minimize a quadratic approximation to the approximate problem in a trust region, subject to linearized constraints.

In the CG method the Lagrange multipliers are obtained by approximately solving the KKT equations

$$\nabla_x L = \nabla f(\{X_k\}) + \sum_{i=1}^{m} u_{k,i}\,\nabla g_i(\{X_k\}) + \sum_{i=1}^{p} v_{k,i}\,\nabla h_i(\{X_k\}) = 0, \qquad (105)$$

in the least-squares sense, subject to $\{u\}$ being positive. Then it takes a step $(\Delta\{X\}, \Delta\{s\})$ to approximately solve

$$\begin{array}{c} min \\ \Delta\{X\}, \Delta\{s\} \end{array} \nabla f^T \Delta\{X\} + \frac{1}{2}\Delta\{X\}^T \nabla^2 L \Delta\{X\} + \mu\{e\}^T [S]^{-1}\Delta\{s\} + \frac{1}{2}\Delta\{s\}^T [S]^{-1}[\Lambda]\Delta\{s\}, \quad (106)$$

where $[\Lambda]$ is a diagonal matrix of size mxm formed by the vector of Lagrange multiplier $\{u\}$ and $\{e\}$ denotes the vector of ones having the same size as $\{u\}$ as well.

The solution of Eq (106) is subject to the linearized constraints

$$\{g(\{X\})\} + [J_g]\Delta\{X\} + \Delta\{s\} = 0, \qquad \{h(\{X\})\} + [J_h]\Delta\{X\} = 0. \qquad (107)$$

To solve Eq. (107) the algorithm tries to minimize a norm of the linearized constraints inside a region with radius scaled by R. Then Eq. (106) is solved with the constraints being to match the residual from solving Eq. (107), staying within the trust region of radius R, and keeping $\{s\}$ strictly positive. For details of the algorithm and the derivation, see Byrd, Gilbert and Nocedal (2000), Byrd, Hribar and Nocedal (1999), Waltz, Morales, Nocedal and Orban (2006).

4.3 Output of the Fmincon PDLB Interior-Point Algorithm

The main outputs of the optimization using the fmincon function will be taken into account in the results presented in Chapter 5. For this reason some definitions of those outputs are explained in this section.

The first output is the vector $\{X_k^*\}$ which represents the vector that minimizes the function.

The second output is the $f(\{X_k^*\})$ which represents the function minimized at the point $\{X_k^*\}$ where the minimum was identified.

The third output is the number of iterarions in the optimization process, each iteration is counted as a k number that indicates where the vector $\{X_k\}$ and its successive vectors $\{X_{k+1}\}$ are calculated.

The fourth output is the resultant vector $|\Delta\{X\}|$ which represents the length of the step where the next point $\{X_{k+1}\}$ will be evaluated.

$$\{X_{k+1}\} = \{X_k\} + \Delta\{X\}, \qquad k = 1,2,\dots n. \tag{108}$$

In the Chapter 5 the $|\Delta\{X\}|$ of the least step of the optimization process will be presented.

The fifth output is the number of calculated functions $Fcount$ that are counted during the optimization process. This count considers the number of objective function and constraint function evaluated nearby each $\{X_k\}$ vector, nevertheless, this count may or may not include the evaluation of all constraint functions. Figure 24.

Figure 24: Example of the count process during optimization.
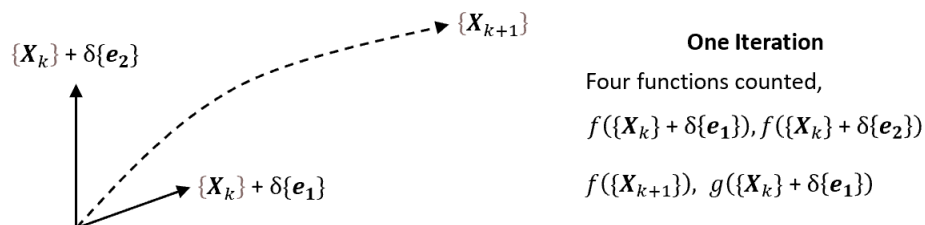
Source: the author.

The sixth output will be the Exitflag function which gives the status whether any violation during the algorithm process happened. The result of this output will be

explained individualy for Condition 1, 2 and 3 in Chapter 5 because it can vary from condition to condition.

From the six outputs only the vector $\{X_k^*\}$ will be presented in a table format to facilitate the visualization.

5 RESULTS AND DISCUSSION

5.1 CALIBRATION OF THE SIX DOF SYSTEM

It is of primary importance to calibrate the model, whether it be analytical or numerical, to be sure that the output of the result is reliable. For this reason, before performing the optimization, the analytical result of the six DOF system is compared to a reference result of the model used by a company specialized in the development of mount systems. The rigid body mode of the reference model was analyzed in the Altair software and a lumped mass representing the same physical properties of the actual motor is used, so the reference model considers the same assumptions used in this work. The refence model was already used for correlation with experimental data what makes its use even more reliable for calibration purposes of this work.

The purity of the modes of the reference model and the analytical model are presented in Table 1 and Table 2, respectively.

Table 1: Modal purity values of the six modes of the reference model.

Modal Purity (%)						
Mode	X	Y	Z	RX	RY	RZ
1	0	86	0	1	0	13
2	99	0	0	0	1	0
3	0	0	99	0	0	0
4	0	2	0	97	0	1
5	0	12	0	2	0	86
6	1	0	0	0	99	0

Source: the author.

Table 2: Modal purity values of the six modes of the analytical model presented here.

Modal Purity (%)						
Mode	X	Y	Z	RX	RY	RZ
1	0	87	0	0	0	13
2	99	0	0	0	0	0
3	0	0	99	0	0	0
4	0	0	0	99	0	0
5	0	13	0	0	0	87
6	0	0	0	0	99	0

Source: the author.

Table 3 shows the difference in the modal purity between the reference model and the analytical model.

Table 3: Difference of the modal purity between the reference model and analytical model.

Modal purity difference (%)						
Mode	**X**	**Y**	**Z**	**RX**	**RY**	**RZ**
1	0.00	1.00	0.00	1.00	0.00	0.00
2	0.00	0.00	0.00	0.00	1.00	0.00
3	0.00	0.00	0.00	0.00	0.00	0.00
4	0.00	2.00	0.00	2.00	0.00	1.00
5	0.00	1.00	0.00	2.00	0.00	1.00
6	1.00	0.00	0.00	0.00	0.00	0.00

Source: the author.

The modal frequencies of the reference model and the analytical model are presented as well in Table 5.

Table 4: Modal frequencies of the reference and the analytical model and the difference frequency for each mode.

Mode	**Reference Model (Hz)**	**Analytical Model (Hz)**	**Frequency Difference (Hz)**
1	13.4	13.4	0.0
2	16.8	16.8	0.0
3	21.7	21.7	0.0
4	24.0	24.1	0.1
5	32.2	32.0	0.2
6	45.2	45.2	0.0

Source: the author.

As it can be observed by the data, the analytical model presents a very high accuracy when compared to the reference results. The modal purity and the modal frequencies of both models are, in general, very close to each other.

5.2 RESULTS OF DIFFERENT OPTIMIZATIONS OF THE MOTOR MOUNT PROJECT

The constraints of the optimization of the mount project are defined in Eq. (104). The upper and lower limits of the position and stiffness are shown in Table 5 to facilitate the visualization of constraints.

In this work, two mounts (mount 3 and mount 4) are kept unchanged while the other two (mount 1 and mount 2) will have some room to get the best position for the mount project.

The variables of mount positions and stiffness are used directly on the algorithm for the optimization process, whereas the angle and damping are fixed parameters pre-defined in the project, however, they can be changed manually if there is the need to make any different assumptions regarding the initial specifications of the project.

Table 5 shows the upper and lower limits of the position and stiffnesses of each mount. The mount position is described as shown in Figure 16.

Table 5: Lower and upper limits of variables of position and stiffness of mounts 1 to 4.

Limits of optimization of the variables									
		Mount 1		Mount 2		Mount 3			
Variable	Coordinate	Lower Limit	Upper Limit	Lower Limit	Upper Limit	Lower Limit	Upper Limit	Lower Limit	Upper Limit
Position (mm)	X	-300	50	-300	50	319		319	
	Y	-250	50	50	250	-220		220	
	Z	-150	50	-150	50	11		11	
Stiffness (N/mm)	X	100	600	100	600	100	600	100	600
	Y	100	600	100	600	100	600	100	600
	Z	100	600	100	600	100	600	100	600

Source: the author.

Table 6 shows the values of the damping loss factor, considered fixed, and angle of each mount regarding a fixed coordinate system at the CG of the motor.

Table 6: Fixed parameters of damping and angles of mounts 1 to 4.

Fixed Parameter of Angle and Loss Factor used in each Mount					
Variable	Coordinate	Mount 1	Mount 2	Mount 3	Mount 4
Loss Factor	X	0.04	0.04	0.04	0.04
	Y	0.04	0.04	0.04	0.04
	Z	0.04	0.04	0.04	0.04
Angle Around (rad)	X	0	0	0	0
	Y	0	0	0	0
	Z	0	0	$\pi/2$	$-\pi/2$

Source: the author.

The mounts 3 and 4 are rotated around the Z axis of the Vehicle Coordinate System (VCS) by $\pi/2$ and $-\pi/2$, respectively. Figure 25 shows this rotation.

Figure 25: Rotation of the mounts 3 and 4 around the Z axis.
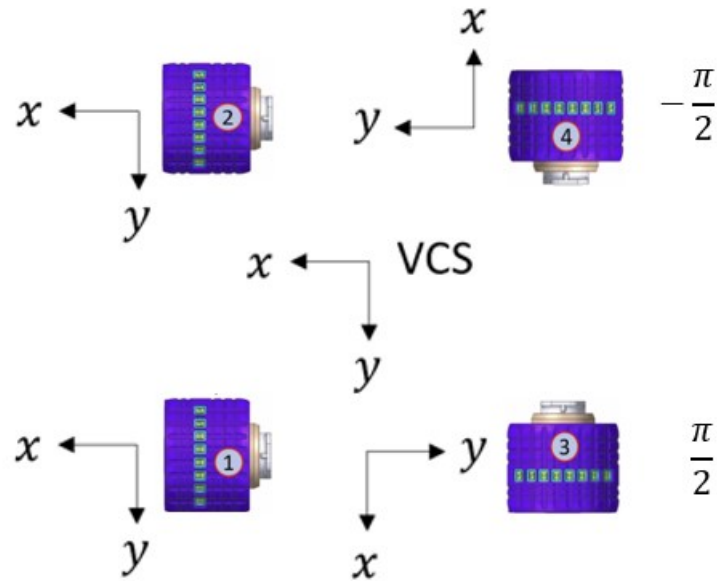
Source: the author.

The initial condition is the point where the algorithm starts to search for the minimum of the objective function. The initial Condition 1 with the position and stiffness are defined in Table 7.

Table 7: Values of position and stiffness used for the initial Condition 1.

Initial Condition 1					
Variable	Coordinate	Mount 1	Mount 2	Mount 3	Mount 4
Position (mm)	X	-100	-100	NA	NA
	Y	-100	100	NA	NA
	Z	-100	-100	NA	NA
Stiffness (N/mm)	X	400	400	400	400
	Y	200	200	200	200
	Z	500	500	500	500

Source: the author.

Tables 8, 9 and 10 show the results of the optimization for Condition 1 versus a reference project. The reference project is based on the results of an actual development of a motor mount project and is not the same one used in the calibration, which was called the reference model. It is important to mention that the calibration model in section 5.1 uses the results of a project already on the market whereas the project reference used here in section 5.2 uses the results of a project that was adapted from a former vehicle platform and is not achieving the criterion of Eq. (99).

Table 8: Results of natural frequencies and the modal purity of optimization for condition 1 and the reference project.

Frequency Condition 1	(Hz)		Modal purity (%) - Condition 1					
		DOF	X	Y	Z	Rx	Ry	Rz
f_1	10.94	f_1	0	97	2	0	0	0
f_2	13.37	f_2	85	0	0	1	14	0
f_3	16.24	f_3	0	2	92	0	0	6
f_4	18.39	f_4	1	0	0	99	0	0
f_5	22.73	f_5	0	1	5	0	0	94
f_6	31.01	f_6	14	0	0	0	86	0
Frequency Reference	(Hz)		Modal purity (%) – Reference					
		DOF	X	Y	Z	Rx	Ry	Rz
f_1	15.10	f_1	0	69	5	24	0	1
f_2	17.32	f_2	97	0	2	0	0	0
f_3	19.65	f_3	0	29	25	43	0	2
f_4	25.56	f_4	2	1	55	16	15	11
f_5	29.04	f_5	0	0	2	11	2	84
f_6	75.92	f_6	0	0	11	6	82	0

Source: the author.

Table 9: Results of position and stiffness ($\{X_k^*\}$) of mounts 1 to 4 for Condition 1 and the reference project.

Optimization Results Condition 1					
Variable	Coordinate	Mount 1	Mount 2	Mount 3	Mount 4
Position (mm)	X	-140	-181	319	319
	Y	-204	188	-220	220
	Z	-73	-66	11	11
Stiffness (N/mm)	X	400.21	401.75	393.97	393.98
	Y	185.04	184.69	204.00	205.44
	Z	485.97	497.67	496.90	503.22
Optimization Results Reference					
Variable	Coordinate	Mount 1	Mount 2	Mount 3	Mount 4
Position (mm)	X	-295	-295	319	319
	Y	-141	141	-220	220
	Z	-130	-130	11	11
Stiffness (N/mm)	X	510	510	510	510
	Y	460	460	460	460
	X	585	585	585	585

Source: the author.

Table 10: Results of transmissibility of mounts 1 to 4 for Condition 1 and the reference project.

Transmissibility Condition 1				
Coordinate	Mount 1 (dB)	Mount 2 (dB)	Mount 3 (dB)	Mount 4 (dB)
x	-31.70	-31.67	-31.83	-31.83
y	-34.81	-34.82	-33.98	-33.92
z	-30.06	-29.86	-29.87	-29.77
Transmissibility Reference				
Coordinate	Mount 1 (dB)	Mount 2 (dB)	Mount 3 (dB)	Mount 4 (dB)
x	-29.65	-29.65	-29.65	-29.65
y	-27.12	-27.12	-27.12	-27.12
z	-28.50	-28.50	-28.50	-28.50

Source: the author.

The magnitude and the phase of the receptance of each individual translational and rotational modes from Condition 1 are presented in Figures 26 and 27.

Figure 26: Magnitude and phase from receptance of the translational modes x, y and z for Condition 1.
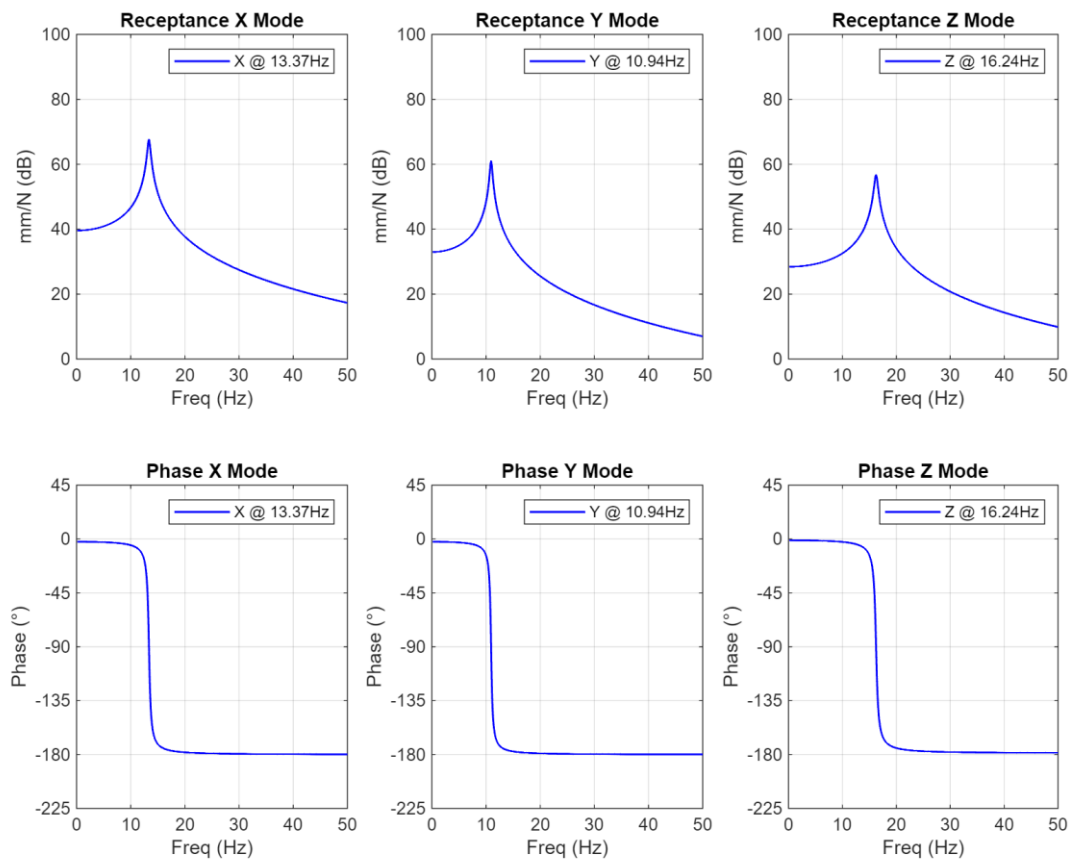
Source: the author

Figure 27: Magnitude and phase from receptance of the rotational modes rx, ry and rz for Condition 1.
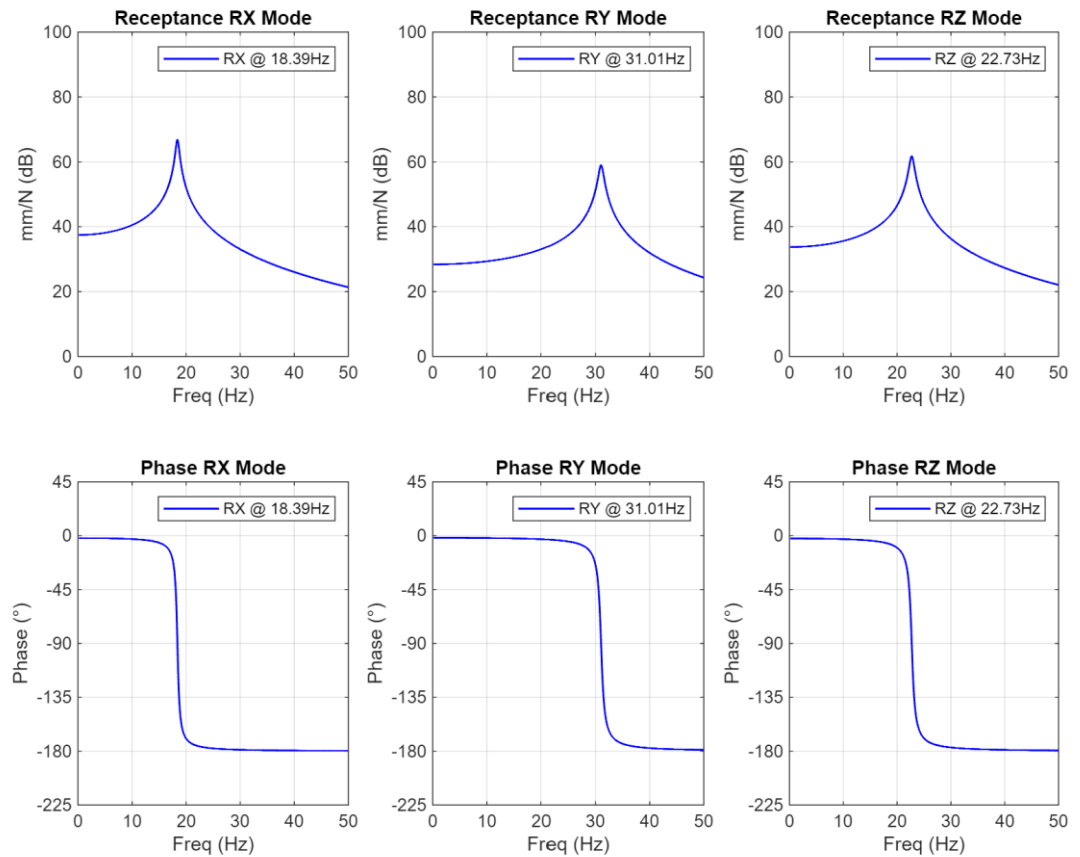
Source: the author.

The combination of all modes found for Condition 1 are represented by the receptance through the sum of the driving points in Figure 28.

The objective function value for the reference project is -431% and the optimization results are below except by the vector $\{X_k^*\}$ which was already presented in Table 9.

- $f(\{X_k^*\}) = -548\%$

- Number of iterations $k = 4$

- Last length step $|\Delta\{X\}| = 2.6515 \times 10^{-10}$

- Number of evaluated function $Fcount = 116$

- Exitflag = 2 (This means that $|\Delta\{X\}|$ is less than the accuracy of the algorithm and the maximum resolution was achieved. Similarly the minimum identified is within the constraint region considering the accuracy of the algorithm).

Figure 28: Drive point receptance of the six DOF for Condition 1.
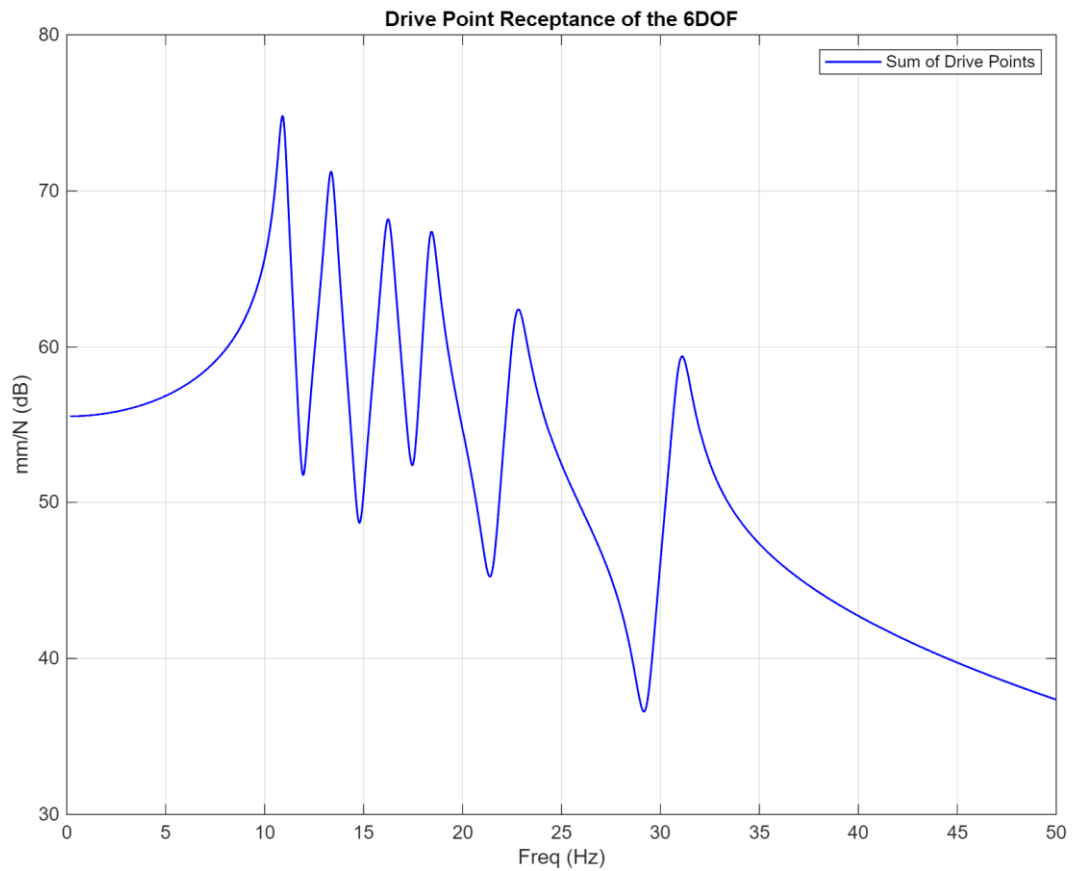
Source: the author.

With an initial Condition 2 the model is rerun, the values of the initial Condition 2 are presented in Table 2.

Table 11: Values of position and stiffness used on the initial Condition 2.

Initial Condition 2					
Variable	Coordinate	Mount 1	Mount 2	Mount 3	Mount 4
Position (mm)	X	-250	-250	NA	NA
	Y	-150	150	NA	NA
	Z	-50	-50	NA	NA
Stiffness (N/mm)	X	400	400	400	400
	Y	200	200	200	200
	Z	500	500	500	500

Source: the author.

Tables 12, 13 and 14 show the results of the optimization for Condition 2 versus the reference project.

Table 12: Results of natural frequencies and the modal purity of optimization for Condition 2 and the reference project.

Frequency Condition 2	(Hz)		Modal purity (%) – Condition 2					
		DOF	X	Y	Z	Rx	Ry	Rz
f_1	11.75	f_1	0	87	0	1	0	11
f_2	13.49	f_2	99	1	0	0	0	0
f_3	15.90	f_3	0	1	9	89	0	0
f_4	17.38	f_4	0	0	90	10	1	0
f_5	22.26	f_5	0	11	0	0	0	89
f_6	33.90	f_6	0	0	1	0	99	0
Frequency Reference	(Hz)		Modal purity (%) – Reference					
		DOF	X	Y	Z	Rx	Ry	Rz
f_1	15.10	f_1	0	69	5	24	0	1
f_2	17.32	f_2	97	0	2	0	0	0
f_3	19.65	f_3	0	29	25	43	0	2
f_4	25.56	f_4	2	1	55	16	15	11
f_5	29.04	f_5	0	0	2	11	2	84
f_6	75.92	f_6	0	0	11	6	82	0

Source: the author.

Table 13 : Results of position and stiffness of mounts 1 to 4 for Condition 2 and the reference project.

Optimization Results Condition 2					
Variable	Coordinate	Mount 1	Mount 2	Mount 3	Mount 4
Position (mm)	X	-246	-246	319	319
	Y	-117	153	-220	220
	Z	-46	-43	11	11
Stiffness (N/mm)	X	400.60	400.74	396.18	396.18
	Y	193.26	193.26	202.21	202.46
	Z	-246	-246	319	319
Optimization Results Reference					
Variable	Coordinate	Mount 1	Mount 2	Mount 3	Mount 4
Position (mm)	X	-295	-295	319	319
	Y	-141	141	-220	220
	Z	-130	-130	11	11
Stiffness (N/mm)	X	510	510	510	510
	Y	460	460	460	460
	X	585	585	585	585

Source: the author.

Table 14: Results of transmissibility of mounts 1 to 4 for Condition 2 and the reference project.

| Coordinate	Transmissibility Condition 2			
	Mount 1 (dB)	Mount 2 (dB)	Mount 3 (dB)	Mount 4 (dB)
x	-31.69	-31.69	-31.78	-31.78
y	-34.44	-34.44	-34.05	-34.04
z	-29.80	-29.80	-29.85	-29.84
Coordinate	Transmissibility Reference			
	Mount 1 (dB)	Mount 2 (dB)	Mount 3 (dB)	Mount 4 (dB)
x	-29.65	-29.65	-29.65	-29.65
y	-27.12	-27.12	-27.12	-27.12
z	-28.50	-28.50	-28.50	-28.50

Source: the author.

The magnitude and the phase from receptance of each individual translational and rotational modes from Condition 1 are presented in Figures 29 and 30.

Figure 29: Magnitude and phase from receptance of the translational modes x, y and z for Condition 2.
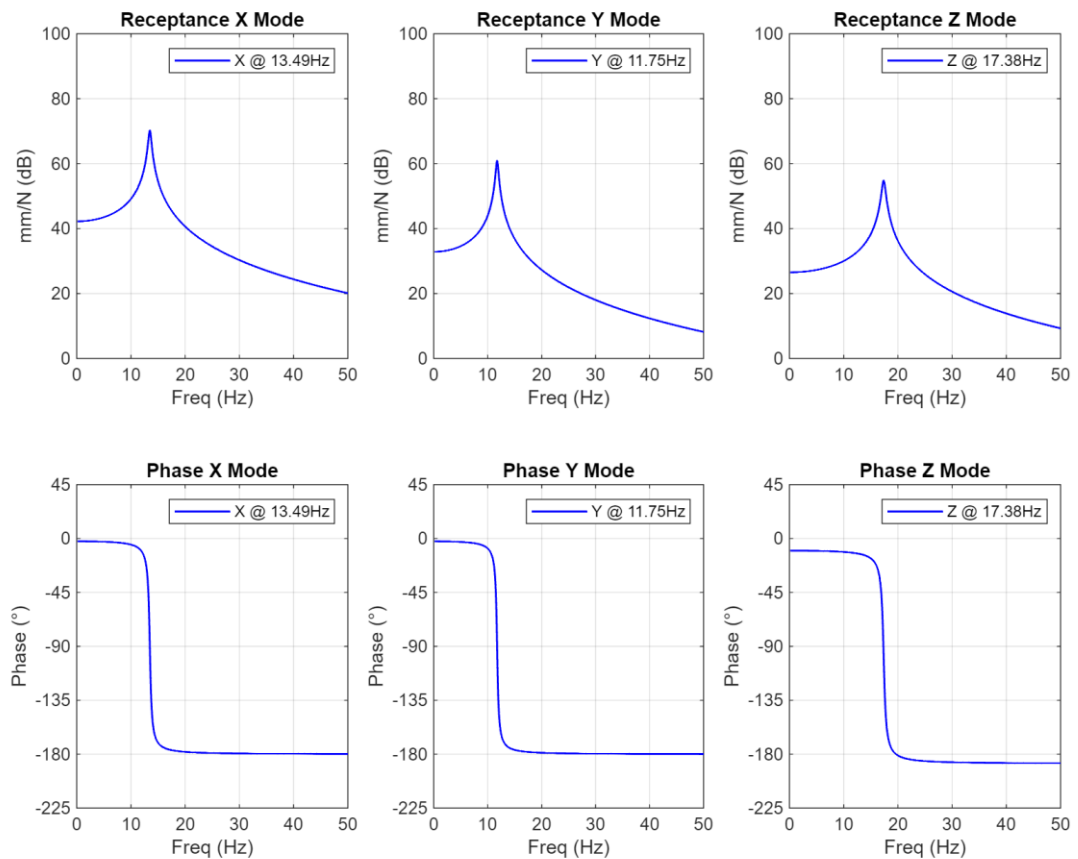
Source: the author.

Figure 30: Magnitude and phase from receptance of the rotational modes rx, ry and rz for Condition 2.
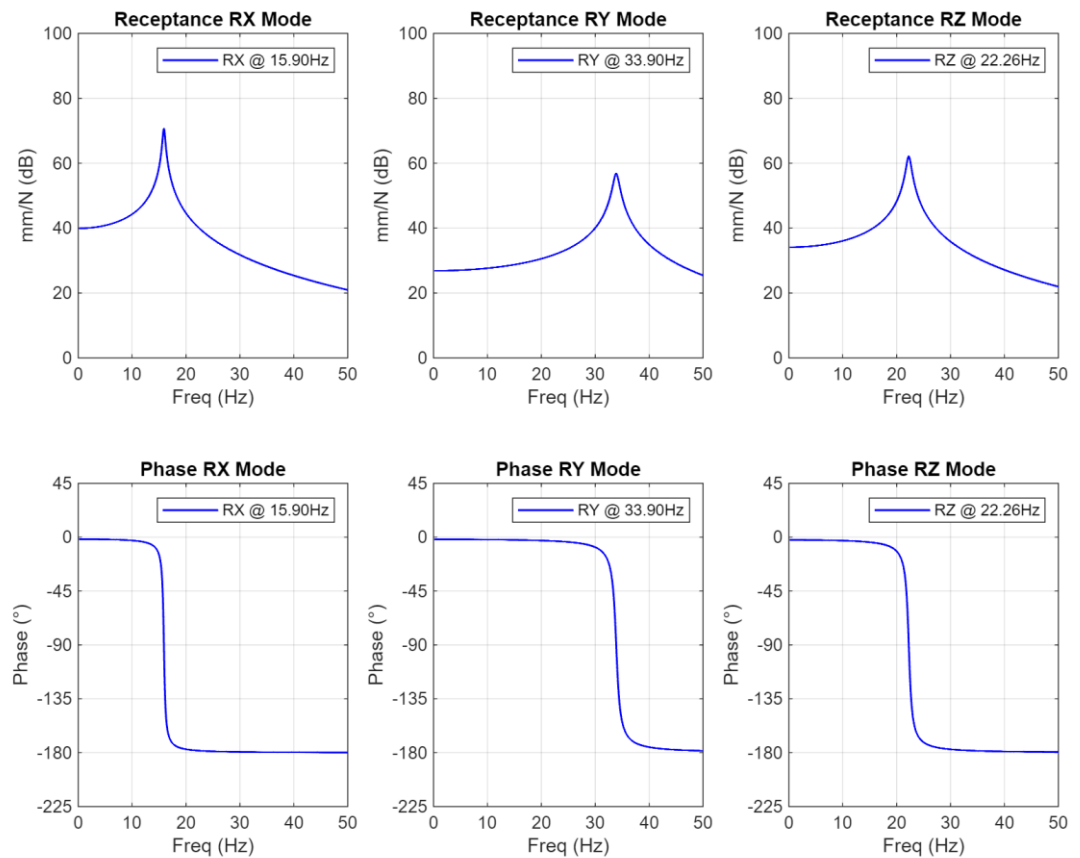
Source: the author.

The combination of all modes found for Condition 2 are represented by the receptance through the sum of the driving points in Figure 31.

The objective function value for the reference project is -431% and the optimization results of Condition 2 are below except by the vector $\{X_k^*\}$ which was already presented in Table 13.

- $f(\{X_k^*\}) = -554\%$
- Number of iterations $k = 2$
- Last lenght step $|\Delta\{X\}| = 2.6121 \times 10^{-10}$
- Number of evaluated function $Fcount = 75$
- Exitflag = -2 (This means that no feasible point was found)

Although the optimization of the objective function have presented a good result, the algorithm was not able to meet the constraint function g_8 which requires a separation of 2 Hz between the modes.

Figure 31: Drive point receptance of the six DOF for Condition 2.
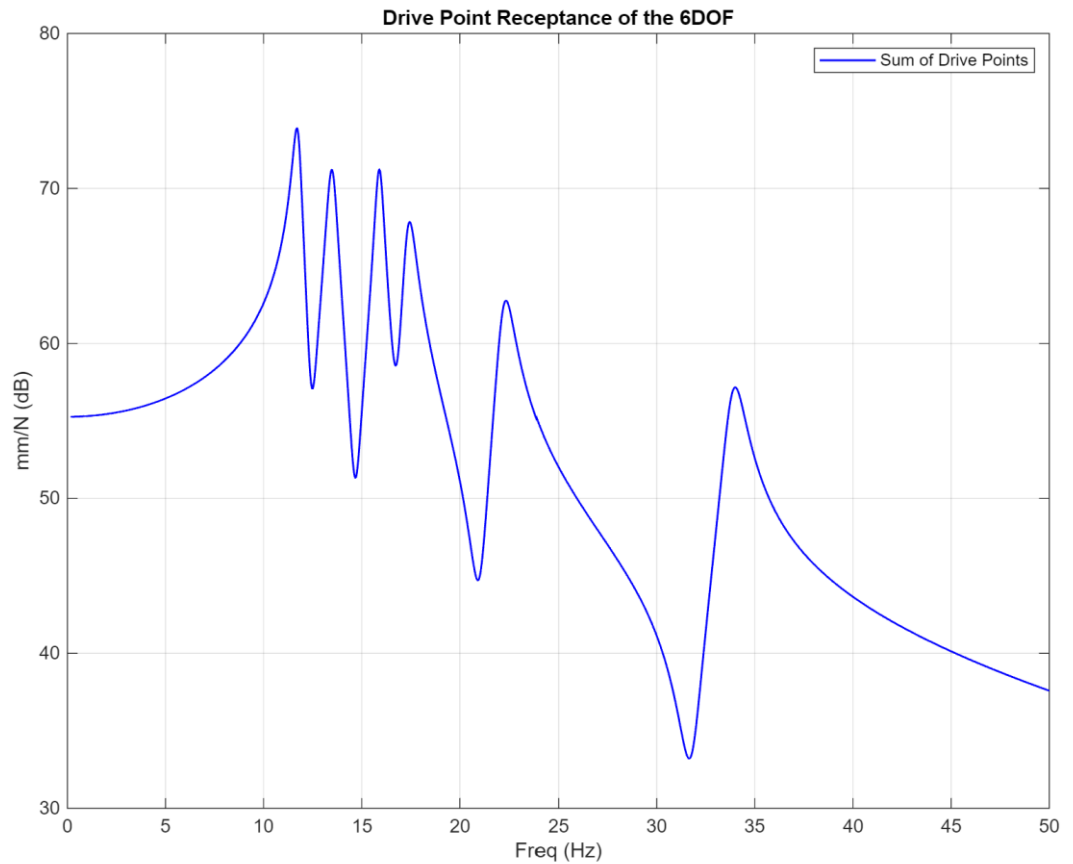
Source: the author.

Once again, the initial condition is changed. This time, the optimization problem is solved using initial Condition 3. The values for initial Condition 3 are shown in Table 15.

Table 15: Values of position and stiffness used on the initial Condition 3.

Initial Condition 3					
Variable	Coordinate	Mount 1	Mount 2	Mount 3	Mount 4
Position (mm)	X	50	50	319	319
	Y	50	50	-220	220
	Z	50	50	11	11
Stiffness (N/mm)	X	400	400	400	400
	Y	200	200	200	200
	Z	500	500	500	500

Source: the author.

Tables 16, 17 and 18 show the results of the optimization for Condition 3 versus the reference project.

Table 16: Results of natural frequencies and the modal purity of optimization for Condition 3 and the reference project.

Frequency Condition 3	(Hz)	Modal purity (%) - Condition 3						
		DOF	X	Y	Z	Rx	Ry	Rz
f_1	11.49	f_1	0	91	0	0	0	9
f_2	13.74	f_2	100	0	0	0	0	0
f_3	16.51	f_3	0	0	97	0	3	0
f_4	19.10	f_4	0	0	0	100	0	0
f_5	23.26	f_5	0	9	0	0	0	91
f_6	31.11	f_6	0	0	3	0	97	0
Frequency Reference	(Hz)	Modal purity (%) – Reference						
		DOF	X	Y	Z	Rx	Ry	Rz
f_1	15.10	f_1	0	69	5	24	0	1
f_2	17.32	f_2	97	0	2	0	0	0
f_3	19.65	f_3	0	29	25	43	0	2
f_4	25.56	f_4	2	1	55	16	15	11
f_5	29.04	f_5	0	0	2	11	2	84
f_6	75.92	f_6	0	0	11	6	82	0

Source: the author.

Table 17: Results of position and stiffness of mounts 1 to 4 for Condition 3 and the reference project.

Optimization Results Condition 3					
Variable	Coordinate	Mount 1	Mount 2	Mount 3	Mount 4
Position (mm)	X	-200	-193	319	319
	Y	-223	224	-220	-220
	Z	-35	-15	11	11
Stiffness (N/mm)	X	416740	416530	377570	377560
	Y	184810	184250	205990	207900
	Z	484510	486080	480860	481090
Optimization Results Reference					
Variable	Coordinate	Mount 1	Mount 2	Mount 3	Mount 4
Position (mm)	X	-295	-295	319	319
	Y	-141	141	-220	220
	Z	-130	-130	11	11
Stiffness (N/mm)	X	510	510	510	510
	Y	460	460	460	460
	X	585	585	585	585

Source: the author.

Table 18: Results of transmissibility of mounts 1 to 4 for Condition 3 and the reference project.

Transmissibility Condition 3				
Coordinate	Mount 1 (dB)	Mount 2 (dB)	Mount 3 (dB)	Mount 4 (dB)
x	-31.70	-31.67	-31.83	-31.83
y	-34.81	-34.82	-33.98	-33.92
z	-30.06	-29.86	-29.87	-29.77
Transmissibility Reference				
Coordinate	Mount 1 (dB)	Mount 2 (dB)	Mount 3 (dB)	Mount 4 (dB)
x	-29.65	-29.65	-29.65	-29.65
y	-27.12	-27.12	-27.12	-27.12
z	-28.50	-28.50	-28.50	-28.50

Source: the author.

The magnitude and the phase of the receptance of each individual translational and rotational modes from Condition 3 are presented in Figures 32 and 33.

Figure 32: Magnitude and phase from receptance of the translational modes x, y and z for Condition 3.
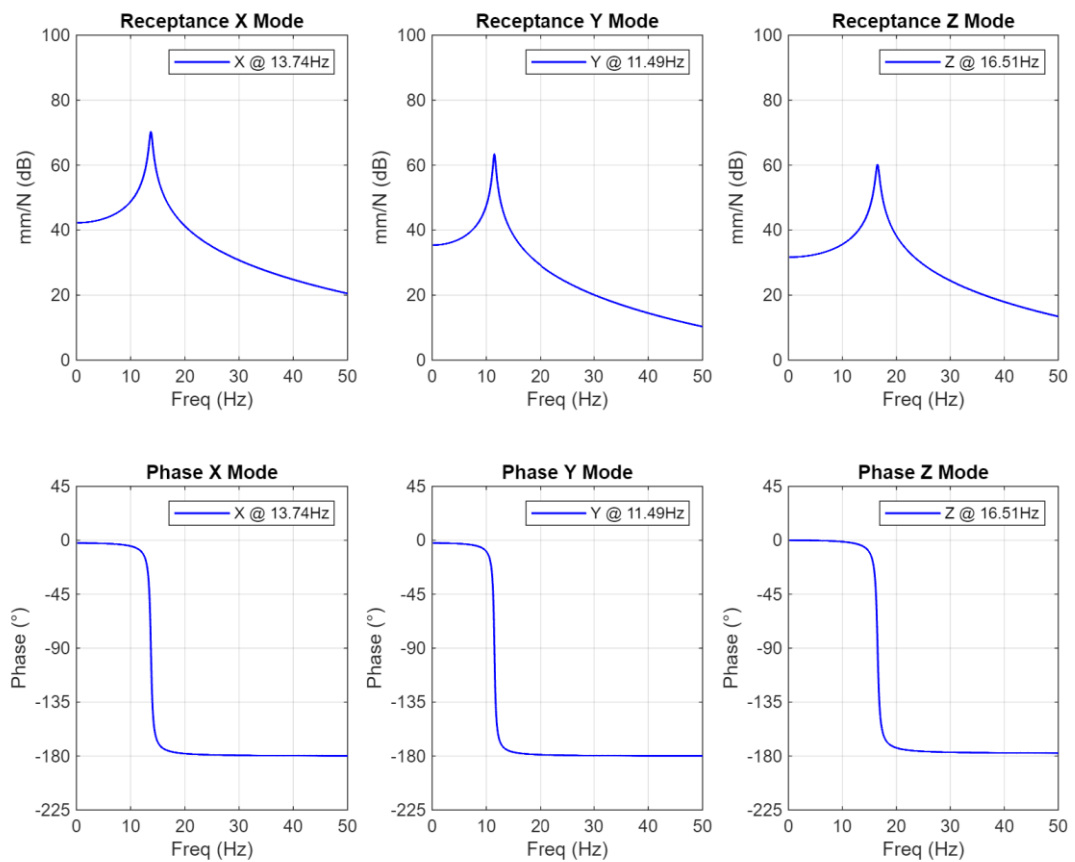
Source: the author.

Figure 33: Magnitude and phase from receptance of the rotational modes rx, ry and rz for Condition 3.
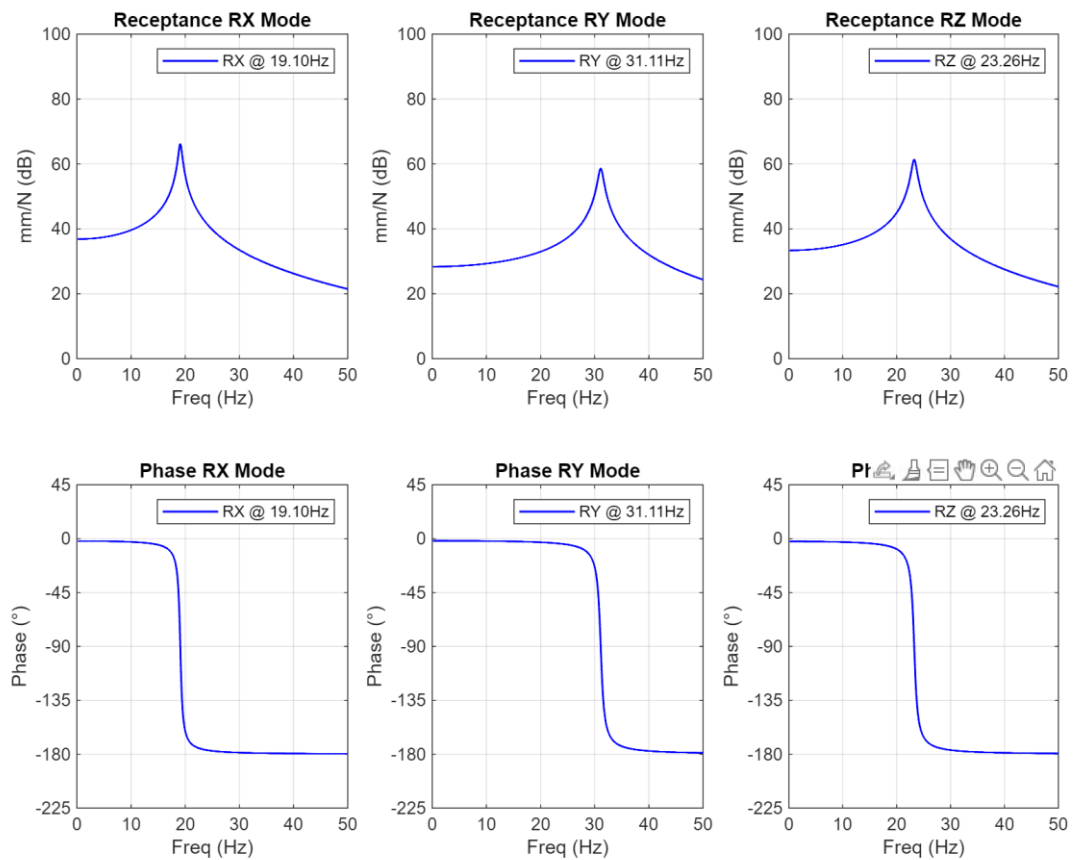

Source: the author.

The combination of all modes found on Condition 3 are represented by the receptance through the sum of the driving points in Figure 34.

The objective function value for the reference project is -431% and the optimization results are below except by the vector $\{X_k^*\}$ which was already presented in Table 17.

- $f(\{X_k^*\}) = -575\%$
- Number of iterations $k = 20$
- Last length step $|\Delta\{X\}| = 2.9812\text{x}10^{-10}$
- Number of evaluated function $Fcount = 465$
- Exitflag = 2 (This means that $|\Delta\{X\}|$ is less than the accuracy of the algorithm and the maximum resolution was achieved. Similarly, the minimum identified is within the constraint region considering the accuracy of the algorithm).

Figure 34: Drive point receptance of the DOF on Condition 3.
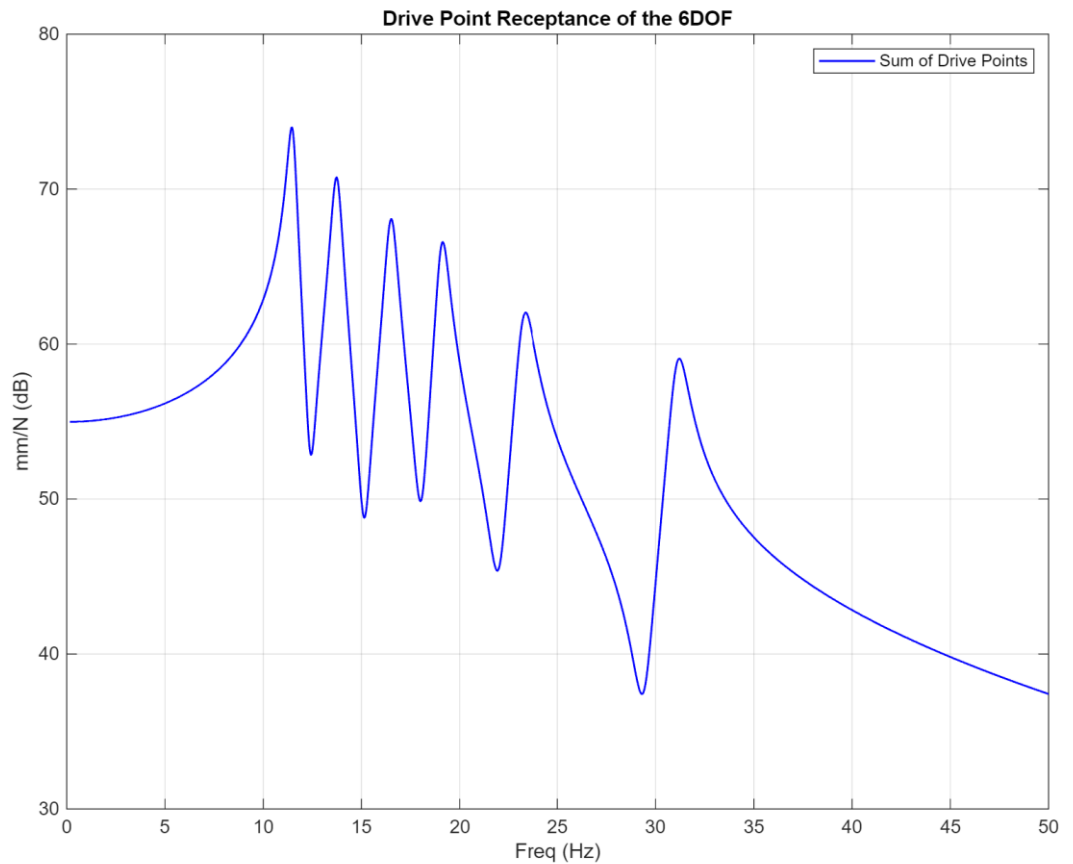
Source: the author.

5.3 COMPARISON OF RESULTS OF DIFFERENT OPTIMIZATIONS

Table 19 shows the comparison of the six natural frequencies obtained from the optimization results for conditions 1, 2 and 3. The frequency criterion of the constraint functions were defined to be greater than 7 Hz and smaller than 47 Hz.

Table 19: Comparison of the natural frequencies of the conditions 1, 2 and 3.

Frequency Mode	Condition 1 (Hz)	Condition 2 (Hz)	Condition 3 (Hz)
f_1	10.94	11.75	11.49
f_2	13.37	13.49	13.74
f_3	16.24	15.90	16.51
f_4	18.39	17.38	19.10
f_5	22.73	22.26	23.26
f_6	31.01	33.90	31.11

Source: the author.

Table 20 shows the comparison of the modal purity per DOF for the conditions 1, 2 and 3. The resctriction functions of modal purity required a modal purity greater than 85%.

Table 20: Comparison of the modal purity of each DOF for conditions 1, 2 and 3.

	Modal Purity X (%)			Modal Purity Y (%)		
DOF	Condition 1	Condition 2	Condition 3	Condition 1	Condition 2	Condition 3
f1	0	0	0	97	87	91
f2	85	99	100	0	1	0
f3	0	0	0	2	1	0
f4	1	0	0	0	0	0
f5	0	0	0	1	11	9
f6	14	0	0	0	0	0
	Modal Purity Z (%)			Modal Purity RX (%)		
DOF	Condition 1	Condition 2	Condition 3	Condition 1	Condition 2	Condition 3
f1	2	0	0	0	1	0
f2	0	0	0	1	0	0
f3	92	9	97	0	89	0
f4	0	90	0	99	10	100
f5	5	0	0	0	0	0
f6	0	1	3	0	0	0
	Modal Purity RY (%)			Modal Purity RZ (%)		
DOF	Condition 1	Condition 2	Condition 3	Condition 1	Condition 2	Condition 3
f1	0	0	9	0	11	0
f2	14	0	0	0	0	0
f3	0	0	0	6	0	3
f4	0	1	0	0	0	0
f5	0	0	91	94	89	0
f6	86	99	0	0	0	97

Source: the author.

Table 21 shows the comparison of the transmissibility of mounts 1, 2, 3 and 4 in each direction for the conditions 1, 2 and 3. The resctrion functios of transmissibility required a transmissibility smaller than -30dB.

Table 21: Comparison of the transmissibility of mounts 1, 2 , 3 and 4 for the conditions 1, 2 and 3.

	Transmissibility Mount 1			Transmissibility Mount 2		
Coordinate	Condition 1	Condition 2	Condition 3	Condition 1	Condition 2	Condition 3
X	-31.70	-31.69	-31.36	-31.67	-31.69	-31.36
Y	-34.81	-34.44	-34.82	-34.82	-34.44	-34.84
Z	-30.06	-29.80	-30.09	-29.86	-29.80	-30.06
	Transmissibility Mount 3			Transmissibility Mount 4		
Coordinate	Condition 1	Condition 2	Condition 3	Condition 1	Condition 2	Condition 3
X	-31.83	-31.78	-32.19	-31.83	-31.78	-32.19
Y	-33.98	-34.05	-33.89	-33.92	-34.04	-33.81
Z	-29.87	-29.85	-30.15	-29.77	-29.84	-30.14

Source: the author.

Table 22 shows the comparison of the position and stiffness of mounts 1, 2, 3 and 4 for conditions 1, 2 and 3. The table shows how the positions and stiffness change.

Table 22: Comparison of the position and stiffness of mounts 1, 2 , 3 and 4 for the Conditions 1, 2 and 3.

Position and Mount Stiffness Optimization Mount 1				
Variable	Coordinate	Condition 1	Condition 2	Condition 3
Position (mm)	X	-140	-246	-200
	Y	-204	-117	-223
	Z	-73	-46	-35
Stiffness (N/mm)	X	400.21	400.60	416.74
	Y	185.04	193.26	184.81
	Z	485.97	501.11	484.51
Position and Mount Stiffness Optimization Mount 2				
Variable	Coordinate	Condition 1	Condition 2	Condition 3
Position (mm)	X	-181	-246	-193
	Y	188	153	224
	Z	-66	-43	-15
Stiffness (N/mm)	X	401.75	400.74	416.53
	Y	184.69	193.26	184.25
	Z	497.67	501.44	486.08
Position and Mount Stiffness Optimization Mount 3				
Variable	Coordinate	Condition 1	Condition 2	Condition 3
Position (mm)	X	319	319	319
	Y	-220	-220	-220
	Z	11	11	11
Stiffness (N/mm)	X	393.97	396.18	377.57
	Y	204.00	202.21	205.99
	Z	496.90	498.42	480.86

Position and Mount Stiffness Optimization Mount 4				
Variable	Coordinate	Condition 1	Condition 2	Condition 3
Position (mm)	X	319	319	319
	Y	220	220	220
	Z	11	11	11
Stiffness (N/mm)	X	393.98	396.18	377.56
	Y	205.44	202.46	207.90
	Z	503.22	498.87	481.09

Source: the author.

The Figure 35, 36 and 37 shows the mount position vectors of Conditions 1, 2 and 3, respectively, by the colors red, green and blue. The two black vectors represent the fixed mounts.

Figure 35: Mount position view from XY plane for Conditions 1, 2 and 3.
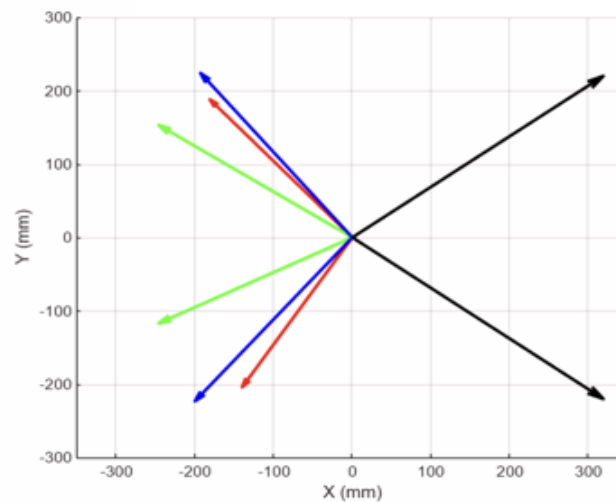
Source: the author.

Figure 36: Mount position view from XZ plane for Conditions 1, 2 and 3.
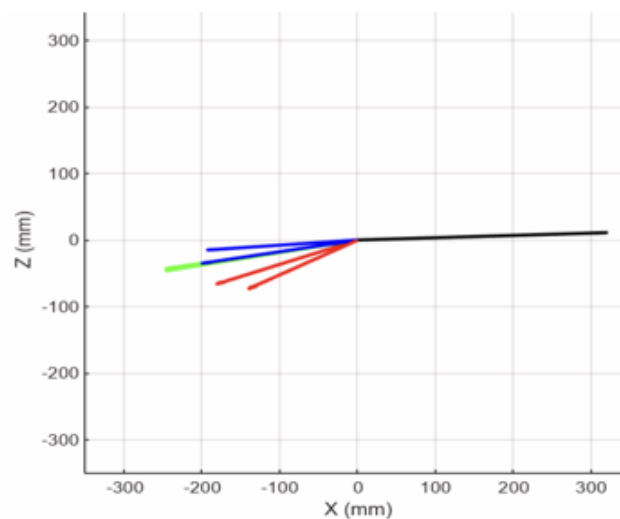
Source: the author.

Figure 37: Mount position view from YZ plane for Conditions 1, 2 and 3.
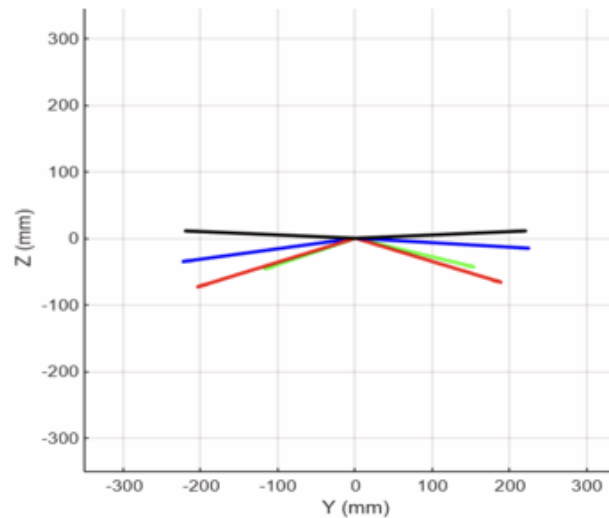
Source: the author.

Table (23) shows the magnitude of the positions of the mounts 1 and 2, which were under the optimization process.

Table 23: Comparison of the magnitude of each position of mounts 1 and 2 for Conditions 1, 2 and 3.

Vector Sum Optimization Mount 1			
Variable	Condition 1	Condition 2	Condition 3
Lenght (mm)	258	277	302
Vector Sum Optimization Mount 2			
Variable	Condition 1	Condition 2	Condition 3
Lenght (mm)	269	293	296

Source: the author.

Table 23 indicates how the magnitude of length of the bracket mount can be explored during the optimization process. This can be used, for example, to optimize local resonance frequencies of the bracket that might be causing problems on transmissibility.

5.4 MOUNT TRANSMISSIBILITY BASED ON DYNAMIC STIFFNESS MEASUREMENT

It is essential to assess the transmissibility performance of the mount as a function of the frequency as the mount stiffness also varies with the frequency.

For this assessment, a mount with a static stiffness of 600 N/mm was used, as it is comparable to the static stiffness of optimized mounts. The selected mount was identified in a commercially available vehicle. The primary objective of using this mount

was to measure its dynamic stiffness and observe the trend of stiffness variation with frequency. This mount served as a baseline for predicting the dynamic stiffness behavior of an optimized mount in the X, Y, and Z directions. The behavior observed in the measured mount provides a reasonable foundation for this predictive analysis of the dynamic stiffness. The fixture used for the measurement is depicted in Figure 38.

Figure 38: Measured mount and the fixture of the bench test.
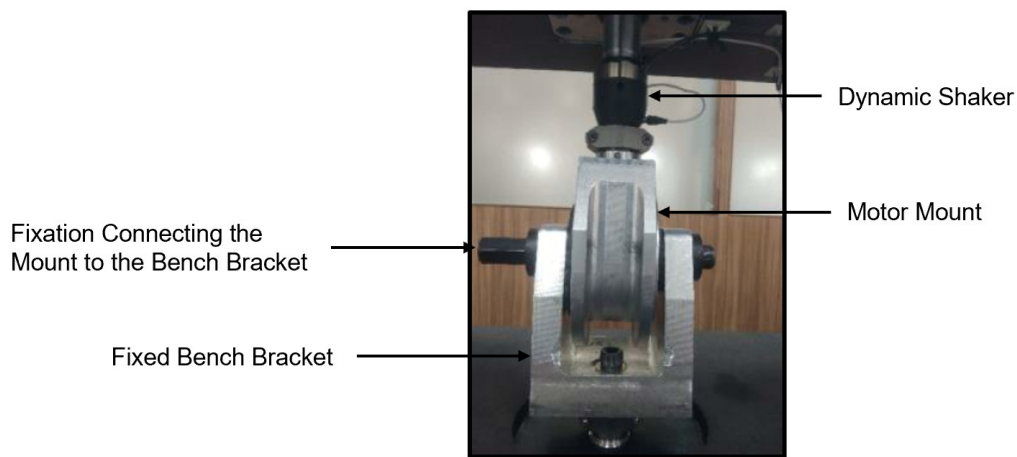
Source: the author.

Figure 39 shows the dynamic stiffness behavior of the measured mount until 600 Hz. The trend of the dynamic stiffness of the measured mount was used as a model to create the dynamic stiffness of the optimized mount.

Figure 39: Dynamic stiffness of the measured mount.
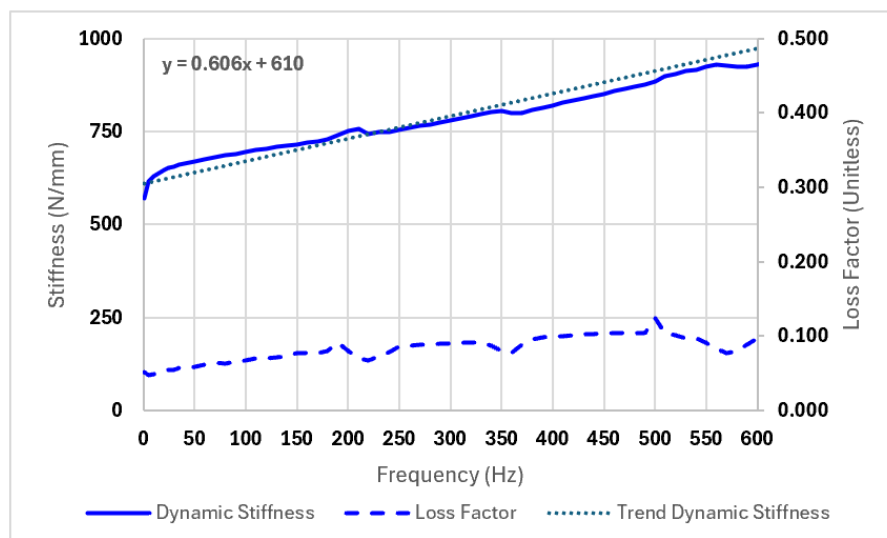
Table shows the dynamics stiffness on directions X, Y and Z of the optimized mount using the model identified by the measured mount. As the dynamic stiffness of the four optimized mounts are similar the static stiffness of mount 1 is selected to calculate the dynamic stiffness.

Table 24: Comparison of the magnitude of each positions of mounts 1 and 2 for Conditions 1, 2 and 3.

Frequency	Tan Delta	X Direction	Y Direction	Z Direction
		Kdyn	Kdyn	Kdyn
Hz	unitless	N/mm	N/mm	N/mm
1	0.051	400	186	486
5	0.048	403	188	488
10	0.049	406	191	491
15	0.051	409	194	494
20	0.053	412	197	497
25	0.054	415	200	500
30	0.054	418	203	503
35	0.057	421	206	506
40	0.058	424	209	509
45	0.057	427	212	512
50	0.058	430	215	515
60	0.061	436	221	521
70	0.064	442	227	527
80	0.063	449	234	534
90	0.066	455	240	540
100	0.068	461	246	546
110	0.069	467	252	552
120	0.070	473	258	558
130	0.071	479	264	564
140	0.073	485	270	570
150	0.076	491	276	576
160	0.077	497	282	582
170	0.077	503	288	588
180	0.080	509	294	594
190	0.091	515	300	600
200	0.080	521	306	606
210	0.069	527	312	612
220	0.067	533	318	618
230	0.073	540	325	625
240	0.078	546	331	631
250	0.085	552	337	637
260	0.087	558	343	643
270	0.088	564	349	649
280	0.089	570	355	655

290	0.089	576	361	661
300	0.090	582	367	667
310	0.091	588	373	673
320	0.091	594	379	679
330	0.091	600	385	685
340	0.087	606	391	691
350	0.080	612	397	697
360	0.076	618	403	703
370	0.089	624	409	709
380	0.095	631	416	716
390	0.098	637	422	722
400	0.099	643	428	728
410	0.100	649	434	734
420	0.101	655	440	740
430	0.103	661	446	746
440	0.103	667	452	752
450	0.103	673	458	758
460	0.104	679	464	764
470	0.104	685	470	770
480	0.104	691	476	776
490	0.104	697	482	782
500	0.123	703	488	788
510	0.104	709	494	794
520	0.101	715	500	800
530	0.096	721	506	806
540	0.097	728	513	813
550	0.092	734	519	819
560	0.083	740	525	825
570	0.077	746	531	831
580	0.080	752	537	837
590	0.088	758	543	843
600	0.096	764	549	849

Source: the author.

The dynamic stiffness derived from the measured model mount are shown in Figures 40, 41 and 42.

Figure 40: Calculated dynamic stiffness for the X direction of the mount 1.
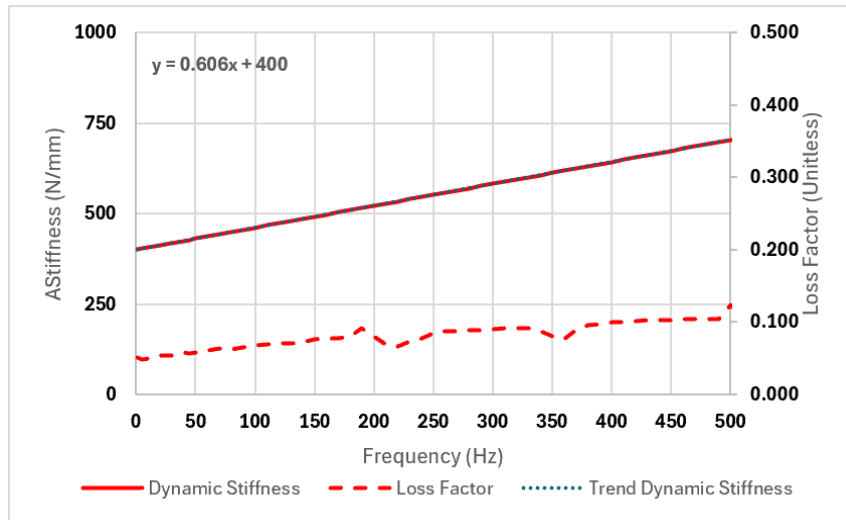
Source: the author.

Figure 41: Calculated dynamic stiffness for the Y direction of the mount 1.
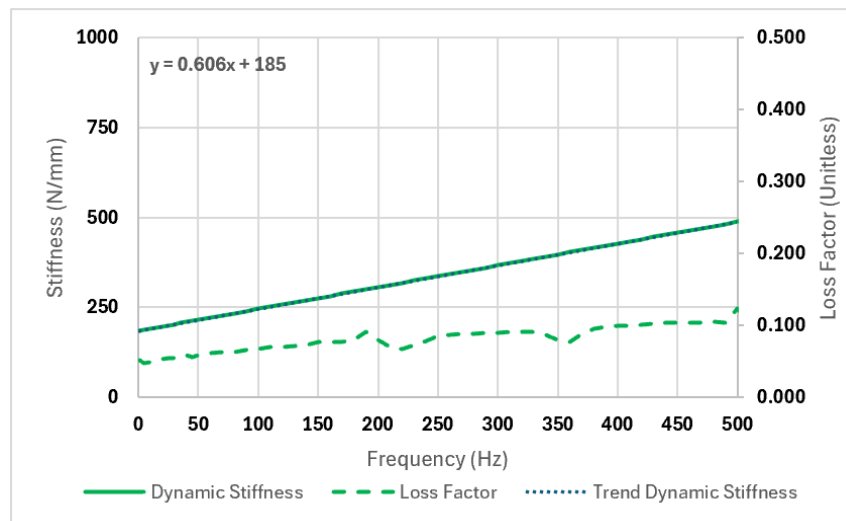
Source: the author.

Figure 42: Calculated dynamic stiffness for the Z direction of the mount 1.
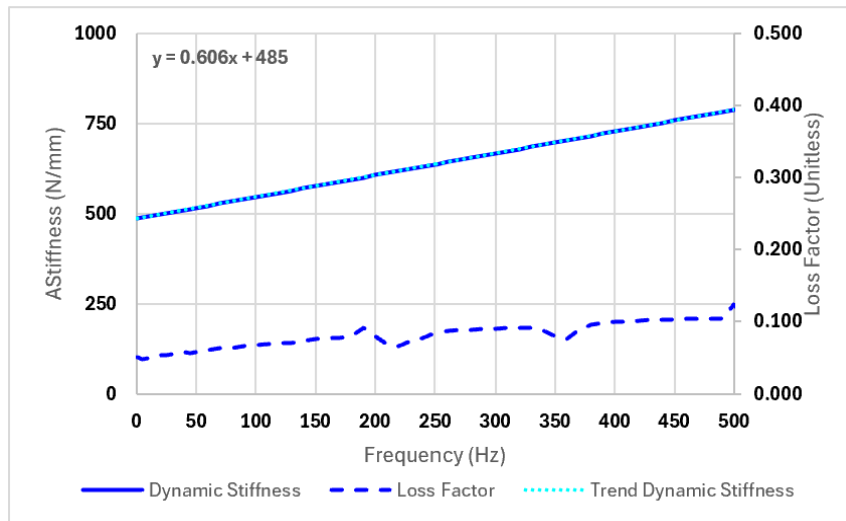
Source: the author.

The mount 1 transmissibility in X, Y and Z directions is shown in Table 25.

Table 25: Mount transmissibility of the X, Y and Z direction of the optimized mount 1.

Transmissibility Mount 1 (dB)			
Freq (Hz)	X	Y	Z
1	-28.3	-34.8	-26.7
5	-28.2	-34.7	-26.6
10	-28.2	-34.5	-26.6
15	-28.1	-34.4	-26.5
20	-28.0	-34.3	-26.5
25	-28.0	-34.1	-26.4
30	-27.9	-34.0	-26.4
35	-27.9	-33.9	-26.3
40	-27.8	-33.8	-26.3
45	-27.7	-33.6	-26.2
50	-27.7	-33.5	-26.2
60	-27.6	-33.3	-26.1
70	-27.4	-33.0	-26.0
80	-27.3	-32.8	-25.9
90	-27.2	-32.6	-25.8
100	-27.1	-32.4	-25.7
110	-27.0	-32.2	-25.6
120	-26.9	-32.0	-25.5
130	-26.8	-31.8	-25.4
140	-26.7	-31.6	-25.3
150	-26.6	-31.4	-25.3
160	-26.5	-31.2	-25.2
170	-26.4	-31.0	-25.1

180	-26.3	-30.9	-25.0
190	-26.2	-30.7	-24.9
200	-26.1	-30.5	-24.8
210	-26.0	-30.3	-24.8
220	-25.9	-30.2	-24.7
230	-25.8	-30.0	-24.6
240	-25.7	-29.9	-24.5
250	-25.6	-29.7	-24.4
260	-25.5	-29.6	-24.3
270	-25.4	-29.4	-24.3
280	-25.3	-29.3	-24.2
290	-25.2	-29.1	-24.1
300	-25.2	-29.0	-24.0
310	-25.1	-28.8	-24.0
320	-25.0	-28.7	-23.9
330	-24.9	-28.6	-23.8
340	-24.8	-28.5	-23.8
350	-24.7	-28.3	-23.7
360	-24.7	-28.2	-23.6
370	-24.6	-28.1	-23.5
380	-24.5	-27.9	-23.5
390	-24.4	-27.8	-23.4
400	-24.3	-27.7	-23.3
410	-24.3	-27.6	-23.3
420	-24.2	-27.5	-23.2
430	-24.1	-27.4	-23.1
440	-24.0	-27.2	-23.1
450	-24.0	-27.1	-23.0
460	-23.9	-27.0	-22.9
470	-23.8	-26.9	-22.9
480	-23.7	-26.8	-22.8
490	-23.7	-26.7	-22.7
500	-23.6	-26.6	-22.7
510	-23.5	-26.5	-22.6
520	-23.5	-26.4	-22.6
530	-23.4	-26.3	-22.5
540	-23.3	-26.2	-22.4
550	-23.3	-26.1	-22.4
560	-23.2	-26.0	-22.3
570	-23.1	-25.9	-22.3
580	-23.1	-25.8	-22.2
590	-23.0	-25.7	-22.2
600	-22.9	-25.6	-22.1

Source: the author.

The graph presented in Figure 43 shows the transmissibility of Table 25$_{2525}$ in X, Y and Z directions.

Figure 43: Mount 1 transmissibility in X, Y and Z directions.
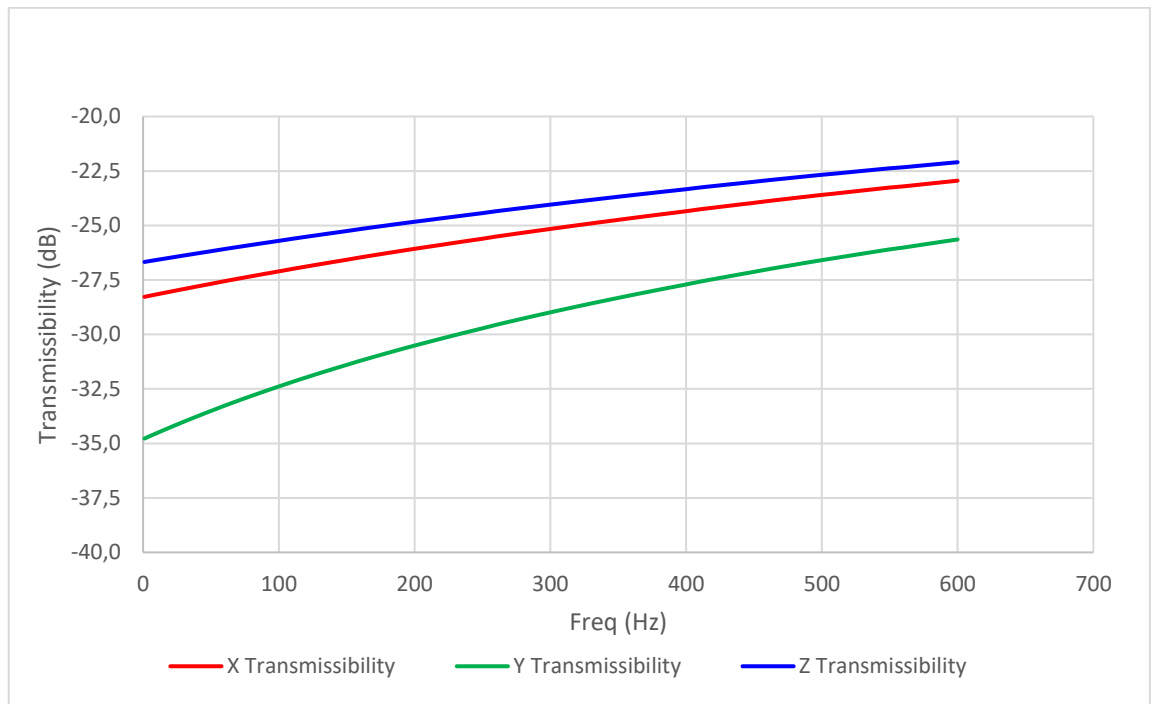
Source: the author.

It is clearly visible that the transmissibility decreases in absolute values as the frequency goes higher.

This behavior is associated by the increase of the dynamic stiffness along the frequency content.

5.5 MOTOR DISPLACEMENT IN FULL TORQUE LOAD

As a second step to evaluate the stiffness feasibility of the optimization process, the displacement in maximum torque of the motor is calculated as it can be used for package space protection.

For this calculation only the rotation coordinates is considered because the moment is generated in the interior of the motor.

The displacement is calculated using the Lagrange equations, which are expressed as follows:

$$\frac{d}{dt}\left(\frac{\partial L}{\partial \dot{q}_i}\right) - \frac{\partial L}{\partial q_i} + \left(\frac{\partial \Gamma}{\partial \dot{q}_i}\right) = f_i, \qquad i = 1, \dots, n, \tag{109}$$

L is defined as the Lagrangian which is $L = T_{total} - V_{total}$.

T_{total} is the total kinetic energy and V_{total} is the total potential energy.

$q_i, \dot{q}_i$ is the displacement and velocity of the i-generalized coordinate of the system.

Γ is the dissipative function due to the damping.

n is the number of degrees of freedom.

The matrix of inertia, damping and stiffness developed through Eq. (109) are given as follow.

$$m_{ij} = \frac{\partial^2 T_{total}}{\partial \dot{q}_i \partial \dot{q}_j}, \tag{110}$$

$$c_{ij} = \frac{\partial^2 \Gamma}{\partial \dot{q}_i \partial \dot{q}_j}, \tag{111}$$

$$k_{ij} = \frac{\partial^2 V}{\partial q_i \partial q_j}. \tag{112}$$

In the calculation of the displacement, only the rotation α, ψ and φ are used to calculate the displacement since the motor generates moment. These angle rotation α, ψ and φ are respectively in the axes X, Y and Z of the Figure (16).

For the motor analysed in this work, the torque is generated in the y direction, but the Torque Roll Axis (TRA) creates a decomposition in the three directions x, y and z. The motor considered in this work generates a torque of 10260 Nm about y. The torque roll axis angles are shown in Table 26.

Table 26: Torque roll axis angle of motor.

Torque Roll Axis		
θ_1 (°)	θ_2 (°)	θ_3 (°)
90.11	0.85	90.84

Source: the author.

After decomposing the torque, the final torque distribution is

$$\begin{Bmatrix} T_x \\ T_y \\ T_z \end{Bmatrix} = \begin{Bmatrix} -21 \\ 10259 \\ -151 \end{Bmatrix} Nm.$$

As it can be observed the main contribution of the torque remains about y, as the value about x is too small only the component of y and z will be considered in the displacement calculation. For this reason the Langrangian will be built taking into account only the ψ and φ coordinates.

$$L = V^\psi + V^\phi + T^\psi + T^\phi. \tag{113}$$

The V^ψ and the V^φ from the potential energy of each mount compression or extension due to the rotation of the coordinates ψ and φ, so the total potential energy will be given by $V_{total} = V^\psi + V^\varphi$. The expression of V^ψ and V^φ are

$$V^\psi = \frac{1}{2}\sum k_{i,z}\delta_{i,\psi}^2$$

$$\tag{114}$$

$$V^\varphi = \frac{1}{2}\sum k_{i,x}\delta_{i,\varphi}^2.$$

$\delta_{i,\psi}$ and $\delta_{i,\varphi}$ are the displacements on the mount i due to the rotation of coordinates ψ and φ.

The total kinetic energy is given by $T_{total} = T^\psi + T^\varphi$ due to the rotation of the motor about the CG. T^ψ and T^φ are given by

$$T^\psi = \frac{1}{2}\frac{\partial^2 T_{total}}{\partial\psi^2}\dot\psi^2$$

$$\tag{115}$$

$$T^\phi = \frac{1}{2}\frac{\partial^2 T_{total}}{\partial\varphi^2}\dot\varphi^2.$$

For the case where the maximum torque without variation has been considered, the total energy of the system is transformed only in potencial energy whereas the kinetic energy is zero. For this reason the motion equation of the system is given by

$$\begin{Bmatrix} T_x \\ T_y \\ T_z \end{Bmatrix} = \begin{bmatrix} 0 & 0 & 0 \\ 0 & \dfrac{\partial^2 V_{total}}{\partial\psi^2} & 0 \\ 0 & 0 & \dfrac{\partial^2 V_{total}}{\partial\varphi^2} \end{bmatrix} \begin{Bmatrix} 0 \\ \psi \\ \varphi \end{Bmatrix}. \tag{116}$$

To calculate the values of ψ and φ, the inverse of the matrix should be applied so the motion equation is given in Eq. (117).

$$\begin{Bmatrix} 0 \\ \psi \\ \phi \end{Bmatrix} = \begin{bmatrix} 0 & 0 & 0 \\ 0 & \dfrac{\partial^2 V_{total}}{\partial \psi^2} & 0 \\ 0 & 0 & \dfrac{\partial^2 V_{total}}{\partial \varphi^2} \end{bmatrix}^{-1} \begin{Bmatrix} T_x \\ T_y \\ T_z \end{Bmatrix}. \tag{117}$$

After replacing all variables in Eq. (117), the angular displacement are

$$\begin{Bmatrix} \alpha \\ \psi \\ \phi \end{Bmatrix} = \begin{Bmatrix} 0.000 \\ 0.080 \\ -0.022 \end{Bmatrix} \text{rad.}$$

With this result is now possible to figure out the displacement in Z due to the ψ coordinate and in X due to φ coordinate on each mount. The displacement results are shown in Table 27.

Table 27: Displacement on each mount caused by rotations of coordinates ψ and ϕ.

	Rotation in ψ		Rotation in φ
	Displacement in Z (mm)		Displacement in X (mm)
$\delta_{1,\psi}$	11.20	$\delta_{1,\varphi}$	-0.45
$\delta_{2,\psi}$	14.50	$\delta_{2,\varphi}$	0.41
$\delta_{3,\psi}$	-25.50	$\delta_{3,\varphi}$	-0.48
$\delta_{4,\psi}$	-25.50	$\delta_{4,\varphi}$	0.48

Source: the author.

As expected the biggest displacement contribution is in the Z direction where nearly the full torque is applied.

6 CONCLUSION AND FUTURE WORK

The objective of this study was to optimize the design of a vehicle motor mount by incorporating the rigid body mode and isolation performance as key technical criteria, aiming to develop a high-performance vibration isolation system.

For this purpose, an analytical rigid body mode model with generic inputs like the number of mounts, mount inclination, mount position, mount stiffness, and the loss factor of the mount was built. On top of that, the isolation model was created, and with this model was possible to evaluate the transmissibility function which describes the isolation performance.

The constraint functions were formulated based on the limits of mount position, stiffness, natural frequencies of the rigid body modes, modal purity, and transmissibility.

After setting all these constraints, the PDLB interior-point algorithm was applied for three different initial conditions of position keeping the same initial stiffness condition. For all three conditions of optimization, the objective functions were satisfied and high modal purity (higher than 85% for each DOF) and isolation performance were obtained, however for the Condition 2 the constraint of frequency separation of 2 Hz between the modes was not met. An interesting outcome observed from the optimization process was that the algorithm primarily focused on adjusting the mount position, with only minimal variations in the mount static stiffness. Nevertheless, an improvement of 7 dBs of the transmissibility performance of the static stiffness was achieved after the optimization.

The transmissibility performance of the dynamic stiffness was further analyzed. To achieve this, a commercially available mount with static stiffness comparable to that of the optimized mount was tested. The dynamic stiffness of the commercial mount was measured and it served as a reference to develop a model that accurately describes the dynamic stiffness. Utilizing this model, the dynamic stiffness of the optimized mount was created, and its transmissibility performance was assessed across a frequency range of 1 Hz to 600 Hz.

The evaluation of isolation performance based on the transmissibility function derived from the dynamic stiffness model showed promising results. The Y direction exhibited the highest isolation performance, followed by the X and Z directions.

Specifically, the transmissibility in the X direction ranged from -28.3 dB to -22.9 dB, in the Y direction from -34.8 dB to -25.6 dB, and in the Z direction from -26.7 dB to -22.1 dB.

To expand the analysis of the mount project in this work the package space considering the motor displacement was done. For this, the motor torque at full load in static load condition was applied and the load on each motor mount was calculated using the Lagrangian approach. Once the loads were calculated the displacements on each mount were calculated and the mount stiffness could also be evaluated in terms of package space. The greatest displacement was observed in the mounts 3 and 4, reaching -25.5 mm in the Z direction.

For future works, there are many things which can be explored like the formulation of the transmissibility function considering the crossing displacements due to different load directions. This kind of evaluation is important to understand how the interaction of the loads changes the mount isolation performance.

Another interesting work that can be done in the future is the study of the mount isolation performance in a high-frequency range. To expand the frequency range would be necessary to take into account the consideration of both the modes of the rubber isolation material and the bracket, because the resonance of each of these parts will affect the transmissibility performance of the mount. Additionally, another algorithms can be tested for optimization of this problem in order to meet the project requirements exploring more the stiffness variation.

Last but not least, the durability effects of the mount can also be explored to further enhance the validation of this study's findings. This would not only add robustness to the mount's lifespan assessment but also contribute to a more comprehensive understanding of the overall validation process.

REFERENCES

ADIGUNA, H. et al. Transient response of a hydraulic engine mount. **Journal of Sound and Vibration**, v. 268, n. 2, p. 217-248, 2003.

AHMADI, H. et al. **Development of smart engine mounts**. International Rubber Conference. Kuala Lampur: Malaysia. 2008.

ARORA, J. **Introduction to optimum design**. 2nd. ed. San Diego: Elsevier Academic Press, 2012.

BAILLIO, P. **True Sharp Edge Orifices**. Technical Report, Bird Precision Data Sheet. Waltham, p. 1-2. 2003.

BYRD, R. H. . G. J. C. . N. J. A Trust Region Method Based on Interior Point Techniques for Nonlinear Programming. **Mathematical Optimization Society**, v. 89, n. 4, p. 149-185, 2000.

BYRD, R. H. . H. M. E. . N. J. An Interior Point Algorithm for Large-Scale Nonlinear Programming. **SIAM Journal on Optimization**, v. 9, n. 4, p. 877-900, 1999.

CAO, L. J.; SADEGHI, F.; STACKE, L. E. An Explicit Finite-element Model to Investigate the Effects of Elastomeric Bushing on Bearing Dynamics. **Journal of Tribology-Transactions of the Asme**, v. 138, n. 3, p. 1-13, 2016.

CHEN, S. et al. **An Equivalent Model for Modal Analysis of Engine Mounting System**. 2nd International Conference on Electronic & Mechanical Engineering and Information Technology (EMEIT). Nanning: Atlantis Press. 2012. p. 1-5.

CHRISTOPHERSON, J.; MAHINFALAH, M.; JAZAR, R. N. Suspended Decoupler: A New Design of Hydraulic Engine Mount. **Advances in Acoustics and Vibration**, 2012, n. 5, 2012. p. 1-11.

CREDE, C. E. **Shock and Vibration Concepts in Engineering Design**. 1. ed. Nova York: Prentice Hall, 1965.

DAVALOS, O.; CALDINO-HERRERA, U.; CORNEJO-MONROY, D. Reduction of Stresses and Mass of an Engine Rubber Mount Subject to Mechanical Vibrations. **Strojniski Vestnik-Journal of Mechanical Engineering**, v. 67, n. 3, p. 101-113, 2021.

DELGADO, J. A. **A combinação dos métodos de barreira e de barreira modificada na resolução do Problema de Fluxo de Potência Ótimo Reativo**. Universidade Estadual Paulista Júlio de Mesquita. Bauru, p. 1 - 151. 2016.

EWINS, D. J. **Modal Testing:** Theory, Practice and Application. 2. ed. Taunton, Somerset, England: Research Studies Press LTD., 2000, ISBN 0-86380-218-4.

FLOWER, W. C. Understanding hydraulic mounts for improved vehicle noise, vibration and ride qualities. **SAE Technical Paper Series**, 1985. p. 832-841.

GADE, S.; HERLUFSEN, H. **Technical Review - Digital Filter Techniques vs. FFT Techniques for Damping Measurements**. 1. ed. Naerum: Brüel & Kjaer A/S, 1994.

GRAESSER, E. J.; WONG, C. R. **The Relationship of Traditional Damping Measures for Materials with High Damping Capacity**. David Taylor Research Center. Bethesda, MD, p. 1-46. 1991.

GRANVILLE, S. Optimal reactive dispatch through interior point methods. **IEEE Transactions on Communication**, v. 9, n. 1, p. 136-146, 1994.

GRIFFIN, M. J. **Handbook of Human Vibration**. 5. ed. Londres: Academic Press Limited, 1990.

HAFIDI, A. E. et al. Vibration reduction on city buses: Determination of optimal position of engine mounts. **Mechanical Systems and Signal Processing**, Paris, v. 24, n. 7, p. 2198-2209, 2010.

HARRIS, C. M.; PIERSOL, A. G. **Harris' Shock and Vibration Handbook**. 5th. ed. New York: McGraw-Hill, 2002.

HAUG, E. J. **COMPUTER-AIDED KINEMATICS AND DYNAMICS OF MECHANICAL SYSTEMS**. 2. ed. [S.l.]: Pearson College Div, v. 2, 2021.

HAZRA, S. . J. R. K. Study of Dynamics Stiffness and Shape Factor of Rubber Mounts to Address High-Frequency Resonance Issue in Electric Powertrain Mounting. **SAE Technical Paper Series**, 2020. p. 1-7.

HE, J.; FU, Z. **Modal Analysis**. 1. ed. Oxford: Butterworth-Heinemann, 2001.

HIXSON, E. L. **Mechanical Impedance and Mobility.** 3. ed. New York: McGraw Hill, 1997.

JAGASICS, S.; VAJDA, I. Cogging torque reduction by magnet pole pairing technique. **Acta Polytech. Hungaria 13**, Budapest, v. 13, n. 4, p. 107–120, 2016.

KRUSE, E.; CARRE, B. Modeling and analysis of high-frequency dynamic characteristics of double isolation rubber mounts. **Journal of Automobile Engineering** , v. 238, n. 4, p. 620-632, 2024.

LEE, H. S.; SHIN, J. K.; MSOLLI, S. Prediction of the Dynamic Equivalent Stiffness for a Rubber Bushing Using the Finitie Element Method and Empirical Modeling. **International Journal of Mechanics and Materials in Design**, v. 15, p. 77-91, 2017.

LEE, K. H..; CHOI, Y. T.; HONG, S. P. Performance Design of Hydraulic Mount for Low Frequency Engine Vibration and Noise Control. **SAE Technical Paper Series**, 1994. p. 1-14.

LIN, H.; TSAY, T. Modeling Identification and Simulation of Bank to Turn Unmanned Aerial Vehicle. **WSEAS Transactions on Systems**, Taiwan, v. 10, n. 4, p. 91-103, April 2011.

LIN, R. C.; SCHOMBURG, U. A Finite Elastic-Viscoelastic-Elastoplastic Material Law with Damage: Theoretical and Numerical Aspects. **Computer Methods in Applied Mechanics and Engineering**, v. 192, p. 1591-1627, 2003.

LION, A.; JOHILITZ, M. A mechanical model to describe the vibroacoustic behaviour of elastomeric engine mounts for electric vehicles. **Mechanical System and Digital Processing** , Neubiberg, v. 144, p. 2-14, 2020.

LI-RONG, W.; ZHEN-HUA, L.; ICHIRO, H. An elementary simulation of vibration isolation characteristics of hydraulically damped rubber mount of car engine. **SAE Technical Paper Series**, 2001. p. 1-9.

MASSEY, B.; WARD-SMITH, J. **Mechanics of Fluids**. 8th. ed. Abingdon: Taylor & Francis, 2006.

NASHIF, A. D.; JONES, D. I.; HENDERSON, J. P. **Vibration Damping**. New York: John Wiley & Sons, Inc., 1985.

OHADI, A.; MAGHSOODI, G. Simulation of engine vibration on non-hydraulic engine mounts. **Journal of Vibration and Acoustics - Transactions of the ASME**, v. 129, n. 4, p. 417-424, 2007.

OOI, L. E.; RIPIN, Z. M. **Dynamic stiffness and loss factor measurement of engine rubber mount by impact tests**. Sains Malaysia Univertisty. Nibong Tebal. 2010.

PARK, J.; SINGH, R. Role of spectrally varying mount properties in influencing coupling between powertrain motions under torque excitation. **Journal of Sound and Vibration**, Columbus, v. 329, n. 14, p. 2895-2914, 2010.

PENG, J.; WANG, M.; JIANG, Y. Simulation and Optimization Method of High Frequency Dynamic Characteristics of Rubber Mount. **SAE Technical Paper Series**, 2021. p. 1-10.

PETRONE, D. F. &. R. Damping evaluation on eco-friendly sandwich panels through reverberation time (RT 60) measurements. **Jornal of Vibration and Control**, v. 21, n. 16, p. 3329-3338, 2015.

QUINTANA, V. H. . T. G. L. . M. J. Interior-point methods and their applications to power system: a classication of publications and software codes. **IEEE Transactions on Communication**, v. 15, n. 1, p. 170-176, 2000.

RIVIN, E. I. Passive engine Mounts - Some Directions for Further Development. **SAE Technical Paper Series**, 1985. p. 582-591.

SHI, H.; WU, P. A Nonlinear Rubber Spring Model Containing Fractional Derivatives for Use in Railroad Vehicle Dynamic Analysis. **Journal of Rail and Rapid Transit**, v. 230, n. 7, p. 1745-1759, 2016.

SINGH, R.; KIM, G.; RAVINDRA, P. Linear analysis of automotive hydro-mechanical mount with emphasis on decoupler characteristics. **Journal of Sound and Vibration**, v. 158, n. 2, p. 219-243, 1992.

SOOVERE, J.; DRAKE, M. L. **Aerospace Structure Technology Damping Design Guide Volume 1 - Technology Review**. Air Force Wright Aeronautical Laboratories. Burbank, p. 1-41. 1985. (AFWAL).

SWANSON, D. A. Active engine mounts for Vehicles. **SAE Technical Paper Series**, 1993. p. 1-11.

TAHIR, M. F. **Multidisciplinary optimization of an elastomeric mount system**. Tsinghua University. Beijing. 2018.

USHIJIMA, T.; TAKANO, K.; KOJIMA, H. High performance hydraulic mount for improving vehicle noise and. **SAE Technical Paper Series**, 1989. p. 1-12.

WALTZ, R. A. . M. J. L. . N. J. . O. D. An interior algorithm for nonlinear optimization that combines line search and trust region steps. **Mathematical Programming**, v. 107, n. 3, p. 391-408, 2006.

XU, C. et al. Identification of Engine Inertia Parameters and System Dynamic Stiffness via In Situ Method. **Hindawi Mathematical Problems in Engineering** , v. 2021, p. 1-16, 2021.

YU, Y.; NAGANATHAN, N. G.; DUKKIPATI, R. V. A literature review of automotive vehicle engine mounting systems. **Mechanism and Machine Theory**, v. 36, n. 1, p. 123-142, 2001.

ZHANG, J.; LIU, X. Research on High-Frequency Dynamic Models of Rubber Mounts with Second-Stage Isolation. **SAE Technical Paper Series**, 2022. p. 1-8.

APPENDIX A – KKT CRITERIA

To find a minimum point $\{X^*\}$ such that f is constrained in the equality equation h_j the Lagrange multiplier is used. Suppose that $\{X^*\}$ is a regular point and a local minimum for the problem. Then there exist unique Lagrange multipliers v_j^*, j = 1 to p such that:

$$\frac{\partial f(\{X^*\})}{\partial X_q} + \sum_{j=1}^{p} v_j^* \frac{\partial h_j(\{X^*\})}{\partial X_q} = 0;\ q = 1\ to\ \beta \qquad (A.1)$$

For convenience the equation above can be arranged using a Lagrange function, where the Lagrange function is described as below:

$$L(\{X\}, \{v\}) = f(\{X\}) + \sum_{j=1}^{p} v_j h_j(\{X\}) \qquad (A.2)$$

Through Eq. (A.2) the Eq. (A.1) can be rewritten according to Eq. (A.3):

$$\nabla L(\{X^*\}, \{v^*\}) = \mathbf{0} \ \ or \ \ \frac{\partial L(\{X^*\}, \{v^*\})}{\partial X_q} = 0;\ q = 1\ to\ \beta$$

$$\frac{\partial L(X^*, v^*)}{\partial v_j} = 0\ and\ h_j(X^*) = 0;\ j\ =\ 1\ to\ p$$

$$(A.3)$$

The gradient conditions of Eq. (A.3) shows that the Lagrange function is stationary with respect to both $\{X\}$ and $\{v\}$. Therefore, it may be treated as an unconstrained function in the variables $\{X\}$ and $\{v\}$ to determine the stationary points. Note that any point that does not satisfy these conditions cannot be a local minimum point. However, a point satisfying the conditions need not be a minimum point either. It is simply a candidate minimum point which can actually be an inflection or maximum point. The second-order necessary and sufficient conditions explained later in this chapter can distinguish between the minimum, maximum, and inflection points.

With Eq. (A.3) is possible to get the β equations associated to $\{X\}$ and p equations associated to $\{v\}$ to find the unknown variables.

Regarding the inequality constraint we have the option to convert it into an equality constraint by introducing a new variable known as the slack variable. Given

that the constraint takes the form "$\leq$" its value is either negative or zero. Consequently, the slack variable must consistently remain nonnegative or zero to equalize the inequality. An inequality constraint of the form $g_i(X) \leq 0$ is essentially equivalent to the equality constraint $g_i(X) + s_i = 0$,

Where $s_i \geq 0$ serves as the slack variable. These variables s_i are treated as unknowns in the design problem, alongside the original variables, and their values are determined as part of the solution process. An inequality constraint is considered active (tight) when the corresponding slack variable s_i has a zero value, indicating no "slack" in the constraint. Conversely, for any $s_i > 0$, the corresponding constraint is considered inactive, and the slack is given by s_i.

It's important to note that this procedure necessitates the introduction of an additional variable s_i and an additional constraint $s_i \geq 0$ for each inequality constraint. This results in an increase in the dimension of the design problem. To guarantee the constraint $s_i \geq 0$, an alternative approach is to use s_i^2 as the slack variable instead of s_i. Consequently, the inequality $g_i(X) \leq 0$ is transformed into an equality as given by Eq. (A.4).

$$g_i(\{X\}) + s_i^2 = 0 \qquad (A.4)$$

Where s_i can assume any real value. This form is applicable in the Lagrange Multiplier Theorem for handling inequality constraints and deriving the associated necessary conditions. The m new equations required to determine the slack variables are obtained by ensuring that the Lagrangian L is stationary with respect to the slack variables as well ($\frac{\partial L}{\partial s} = \mathbf{0}$).

It's worth mentioning that once a design point is specified, Eq. (A.3) allows for the calculation of the slack variable s_i^2. If the constraint is satisfied at the point ($g_i \leq 0$), then $s_i^2 \geq 0$. In the case of violation, s_i^2 is negative, which is unacceptable, indicating that the point is not a viable candidate for a minimum point. Additionally, there exists an additional necessary condition for the Lagrange multipliers of "$\leq$ type" constraints given as

$$u_i^* \geq 0; \; i = 1 \; to \; m \qquad (A.5)$$

where u_i^* is the Lagrange multiplier for the ith inequality constraint. Thus, the Lagrange multiplier for each "$\leq$" inequality constraint must be nonnegative. If the constraint is inactive at the optimum, its associated Lagrange multiplier is zero. If it is active ($g_i(\{X\})$ = 0), then the associated multiplier must be nonnegative.

The necessary conditions for the equality and inequality constraints can be summed up in what are commonly known as the Karush-Kuhn-Tucker (KKT) first-order necessary conditions.

Let $\{X^*\}$ be a regular point of the feasible set that is a local minimum for $f(\{X\})$ subject to $h_j(\{X\}) = 0$; i = 1 to p; $g_i(\{X\}) \leq 0$; j = 1 to m. Then there exist Lagrange multipliers v_j^* (a p-vector) and u_i^* (an m-vector) such that the Lagrangian function is stationary with respect to X_q, v_j^*, u_i^*, and s_i at the point $\{X^*\}$.

$$L(\{X\}, \{v\}, \{u\}, \{s\}) = f(\{X\}) + \sum_{j=1}^{p} v_j h_j(\{X\}) + \sum_{i=1}^{m} u_j(g_i(\{X\}) + s_i^2) \qquad (A.6)$$

Once the Lagrangian is built the gradient conditions are described.

$$\frac{\partial L}{\partial X_q} = \frac{\partial L}{\partial X_q} + \sum_{j=1}^{p} v_j^* \frac{\partial h_j}{\partial X_q} + \sum_{j=1}^{p} u_i^* \frac{\partial g_i}{\partial X_q} = 0; \quad q = 1 \text{ to } \beta \qquad (A.7)$$

$$\frac{\partial L}{\partial v_j} = 0; \; h_j(\{X^*\}) = 0; \; j = 1 \text{ to } p \qquad (A.8)$$

$$\frac{\partial L}{\partial u_i} = 0; \; (g_i(\{X^*\}) + s_i^2) = 0; \; i = 1 \text{ to } m \qquad (A.9)$$

$$s_i^2 \geq 0; \; or \; equivalent \; g_i \leq 0; \; i = 1 \text{ to } m \qquad (A.10)$$

$$\frac{\partial L}{\partial s_i} = 0; \; 2u_i^* s_i = 0; \; i = 1 \text{ to } m \qquad (A.11)$$

$$u_i^* \geq 0; \; i = 1 \text{ to } m \qquad (A.12)$$

Finally the concept of Lagrange multiplier can be applied in its known form in Eq. (A.13).

$$-\frac{\partial f}{\partial X_q} = \sum_{j=1}^{p} v_j^* \frac{\partial h_j}{\partial X_q} + \sum_{j=1}^{p} u_i^* \frac{\partial g_i}{\partial X_q} = 0; \quad q = 1\ to\ \beta \qquad (A.13)$$

KKT conditions are not applicable at the points that are not regular. In those cases their use may yield candidate minimum points; however, the Lagrange multipliers are not unique.

Any point that does not satisfy KKT conditions cannot be a local minimum unless it is an irregular point (in that case KKT conditions are not applicable). Points satisfying the conditions are called KKT points.

The points satisfying KKT conditions can be constrained or unconstrained. They are unconstrained when there are no equalities and all inequalities are inactive.

If the candidate point is unconstrained, it can be a local minimum, maximum, or inflection point depending on the form of the Hessian matrix of the cost function.

If there are equality constraints and no inequalities are active (i.e., $\{u\} = 0$), then the points satisfying KKT conditions are only stationary. They can be minimum, maximum, or inflection points.

If some inequality constraints are active and their multipliers are positive, then the points satisfying KKT conditions cannot be local maxima for the cost function (they may be local maximum points if active inequalities have zero multipliers). They may not be local minima either, this will depend on the second-order necessary and sufficient conditions.

Solutions of the first-order necessary conditions are candidate local minimum, but the second-order necessary and sufficient conditions must be applied at $\{X^*\}$ to verify if it is indeed a local minimum. In this section, we shall discuss second-order necessary and sufficiency conditions for constrained optimization problems. The second-order necessary and sufficiency condition are evaluated considering active constraint at $\{X^*\}$ to determine the feasible changes of the vector $\{d\}$, where $\{d\}$ is the vector giving the direction of the local minimum point. So, in each iteration to find the local minimum the new candidate point is updated by $\{X\} = \{X^*\} + \{d\}$. Only the points $\{X\} = \{X^*\} + \{d\}$ in the neighborhood of $\{X^*\}$ that satisfy the active constraint equations will be considered. Any $\{d\} \neq \{0\}$ satisfying active constraints to the first order must be in the constraint tangent hyperplane (Figure 3.3-1). Such $\{d\}$'s are then orthogonal to the gradients of the active constraints since constraint gradients are normal to the constraint tangent hyperplane. Therefore, the dot product of $\{d\}$ with each of the

constraint gradients ∇h_j and ∇g_i must be zero, i.e., $\nabla h_j^T \{d\} = 0$ and $\nabla g_i^T \{d\} = 0$. These equations are used to determine directions $\{d\}$ that define a feasible region around the point $\{X^*\}$. Note that only active inequalities constraints ($g_i = 0$) are used in determining $\{d\}$. The situation is depicted in (Figure 3.3-1) for one inequality constraint.

Figure 44: Directions $\{d\}$ used in constrained sufficiency conditions.
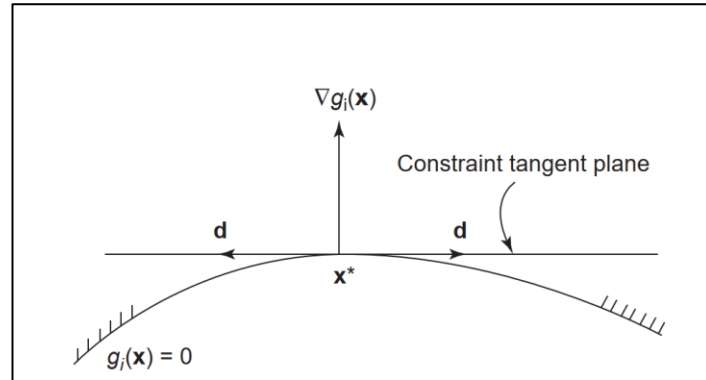
Source: adapted from Arora (2012).

To derive the second-order conditions, the Taylor's expansion of the Lagrange function is written and only $\{d\}$'s satisfying the preceding conditions are considered. $\{X^*\}$ is then a local minimum point if the second-order term of Taylor's expansion is positive for all $\{d\}$ in the constraint tangent hyperplane. This is then the sufficient condition for an isolated local minimum point. As a necessary condition the second-order term must be nonnegative.

In short, these necessary and sufficient conditions can be written by the following equations.

For second-order necessary condition for general constrained problems considering that $\{X^*\}$ satisfy the first-order KKT necessary conditions for the general optimum design problem. The Hessian of the Lagrange function L at $\{X^*\}$ is described in Eq. (A.14).

$$\nabla^2 L = \nabla^2 f + \sum_{j=1}^{p} v_j^* \nabla^2 h_j + \sum_{i=1}^{m} u_i^* \nabla^2 g_i = 0 \qquad (A.14)$$

Now with $\{d\} \neq \{0\}$ the linear system must satisfy the conditions below.

$$\nabla h_j^T \{d\} = 0; j = 1 \text{ to } p \qquad (A.15)$$

$$\nabla g_i^T \{d\} = 0; \text{ for all active inequalities} \qquad (A.16)$$

Then if $\{X^*\}$ is a local minimum point for the optimum design problem, it must be true that:

$$Q \geq 0 \; where \; Q = \{d\}^T \nabla^2 L(\{X^*\})\{d\} \qquad (A.17)$$

These are the necessary conditions of second-order general constrained problem, now there are some slightly differences for the second-order sufficient condition of the constrained problem that are presented on the upcoming Eqs. (A.18), (A.19) and (A.20).

Considering again that at $\{X^*\}$ the first-order KKT necessary conditions for the general optimum design problem is satisfied, the nonzero field directions ($\{d\} \neq \{0\}$ and Eqs. (A.18), (A.19), (A.20) and (A.21) are satisfied, then $\{X^*\}$ is an isolated local minimum point (isolated means that there are no other local minimum points in the neighborhood of $\{X^*\}$.

$$\nabla h_j^T \{d\} = 0; j = 1 \text{ to } p \qquad (A.18)$$

$$\nabla g_i^T \{d\} = 0; \text{ for all active inequalities with } u_i^* > 0 \qquad (A.19)$$

$$\nabla g_i^T \{d\} \leq 0; \text{ for those active inequalities with } u_i^* = 0 \qquad (A.20)$$

$$Q \geq 0 \; where \; Q = \{d\}^T \nabla^2 L(\{X^*\})\{d\} \qquad (A.21)$$

The last but not least is the strong sufficient condition, which says that if $\{X^*\}$ satisfy the first-order KKT necessary conditions for the general optimum design problem and the Hessian $\nabla^2 L(X^*)$ for the Lagrange function at $\{X^*\}$ is positive definite then $\{X^*\}$ is an isolated minimum point.